Test of the Equivalence Principle in an Einstein Elevator

Annual Report #2

NASA Grant NAG3-2881

For the period 1 March 2004 through 28 February 2005

Principal Investigator

Irwin I. Shapiro

March 2005

Prepared for
National Aeronautics and Space Administration
Office of Biological and Physical Research
Washington, DC

Smithsonian Institution
Astrophysical Observatory
Cambridge, Massachusetts 02138

Test of the Equivalence Principle in an Einstein Elevator

Annual Report #2

NASA Grant NAG3-2881

For the period 1 March 2004 through 28 February 2005

Principal Investigator
Irwin I. Shapiro

Co-Investigators
S. Glashow
E.C. Lorenzini
M.L. Cosmo
P.N. Cheimets
N. Finkelstein (E/PO)
M. Schneps (E/PO)

Non-US partners (IFSI)
V. Iafolla (non-US PI)
D. Lucchesi
S. Nozzoli
F. Santoli

Collaborators
J. Ashenberg

Ph.D. Students
C. Bombardelli

SAO Engineering
M. Freeman
T. Gauron
R. Ingram

March 2005

Prepared for
National Aeronautics and Space Administration
Office of Biological and Physical Research
Washington, DC

Smithsonian Institution
Astrophysical Observatory
Cambridge, Massachusetts 02138

The Smithsonian Astrophysical Observatory
is a member of the
Harvard-Smithsonian Center for Astrophysics

Table of Contents

Summary

This Annual Report illustrates the work carried out during the last grant-year activity on the Test of the Equivalence Principle in an Einstein Elevator. The activity focused on the following main topics: (1) analysis and conceptual design of a detector configuration suitable for the flight tests; (2) development of techniques for extracting a small signal from data strings with colored and white noise; (3) design of the mechanism that spins and releases the instrument package inside the cryostat; and (4) experimental activity carried out by our non-US partners (a summary is shown in this report).

The analysis and conceptual design of the flight-detector (point 1) was focused on studying the response of the differential accelerometer during free fall, in the presence of errors and precession dynamics, for various detector's configurations. The goal was to devise a detector configuration in which an Equivalence Principle violation (EPV) signal at the sensitivity threshold level can be successfully measured and resolved out of a much stronger dynamics-related noise and gravity gradients. A detailed analysis and comprehensive simulation effort led us to a detector's design that can accomplish that goal successfully.

The techniques developed for signal extraction (point 2) was focused on extracting an EPV signal at the threshold level from the noise affecting the detector's output data. Techniques were developed for signal extraction from colored and white noises. Moreover, algorithms were developed/utilized for evaluating the confidence level in detecting the signal and the statistical error in estimating its amplitude.

The engineers in our team worked on the design (point 3) of the mechanism that spins and releases the instrument package inside the cryostat during the fall of the capsule. Engineering drawings of the mechanism are presented with a list of key components of the mechanism and a description of its functions.

Finally, a brief summary of the experimental activity (point 4) carried out during the last year by our non-US partners at the IFSI laboratory (Rome, Italy) is presented. The experimental work focused on the construction of a second differential accelerometer prototype that improves upon the performance of the previous prototype and its initial calibration tests in the laboratory.

List of Figures

List of Tables

Brief Description of Experiment

The scientific goal of the experiment is to test the equality of gravitational and inertial mass (i.e., to test the Principle of Equivalence) by measuring the independence of the rate of fall of bodies from their compositions. The measurement is accomplished by measuring the relative displacement (proportional to the acceleration) of falling bodies of different materials which are the proof masses of a differential accelerometer[i].

A differential displacement at the expected frequency between the two proof masses different from zero will indicate a violation of the Equivalence Principle. The goal is to measure the Eötvös ratio $\delta g/g$ (differential acceleration/common acceleration) with a targeted accuracy of a few parts in 10^{-15}, which is about two orders of magnitude better than the state of the art[ii] [iii]. Thanks to the improved accuracy the test will probe the territory where possible violations of the Equivalence Principle have been postulated[iv] [v].

The experiment is carried out in vertical free fall with the experimental capsule released from a stratospheric balloon at an altitude of 40 km[vi]. The capsule, that is evacuated and at cryogenic temperature, is released from balloon and immediately afterward the detector is released inside the falling capsule from its top. Depending on the ballistic coefficient of the capsule, the detector takes between 25 s and 30 s to span the 2-m length of the capsule while the capsule falls between 3.1 km and 4.4 km. This technique provides an environment that is almost free of perturbations external to the detector.

Flight Detector Analysis and Conceptual Design

Introduction

A successful design of the differential acceleration detector for the balloon flights involves a careful analysis of the motion of the instrument package (that houses the detector) in free fall. This issue is also present in space-based detectors operating in a spacecraft that is not perfectly fixed in inertial space. Since rotation of the spacecraft with respect to inertial space is a highly desirable feature for helping in separating the violation signal from noise sources, addressing the issue of measuring differential accelerations in a moving detector is of general importance for tests of the Equivalence Principle both in free fall from balloons and in space.

The dynamics analyses that we have conducted on various detector configurations have shown that the details of relative motion of the proof masses with respect to the instrument package (or spacecraft for a space-based test) are important for enabling the extraction of a violation signal from the much greater dynamics-related noise[vii].

Let us first consider a configuration in which the proof masses can only translate (i.e., they are constrained to move along a line) with respect to the instrument package. It is obvious that if the centers of mass (CMs) of the proof masses were both perfectly coincident with the CM of the instrument package then the dynamical coupling between the rotation of the instrument package and the motion of the proof masses would be null. However, this is not a realistic case because construction imperfections and material inhomogeneities give rise to CMs that are not coincident. Even if the proof masses were controlled in order to reduce the error between the two CMs locations, the error with respect to the CM of the instrument package or spacecraft would be present if the spacecraft were to have fluids on board because the spacecraft CM would not be perfectly stable. In other words, we must always assume that those errors are present and, consequently, we need to quantify their impact on our ability to extract a differential acceleration signal at the desired threshold level from the prevailing dynamics noise.

In a rotational detector configuration, in which the two proof masses are constrained to rotate with respect to the instrument package (or spacecraft) the importance of coincidence among the CMs of the proof masses and the CM of the instrument package is diminished with respect to the importance of the equality between the moments of inertia between the two proof masses (see later on).

In yet another detector configuration (that we call roto-translational), the proof masses are hinged off their CMs (e.g., at their edges). In this case, the motion of the proof masses with respect to their housing (instrument package or spacecraft) is a combination of a rotation and a translation and, consequently, both sets of issues pointed out previously apply to this case.

In Annual Report #1 (Ref. [viii]) for this grant we have already analyzed the dynamics of the translational configuration for the flight detector. The conclusion of that analysis is that the precession frequency of the instrument package in free fall should be in a particular frequency

window in order for the dynamics-related noise to be separated from the frequency (equal to the rotation of the package) of the violation signal and not to saturate the differential accelerometer response. One problem with the translational configuration for our detector, which has mechanically constrained proof masses, is the difficulty in manufacturing mechanical flexural constraints that provide low frequency for the translational motion along the sensitive axis. Low-frequency flexural constraints need to be long (leading to a bulky detector) and thin (leading to a weak detector). We need to utilize the rotational degree of freedom for the sensing motion of the proof masses in order to solve this issue. Moreover, gravity gradients play a major role in translational configurations while their role can be strongly diminished (see later on) in rotational configurations of appropriate design.

We will analyze both the roto-translational configuration and a purely rotational configuration of the detector in the following sections.

Detector dynamics analysis

Roto-translational configuration

Motion of proof masses with respect to detector's housing

Let us consider a set of three rigid bodies A, B, C constrained to each other in such a way that the relative motion of A with respect to C is a rotation around a pivot axis $<d_A>$ and the relative motion of B with respect to C is a rotation around a pivot axis $<d_B>$ with $<d_A>$ and $<d_B>$ parallel but not necessarily coincident. The pivot axes are not located at the centers of mass (CMs) of the proof masses but rather at distances b_A and b_B from the CMs of A and B. Let A and B be linked with C through a torsional spring dashpot system around the axes $<d_A>$ and $<d_B>$ characterized by elastic and damping coefficients (k_A, ξ_A) and (k_B, ξ_B) respectively. An example of relationship between spin and pivot axis for one proof mass is shown in Figure 1.

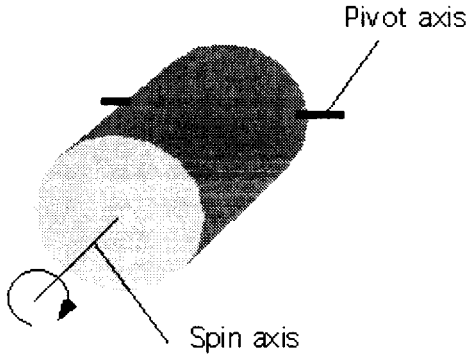

Figure 1 Schematic of one proof mass in a roto-translational configuration.

Let <x,y,z> be a reference system centered at the global center of mass CM of the system composed by the three rigid bodies. Let y be parallel to <d_A> and <d_B> (such axis is exiting the page in Figure 2), z parallel to the central symmetry axis of body C ,and x right-handed with y and z.

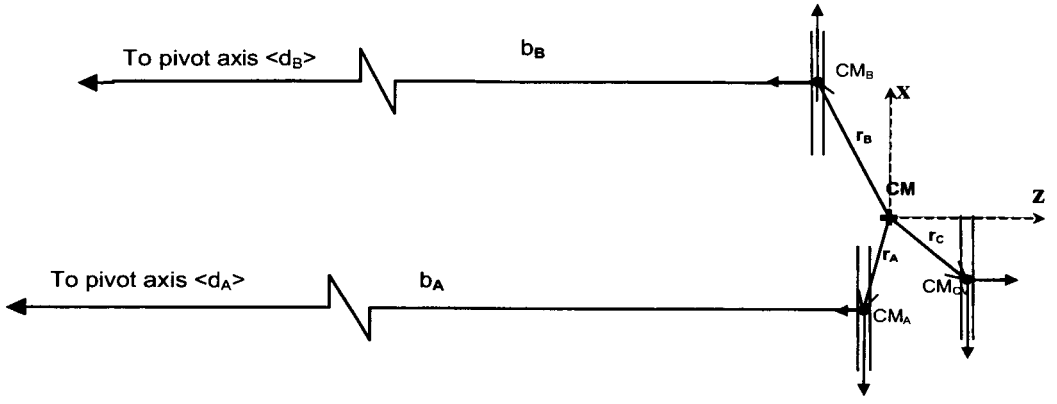

Figure 2 Geometry of individual centers of mass position with respect to pivot axis.

Since the mutual rotations between the three bodies will be of the order of a few arc seconds, we will assume that the components of vectors and inertia matrices with respect to the body axes of A and B are equal to the same components with respect to <x,y,z> (i.e., the body axes of C).

Let $\boldsymbol{\omega}_C = (\omega_x,\omega_y,\omega_z)^T$ be the angular velocity vector of body C and consequently of the reference frame <x,y,z> . The angular velocity of body A and B, projected on <x,y,z> are then:

$$\boldsymbol{\omega}_A = \left(\omega_x,\omega_y + \frac{\dot{x}_A}{b_A},\omega_z\right)^T \tag{1.1}$$

$$\boldsymbol{\omega}_B = \left(\omega_x,\omega_y + \frac{\dot{x}_B}{b_B},\omega_z\right)^T \tag{1.2}$$

The equations of motion of the system written with respect to an inertial system centered at the Earth are:

$$m_A(\ddot{\mathbf{R}}_{CM} + \ddot{\boldsymbol{\rho}}_A) = \mathbf{F}_A^g + \mathbf{F}_A^k + \mathbf{F}_A^{\xi} + \mathbf{F}_A^b + m_A \cdot \mathbf{a}_A^{EPV} \tag{2.1}$$

$$m_B(\ddot{\mathbf{R}}_{CM} + \ddot{\boldsymbol{\rho}}_B) = \mathbf{F}_B^g + \mathbf{F}_B^k + \mathbf{F}_B^{\xi} + \mathbf{F}_B^b \tag{2.2}$$

$$m_C\boldsymbol{\rho}_C = -m_A\boldsymbol{\rho}_A - m_B\boldsymbol{\rho}_B \tag{2.3}$$

where $\boldsymbol{\rho}$ is the radius vector of each individual center of mass relative to the overall CM and projected on the inertial system, $\mathbf{R}_{CM}$ is the radius vector of CM from the earth center projected

on the inertial system, $\mathbf{F}^g$ is the earth gravity field force, $\mathbf{F}^k$ the equivalent force of the internal spring and $\mathbf{F}^\xi$ the equivalent force of the internal damper acting on each mass. $\mathbf{F}^b$ is the force transmitted to each mass from the pivotal constraint as a consequence of the rigid body attitude motion of A and B. We also added the acceleration $\mathbf{a}^{EPV}$ acting on the mass A to simulate a violation of the equivalent principle. The equations of motion of the system center of mass are:

$$\ddot{\mathbf{R}}_{CM} = -\frac{\mu_E \mathbf{R}_{CM}}{\mathbf{R}_{CM}^3} + \frac{\mathbf{F}_C^p}{m_T} \tag{3}$$

where $\mathbf{F}_C^p$ is a perturbing force acting on the external case during free fall and m_T the total mass of the system.

The gravitational forces appearing in Eqs. (2.1) and (2.2) can be written in terms of a gravity gradient matrix $[\Gamma^E]$ with respect to CM as follows:

$$\mathbf{F}_A^g = m_A\left(-\frac{\mu_E \mathbf{R}_{CM}}{\mathbf{R}_{CM}^3} + \left[\Gamma^E\right]\boldsymbol{\rho}_A\right) \tag{4.1}$$

$$\mathbf{F}_B^g = m_B\left(-\frac{\mu_E \mathbf{R}_{CM}}{\mathbf{R}_{CM}^3} + \left[\Gamma^E\right]\boldsymbol{\rho}_B\right) \tag{4.2}$$

The earth gravity gradient matrix, in inertial coordinates, has the diagonal form:

$$\left[\Gamma^E\right] = \begin{bmatrix} g_{11} & 0 & 0 \\ 0 & g_{22} & 0 \\ 0 & 0 & g_{33} \end{bmatrix} \tag{5}$$

After plugging Eqs. (3) into Eqs. (2) we obtain:

$$\ddot{\boldsymbol{\rho}}_A = \left[\Gamma^E\right]\boldsymbol{\rho}_A + \frac{\mathbf{F}_A^k + \mathbf{F}_A^\xi + \mathbf{F}_A^b}{m_A} - \frac{\mathbf{F}_C^p}{m_T} + \mathbf{a}_A^{EPV} \tag{6.1}$$

$$\ddot{\boldsymbol{\rho}}_B = \left[\Gamma^E\right]\boldsymbol{\rho}_B + \frac{\mathbf{F}_B^k + \mathbf{F}_B^\xi + \mathbf{F}_B^b}{m_B} - \frac{\mathbf{F}_C^p}{m_T} \tag{6.2}$$

$$\boldsymbol{\rho}_C = -\frac{m_A}{m_C}\boldsymbol{\rho}_A - \frac{m_B}{m_C}\boldsymbol{\rho}_B \tag{6.3}$$

The previous equations can be written with respect to the non-inertial system <x,y,z> as follows:

$$\ddot{\mathbf{r}}_A + [\dot{\omega}]\mathbf{r}_A + [\omega][\omega]\mathbf{r}_A + 2[\omega]\dot{\mathbf{r}}_A = \left[\Gamma^E_{xyz}\right]\mathbf{r}_A + \frac{\mathbf{F}^k_A + \mathbf{F}^{\xi}_A + \mathbf{F}^b_A}{m_A} - \frac{\mathbf{F}^p_A}{m_A} + \mathbf{a}^{EPV}_A \tag{7.1}$$

$$\ddot{\mathbf{r}}_B + [\dot{\omega}]\mathbf{r}_B + [\omega][\omega]\mathbf{r}_B + 2[\omega]\dot{\mathbf{r}}_B = \left[\Gamma^E_{xyz}\right]\mathbf{r}_B + \frac{\mathbf{F}^k_B + \mathbf{F}^{\xi}_B + \mathbf{F}^b_B}{m_B} - \frac{\mathbf{F}^p_B}{m_B} \tag{7.2}$$

$$\mathbf{r}_C = -\frac{m_A}{m_C}\mathbf{r}_A - \frac{m_B}{m_C}\mathbf{r}_B \tag{7.3}$$

where $\mathbf{r}_A, \mathbf{r}_B, \mathbf{r}_C$ are the radius vectors of each individual center of mass relative to CM and projected on the body axes <xyz> and $\mathbf{F}^p_A$, $\mathbf{F}^p_B$ are possible perturbation forces acting inside the detector on the proof masses.

$[R_{IB}]$, $[R_{BI}]$ = rotation matrixes from the inertial to the <xyz> frame and viceversa.

$[\omega] = [R_{IB}]\left[\dot{R}_{BI}\right]$ = angular velocity matrix of body reference frame.

while the gravity gradient matrix in body axes is;

$$\left[\Gamma^E_{xyz}\right] = [R_{IB}]\left[\Gamma^E\right][R_{BI}] = \begin{bmatrix} g_{xx} & g_{xy} & g_{xz} \\ g_{xy} & g_{yy} & g_{yz} \\ g_{xz} & g_{yz} & g_{zz} \end{bmatrix} \tag{8}$$

For defining the orientation of the body axes with respect to the inertial axes, we adopt the rotational Euler's rotation sequence 2-1-3 that leads to relatively simple formulas for the external torques in body axes for a body spinning about an horizontal axis. Moreover, this rotation sequence avoids the trigonometric discontinuity for attitude oscillations about an horizontal axis. The physical significance of the angles in the 2-1-3 sequence with the Y inertial axis along the local vertical are ϕ = azimuth, θ = elevation and ψ = spin. After defining c = cosine and s = sine, the 2-1-3 rotation matrix yields:

$$\left[\mathbf{R}^{2-1-3}_{IB}\right] = \begin{bmatrix} r_{11} & r_{12} & r_{13} \\ r_{21} & r_{22} & r_{23} \\ r_{31} & r_{32} & r_{33} \end{bmatrix} = \begin{bmatrix} c\psi c\phi + s\psi s\theta s\phi & s\psi c\theta & -c\psi s\phi + s\psi s\theta c\phi \\ -s\psi c\phi + c\psi s\theta s\phi & c\psi c\theta & s\psi s\phi + c\psi s\theta c\phi \\ c\theta s\phi & -s\theta & c\theta c\phi \end{bmatrix} \tag{9}$$

The inverse rotation (i.e., from inertial to body axes) is $[R_{BI}] = \left[R^T_{IB}\right]$ thanks o the orthogonality o rotation matrices. After introducing Eqs. (5) and (9) in Eq. (8) we obtain:

$$
\begin{aligned}
g_{xx} &= r_{11}^2 g_{11} + r_{12}^2 g_{22} + r_{13}^2 g_{33} \\
g_{xy} &= r_{11} r_{21} g_{11} + r_{12} r_{22} g_{22} + r_{13} r_{23} g_{33} \\
g_{xz} &= r_{11} r_{31} g_{11} + r_{12} r_{22} g_{22} + r_{13} r_{33} g_{33} \\
g_{yx} &= r_{21} r_{11} g_{11} + r_{22} r_{12} g_{22} + r_{23} r_{13} g_{33} \\
g_{yy} &= r_{21}^2 g_{11} + r_{22}^2 g_{22} + r_{23}^2 g_{33} \\
g_{yz} &= r_{21} r_{31} g_{11} + r_{22} r_{32} g_{22} + r_{23} r_{33} g_{33} \\
g_{zx} &= r_{31} r_{11} g_{11} + r_{32} r_{12} g_{22} + r_{33} r_{13} g_{33} \\
g_{zy} &= r_{31} r_{21} g_{11} + r_{32} r_{22} g_{22} + r_{33} r_{23} g_{33} \\
g_{zz} &= r_{31}^2 g_{11} + r_{32}^2 g_{22} + r_{33}^2 g_{33}
\end{aligned}
\tag{10}
$$

By choosing the inertial frame such that the Y axis is parallel to $\mathbf{R}_{CM}$, the components of the Earth's gravity gradient in inertial coordinates are:

$$
\begin{aligned}
g_{11} &= -\frac{GM_E}{R_{CM}^3} \\
g_{22} &= 2\frac{GM_E}{R_{CM}^3} \\
g_{33} &= -\frac{GM_E}{R_{CM}^3}
\end{aligned}
\tag{11}
$$

The forces $\mathbf{F}^k$ and $\mathbf{F}^\xi$ transmitted by the rotational spring dash-pot system can be obtained as shown in the following. For a displacement x_A of the center of mass of A relative to C the spring dash-pot system exerts the torque (note that u_x, u_y, and u_z are the unit vectors of the body axes):

$$
\boldsymbol{\tau}_{SD} = \left(-k_{\theta}^{A}\theta_A - \xi_{\theta}^{A}\dot{\theta}_A\right)\mathbf{u}_y = \left(-\frac{k_{\theta}^{A}x_A}{b_A} - \frac{\xi_{\theta}^{A}\dot{x}_A}{b_A}\right)\mathbf{u}_y \tag{12}
$$

The corresponding force transmitted at the center of mass of A is then:

$$
\mathbf{F}_A^k + \mathbf{F}_A^\xi = \left(-\frac{k_\theta^A x_A}{b_A^2} - \frac{\xi_\theta^A \dot{x}_A}{b_A^2}\right)\mathbf{u}_x \tag{13.1}
$$

and similarly for B:

$$\mathbf{F}_B^k + \mathbf{F}_B^\xi = \left(-\frac{k_\theta^B x_B}{b_B^2} - \frac{\xi_\theta^A \dot{x}_B}{b_B^2} \right) \mathbf{u}_x \tag{13.2}$$

In order to determine the constraint force $\mathbf{F}^b$ transmitted at the center of mass we write the equation of the variation of angular momentum for body A about its center of mass projected onto body axes:

$$\frac{d\mathbf{L}_A}{dt} = [\boldsymbol{\omega}_A][I_A]\boldsymbol{\omega}_A + [I_A]\dot{\boldsymbol{\omega}}_A = b_A \mathbf{u}_z \times \mathbf{F}_A^b + \boldsymbol{\tau}_A^g \tag{14}$$

where $[I_A]$ is the inertia matrix of A in body axes and $\boldsymbol{\tau}_A^g$ is the gravitational torque acting on A. After developing Eq. (14) and taking into account Eq. (1.1) we obtain:

$$\mathbf{F}_{Ax}^b = -\left(\frac{I_A \ddot{x}_A}{b_A^2} + \frac{I_A}{b_A} \dot{\omega}_y \right)$$

and similarly for B:

$$\mathbf{F}_{Bx}^b = -\left(\frac{I_B \ddot{x}_B}{b_B^2} + \frac{I_B}{b_B} \dot{\omega}_y \right)$$

Consequently, Eqs. (7) can be rewritten as follows:

$$\ddot{\mathbf{r}}_A + [\dot{\boldsymbol{\omega}}]\mathbf{r}_A + [\boldsymbol{\omega}][\boldsymbol{\omega}]\mathbf{r}_A + 2[\boldsymbol{\omega}]\dot{\mathbf{r}}_A = \boldsymbol{\Gamma}_{xyz}^E \mathbf{r}_A - \left(\frac{k_{\boldsymbol{\theta}}^A x_A}{m_A b_A^2} + \frac{\xi_{\boldsymbol{\theta}}^A \dot{x}_A}{m_A b_A^2} \right) \mathbf{u}_x$$
$$- \left(\frac{I_A \ddot{x}_A}{m_A b_A^2} + \frac{I_A}{m_A b_A} \dot{\boldsymbol{\omega}}_y \right) \mathbf{u}_x - \frac{\mathbf{F}_A^p}{m_A} + \mathbf{a}_A^{EPV} \tag{15.1}$$

$$\ddot{\mathbf{r}}_B + [\dot{\boldsymbol{\omega}}]\mathbf{r}_B + [\boldsymbol{\omega}][\boldsymbol{\omega}]\mathbf{r}_B + 2[\boldsymbol{\omega}]\dot{\mathbf{r}}_B = \boldsymbol{\Gamma}_{xyz}^E \mathbf{r}_B - \left(\frac{k_{\boldsymbol{\theta}}^B x_B}{m_B b_B^2} + \frac{\xi_{\boldsymbol{\theta}}^B \dot{x}_B}{m_B b_B^2} \right) \mathbf{u}_x$$
$$- \left(\frac{I_B \ddot{x}_B}{m_B b_B^2} + \frac{I_B}{m_B b_B} \dot{\boldsymbol{\omega}}_y \right) \mathbf{u}_x - \frac{\mathbf{F}_B^p}{m_B} \tag{15.2}$$

$$\mathbf{r}_C = -\frac{m_A}{m_C} \mathbf{r}_A - \frac{m_B}{m_C} \mathbf{r}_B \tag{15.3}$$

At this point we shall express Eqs. (15) in terms of the stretches x_A, x_B of the springs linking A with C and B with C. Let $\mathbf{r}_{A0}, \mathbf{r}_{B0}, \mathbf{r}_{C0}$ be the radius vectors of the individual center of masses with respect to CM when the springs are at rest, then:

$$\mathbf{r}_A = \mathbf{r}_{A0} + \zeta_A \mathbf{u}_x = (r_{A0x} + \zeta_A, r_{A0y}, r_{A0z})^T \tag{16.1}$$

$$\mathbf{r}_B = \mathbf{r}_{B0} + \zeta_B \mathbf{u}_x = (r_{B0x} + \zeta_B, r_{B0y}, r_{B0z})^T \tag{16.2}$$

$$\mathbf{r}_C = -m_A/m_C(\mathbf{r}_{A0} + \zeta_A \mathbf{u}_x) - m_B/m_C(\mathbf{r}_{B0} + \zeta_B \mathbf{u}_x) \tag{16.3}$$

From Eq. (7.3) $\mathbf{r}_C$ can be expressed as:

$$\mathbf{r}_C = \mathbf{r}_{C0} - 1/m_C \,(\, m_A \zeta_A + m_B \zeta_B)\, \mathbf{u}_x \tag{17}$$

where

$$\mathbf{r}_{C0} = -1/m_C \,(m_A\, \mathbf{r}_{A0} + m_B\, \mathbf{r}_{B0}) \tag{18}$$

Let $\boldsymbol{\delta}_A$, $\boldsymbol{\delta}_B$ be position vectors from the center of mass of C to the center of mass of A and B respectively, when the springs are at rest, then:

$$\boldsymbol{\delta}_A = \mathbf{r}_{A0} - \mathbf{r}_{C0} = \mathbf{r}_{A0}(1 + m_A/m_C) + \mathbf{r}_{B0}\, m_B/m_C \tag{19.1}$$

$$\boldsymbol{\delta}_B = \mathbf{r}_{B0} - \mathbf{r}_{C0} = \mathbf{r}_{B0}(1 + m_B/m_C) + \mathbf{r}_{A0}\, m_A/m_C \tag{19.2}$$

We can now compute the stretches x_A, x_B of the two springs linking A with C and B with C as follows:

$$x_A = (r_{Ax} - r_{A0x}) - (r_{Cx} - r_{C0x}) = \zeta_A(1 + m_A/m_C) + \zeta_B\, m_B/m_C \tag{20.1}$$

$$x_B = (r_{Bx} - r_{B0x}) - (r_{Cx} - r_{C0x}) = \zeta_B(1 + m_B/m_C) + \zeta_A\, m_A/m_C \tag{20.2}$$

Solving Eq. (16) for $\mathbf{r}_{A0}, \mathbf{r}_{B0}$ and Eq. (17) for ζ_A, ζ_B yields:

$$\mathbf{r}_{A0} = \boldsymbol{\delta}_A(m_B + m_C)/m_T - \boldsymbol{\delta}_B\, m_B/m_T \tag{21.1}$$

$$\mathbf{r}_{B0} = \boldsymbol{\delta}_B(m_A + m_C)/m_T - \boldsymbol{\delta}_A\, m_A/m_T \tag{21.2}$$

$$\zeta_A = x_A(m_B + m_C)/m_T - x_B\, m_B/m_T \tag{21.3}$$

$$\zeta_B = x_B(m_A + m_C)/m_T - x_A\, m_A/m_T \tag{21.4}$$

We can now write the equations of motions of the centers of mass in term of the variables $x_A(t)$ and $x_B(t)$ and the parameters $\boldsymbol{\delta}_A$, $\boldsymbol{\delta}_B$:

$$\ddot{\mathbf{r}}_A + [\dot{\boldsymbol{\omega}}]\mathbf{r}_A + [\boldsymbol{\omega}][\boldsymbol{\omega}]\mathbf{r}_A + 2[\boldsymbol{\omega}]\dot{\mathbf{r}}_A = \boldsymbol{\Gamma}^E_{xyz}\mathbf{r}_A - \left(\frac{k^A_{\theta} x_A}{m_A b_A{}^2} + \frac{\xi^A_{\theta}\dot{x}_A}{m_A b_A{}^2}\right)\mathbf{u}_x$$
$$-\left(\frac{I_A \ddot{x}_A}{m_A b_A{}^2} + \frac{I_A}{m_A b_A}\dot{\boldsymbol{\omega}}_y\right)\mathbf{u}_x - \frac{\mathbf{F}^p_A}{m_A} + \mathbf{a}^{EPV}_A \qquad (22.1)$$

$$\ddot{\mathbf{r}}_B + [\dot{\boldsymbol{\omega}}]\mathbf{r}_B + [\boldsymbol{\omega}][\boldsymbol{\omega}]\mathbf{r}_B + 2[\boldsymbol{\omega}]\dot{\mathbf{r}}_B = \boldsymbol{\Gamma}^E_{xyz}\mathbf{r}_B - \left(\frac{k^B_{\theta} x_B}{m_B b_B{}^2} + \frac{\xi^B_{\theta}\dot{x}_B}{m_B b_B{}^2}\right)\mathbf{u}_x$$
$$-\left(\frac{I_B \ddot{x}_B}{m_B b_B{}^2} + \frac{I_B}{m_B b_B}\dot{\boldsymbol{\omega}}_y\right)\mathbf{u}_x - \frac{\mathbf{F}^p_B}{m_B} \qquad (22.2)$$

$$\mathbf{r}_C = -\frac{m_A}{m_C}\mathbf{r}_A - \frac{m_B}{m_C}\mathbf{r}_B \qquad (22.3)$$

where

$$\mathbf{r}_A = \boldsymbol{\delta}_A(m_B+m_C)/m_T - \boldsymbol{\delta}_B m_B/m_T + (x_A(m_B+m_C)/m_T - x_B m_B/m_T)\mathbf{u}_x \qquad (23.1)$$

$$\mathbf{r}_B = \boldsymbol{\delta}_B(m_A+m_C)/m_T - \boldsymbol{\delta}_A m_A/m_T + (x_B(m_A+m_C)/m_T - x_A m_A/m_T)\mathbf{u}_x \qquad (23.2)$$

After substituting Eqs. (23) into Eqs. (22), considering the x components of the Eqs. (22.1) and (22.2) we obtain, for $m_C >> m_A$ and m_B (as it is indeed the case) and $\mathbf{F}^p_A = \mathbf{F}^p_B = 0$:

$$p_A \ddot{x}_A - \left(\omega_y^2 + \omega_z^2 - g_{xx}\right)x_A + \frac{k_{\theta A}}{m_A b_A{}^2}x_A + \frac{\xi_{\zeta A}}{m_A b_A{}^2}\dot{x}_A$$
$$+\left(\delta_{Az} - \frac{I_A}{m_A b_A}\right)\dot{\omega}_y - \delta_{Ay}\dot{\omega}_z - \delta_{Ax}\omega_y^2 - \delta_{Ax}\omega_z^2 + \delta_{Az}\omega_x\omega_z + \delta_{Ay}\omega_x\omega_y \qquad (24.1)$$
$$-\delta_{Az}g_{xz} - \delta_{Ay}g_{xy} + \delta_{Ax}g_{xx} - a^{EPV}_x = 0$$

$$p_B \ddot{x}_B - \left(\omega_y^2 + \omega_z^2 - g_{xx}\right)x_B + \frac{k_{\theta B}}{m_B b_B{}^2}x_B + \frac{\xi_{\zeta B}}{m_B b_B{}^2}\dot{x}_B$$
$$+\left(\delta_{Bz} - \frac{I_B}{m_B b_B}\right)\dot{\omega}_y - \delta_{By}\dot{\omega}_z - \delta_{Bx}\omega_y^2 - \delta_{Bx}\omega_z^2 + \delta_{Bz}\omega_x\omega_z + \delta_{By}\omega_x\omega_y \qquad (24.2)$$
$$-\delta_{Bz}g_{xz} - \delta_{By}g_{xy} + \delta_{Bx}g_{xx} = 0$$

where

$$p_A = \frac{m_A b_A^{\,2} + I_A}{m_A b_A^{\,2}}$$

$$p_B = \frac{m_B b_B^{\,2} + I_B}{m_B b_B^{\,2}}$$

Attitude equation of motion of the whole detector

The attitude equations of motion can be derived based on the conservation of angular momentum. Let $[I_A]$, $[I_B]$, $[I_C]$ be the inertia matrices of the three bodies in body axes <x,y,z. The total angular momentum of the system, projected upon <x,y,z> is written using the translation theorem of the angular momentum as follows:

$$\mathbf{L} = [I_A]\boldsymbol{\omega}_A + [I_B]\boldsymbol{\omega}_B + [I_C]\boldsymbol{\omega}_C + [R_{IB}]\left(\boldsymbol{\omega}_A \times m_A\dot{\boldsymbol{\omega}}_A + \boldsymbol{\omega}_B \times m_B\dot{\boldsymbol{\omega}}_B + \boldsymbol{\omega}_C \times m_C\dot{\boldsymbol{\omega}}_C\right) \quad (25)$$

After some algebraic manipulations the derivative of the angular momentum projected onto body axes yield:

$$\begin{aligned}\frac{d\mathbf{L}}{dt} = {} & [I_A]\dot{\boldsymbol{\omega}}_A + [I_B]\dot{\boldsymbol{\omega}}_B + [I_C]\dot{\boldsymbol{\omega}}_C + [\boldsymbol{\omega}][I_A]\boldsymbol{\omega}_A + [\boldsymbol{\omega}][I_B]\boldsymbol{\omega}_B + [\boldsymbol{\omega}][I_C]\boldsymbol{\omega}_C \\ & + m_A\mathbf{r}_A \times \left(\ddot{\mathbf{r}}_A + [\dot{\boldsymbol{\omega}}]\mathbf{r}_A + [\boldsymbol{\omega}][\boldsymbol{\omega}]\mathbf{r}_A + 2[\boldsymbol{\omega}]\dot{\mathbf{r}}_A\right) \\ & + m_B\mathbf{r}_B \times \left(\ddot{\mathbf{r}}_B + [\dot{\boldsymbol{\omega}}]\mathbf{r}_B + [\boldsymbol{\omega}][\boldsymbol{\omega}]\mathbf{r}_B + 2[\boldsymbol{\omega}]\dot{\mathbf{r}}_B\right) \\ & + m_C\mathbf{r}_C \times \left(\ddot{\mathbf{r}}_C + [\dot{\boldsymbol{\omega}}]\mathbf{r}_C + [\boldsymbol{\omega}][\boldsymbol{\omega}]\mathbf{r}_C + 2[\boldsymbol{\omega}]\dot{\mathbf{r}}_C\right)\end{aligned} \quad (26)$$

After taking into account Eqs. (22), Eq. (26) in body axes yields:

$$\begin{aligned}& [I_A]\dot{\boldsymbol{\omega}}_A + [I_B]\dot{\boldsymbol{\omega}}_B + [I_C]\dot{\boldsymbol{\omega}}_C + [\boldsymbol{\omega}][I_A]\boldsymbol{\omega}_A + [\boldsymbol{\omega}][I_B]\boldsymbol{\omega}_B + [\boldsymbol{\omega}][I_A]\boldsymbol{\omega}_B \\ & + \left(\frac{m_A^{\,2} + m_A m_C}{m_C}\mathbf{r}_A + \frac{m_A m_B}{m_C}\mathbf{r}_B\right) \\ & \times \left(\left[\Gamma^E_{xyz}\right]\mathbf{r}_A - \left(\frac{k^A_{\theta} x_A}{m_A b_A^{\,2}} + \frac{\xi^A_{\theta}\dot{x}_A}{m_A b_A^{\,2}}\right)\mathbf{u}_x - \left(\frac{I_A\ddot{x}_A}{m_A b_A^{\,2}} + \frac{I_A}{m_A b_A}\dot{\boldsymbol{\omega}}_y\right)\mathbf{u}_x - \frac{\mathbf{F}^p_A}{m_A}\right) \\ & + \left(\frac{m_B^{\,2} + m_B m_C}{m_C}\mathbf{r}_B + \frac{m_A m_B}{m_C}\mathbf{r}_A\right) \\ & \times \left(\left[\Gamma^E_{xyz}\right]\mathbf{r}_B - \left(\frac{k^B_{\theta} x_B}{m_B b_B^{\,2}} + \frac{\xi^B_{\theta}\dot{x}_B}{m_B b_B^{\,2}}\right)\mathbf{u}_x - \left(\frac{I_B\ddot{x}_B}{m_B b_B^{\,2}} + \frac{I_B}{m_B b_B}\dot{\boldsymbol{\omega}}_y\right)\mathbf{u}_x - \frac{\mathbf{F}^p_B}{m_B}\right) = \boldsymbol{\tau}^{GG}\end{aligned} \quad (27)$$

where $\boldsymbol{\tau}^{GG}$ is the gravitational torque on the whole instrument package.

Numerical cases

We integrated numerically the dynamics equations (both the attitude equations of the instrument package and the motion of the proof masses inside the detector) derived previously for roto-translational detector configuration. This configuration has appealing features from the point of view of constructing the suspensions of the proof masses and the ability of ground testing through gravitational excitation of the proof masses (see IFSI contribution Section). The new differential detector prototype was designed according to this configuration.

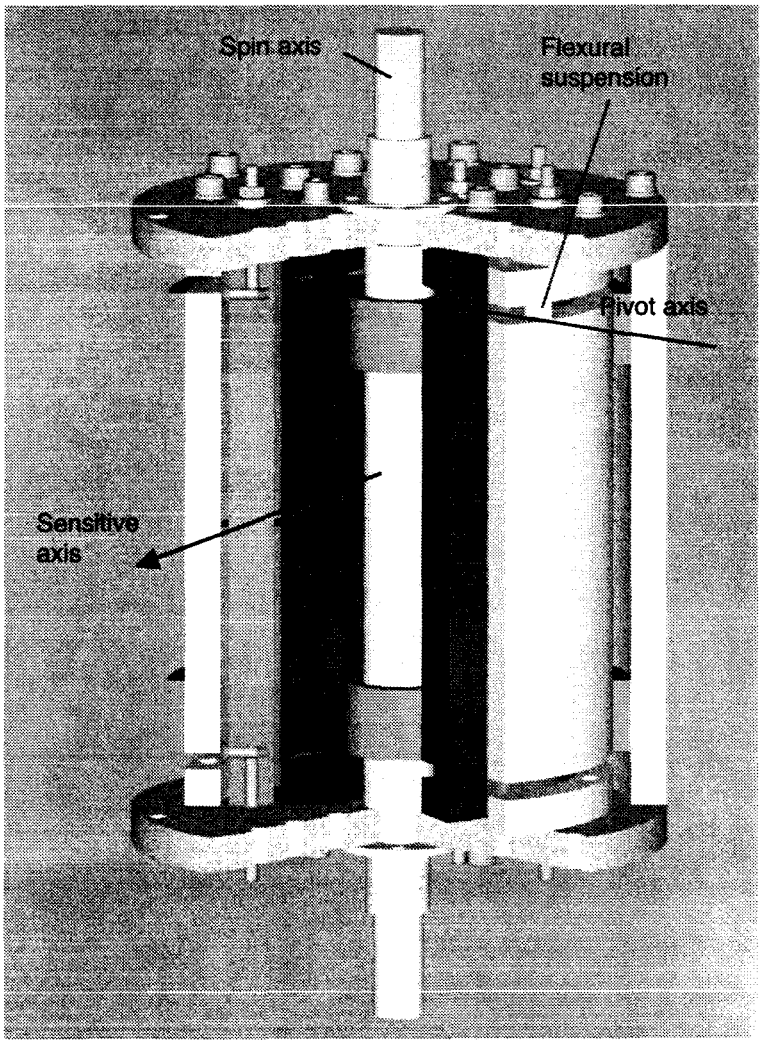

Figure 3 New acceleration detector prototype that has a roto-translational configuration.

The suspensions are flexural suspensions (shaped like short flat flexures) that connect the base of each cylindrical proof mass to the detector's housing. The flexures are easy to

manufacture and provide an excellent frequency separation between their sensitive modal frequency (i.e., the one that bends the flexures) and any other modal frequency (see Ref. i). The acceleration detector prototype (see Figure 3) is shown here because it provides a good example of a roto-translational configuration.

We explored cases with a precession frequency of the instrument package within the 0.2-0.4 Hz window that proved optimal for the translational detector (see Ref. i). As a general comment of simulation results, the roto-translational configuration has more internal dynamics than the translational configuration. The offsets between pivot axes and respective CMs of the proof masses couple the attitude dynamics of the instrument package to the internal dynamics of the proof masses more than with suspensions that are (ideally) located at the CMs of the proof masses. Moreover, the roto-translational configuration show the same sensitivity to gravity gradient *forces* (more on this point later) of the translational detector. This implies that the roto-translational configuration must satisfy the same tight requirement on the orientation of the spin axis of the translational configuration. After calling θ the elevation angle of the spin axis with respect to the horizontal plane and δ_z the centering error of the proof masses along the spin axis, then we must have $\delta_z\theta < 1$ micronxdeg. This requirement then drives the design of the leveling and release mechanism that needs to provide elevation angle errors less than 0.1 deg for centering errors of the proof masses equal to 10 microns.

Unlike the translational detector configuration, the roto-translational configuration is also affected by inequalities between the moments of inertia about the pivot axes of the two proof masses. Unequal moments of inertia will produce slightly different rotations of the proof masses that are detected as a differential output at various frequencies

A sample of simulations for a precession frequency of 0.2 Hz is shown in the following. Figure 4 presents the results for a baseline case with pivot offsets equal to 3.2 cm and relatively small centering errors of the proof masses. The output at low frequency is dominated by the precession dynamics-related noise that exhibits two peaks at the precession frequency and twice the precession frequency. Even after removal of those two harmonics by least-square fitting of the output in the time domain, the dynamics-related noise level at the signal frequency of 0.5 Hz is about $5\text{x}10^{-15}$ g. A better attenuation technique of the colored noise could improve the situation but, as shown later on, the dynamics-noise can be much more drastically reduced by changing the detector's configuration. Note also the harmonic peak at 1 Hz which is associated with the gravity gradient forces due to the centering error of the proof masses.

Subsequently, we have added an EP violation signal of $2\text{x}10^{-14}$ g to the previous case and the results are shown in Figure 5. The EP violation signal can be barely resolved after having filtered out the colored noise at low frequency as shown in the last panel of Figure 5. An EP violation signal of $5\text{x}10^{-14}$ g can be more clearly resolved but this is well above the sensitivity threshold level that we desire to achieve. The purely rotational configuration of the detector will cure this problem of high dynamics noise.

Damped 25% for 5 s, Elastic freq. = 3 Hz; Ix = 0.3; Iy = 0.3, Iz = 0.18 (0.2 Hz prograde)
OmegaX = 0.1deg/s, Elevation angle = 0 deg; Spin = 0.5 Hz; Rotation Seq 2-1-3, SmoothDamp = 0.04
del-xA = del-yA= del-zA = 1 μm; del-xB = del-yB= del-zB = -1 μm; Pivots = 0.032cm
Signal = 0 g; White Noise = 0 g; Initial xA = xB = ±10 μm; Equations (8/17/04)

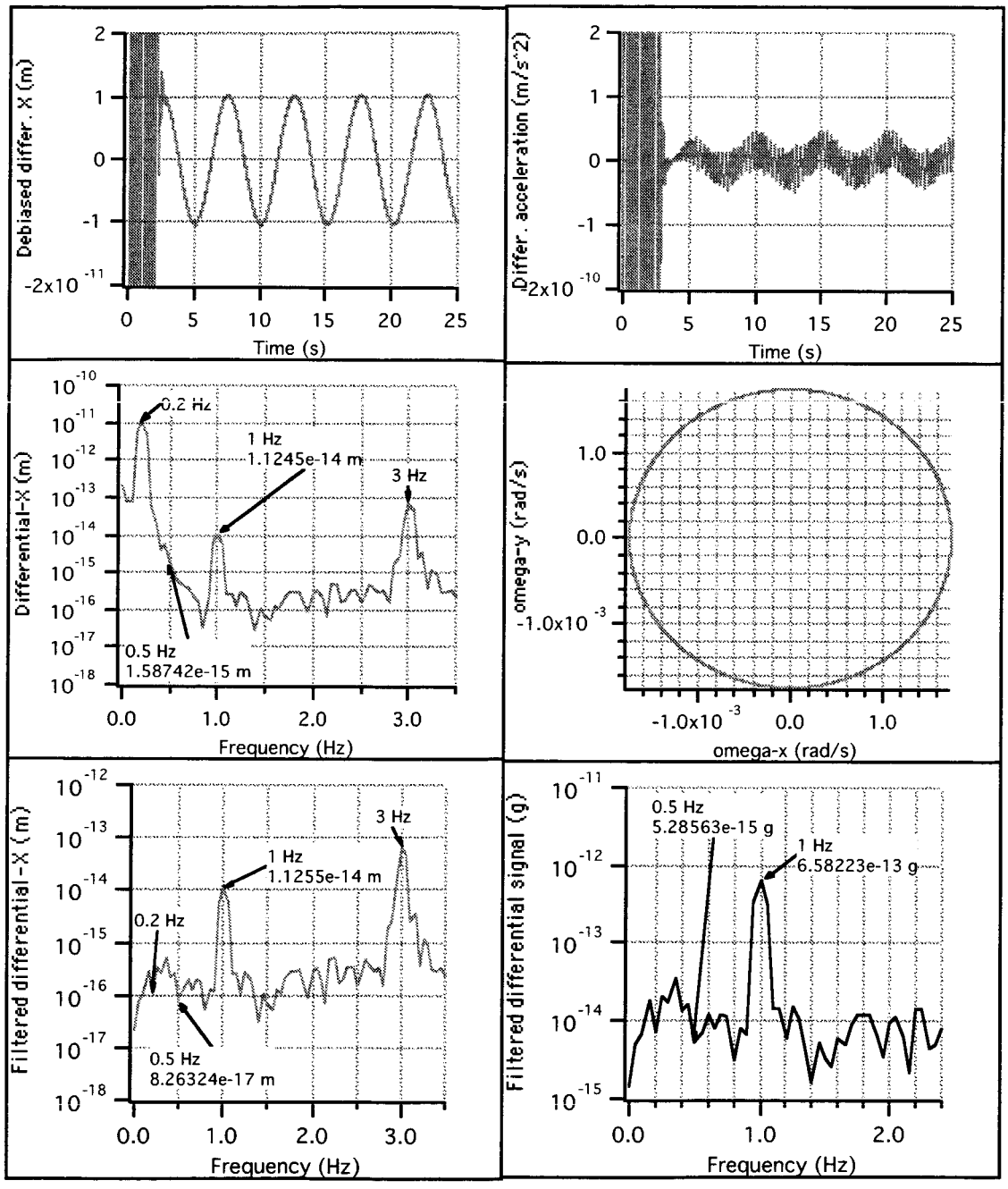

Figure 4 Simulation results for a roto-translational configuration with instrument package's precession frequency = 0.2 Hz and No EP violation signal.

Damped 25% for 5 s, Elastic freq. = 3 Hz; Ix = 0.3; Iy = 0.3, Iz = 0.18 (0.2 Hz prograde)
OmegaX = 0.1deg/s, Elevation angle = 0.1 deg; Spin = 0.5 Hz; Rotation Seq 2-1-3, SmoothDamp = 0.04
del-xA = del-yA= del-zA = 1 μm; del-xB = del-yB= del-zB = -1 μm; Pivots = 0.032cm
Signal = 2x10^-14 g; White Noise = 0 g; Initial xA = xB = ±10 μm; Equations (8/17/04)

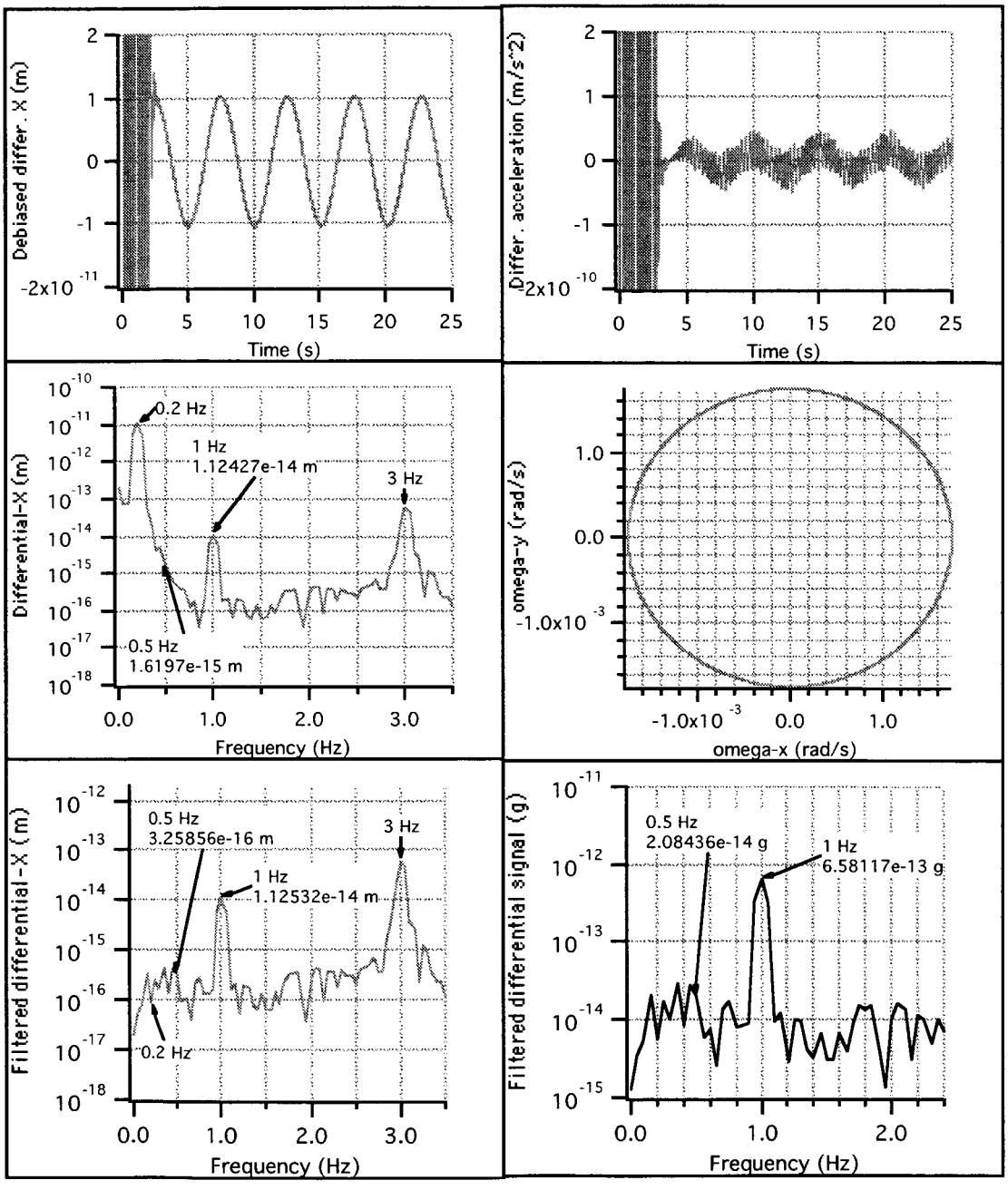

Figure 5 Simulation results for a roto-translational configuration with instrument package's precession frequency = 0.2 Hz and an EP violation signal = 2×10^{-14} g.

Damped 25% for 5 s, Elastic freq. = 3 Hz; Ix = 0.3; Iy = 0.3, Iz = 0.18 (0.2 Hz prograde)
OmegaX = 0.1deg/s, Elevation angle = 0.1 deg; Spin = 0.5 Hz; Rotation Seq 2-1-3, SmoothDamp = 0.04
del-xA = del-yA= del-zA = 1 μm; del-xB = del-yB= del-zB = -1 μm; Pivots = 0.032cm
Signal = 5x10^-14 g; White Noise = 0 g; Initial xA = xB = ±10 μm; Equations (8/17/04)

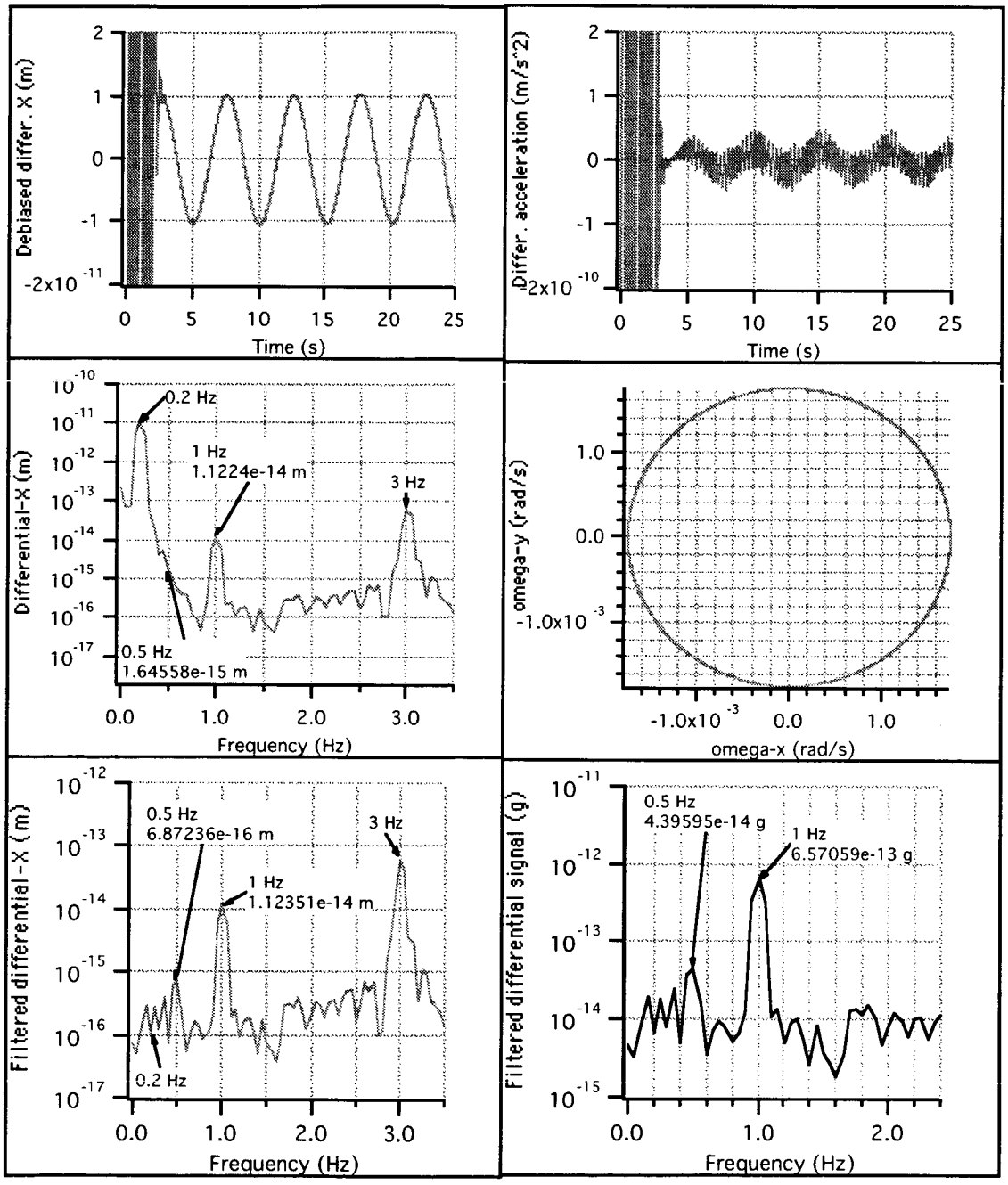

Figure 6 Simulation results for a roto-translational configuration with instrument package's precession frequency = 0.2 Hz and an EP violation signal = 5×10^{-14} g.

Purely rotational configuration

Detector configuration with pivot axes perpendicular to spin axis

In a purely rotational configuration, the proof masses are constrained by the pivot axes (located at the CMs of the proof masses) to rotate with respect to the housing of the detector. A schematic of a configuration with the pivot axes of the proof masses perpendicular to the detector's spin axis is shown in Figure 7.

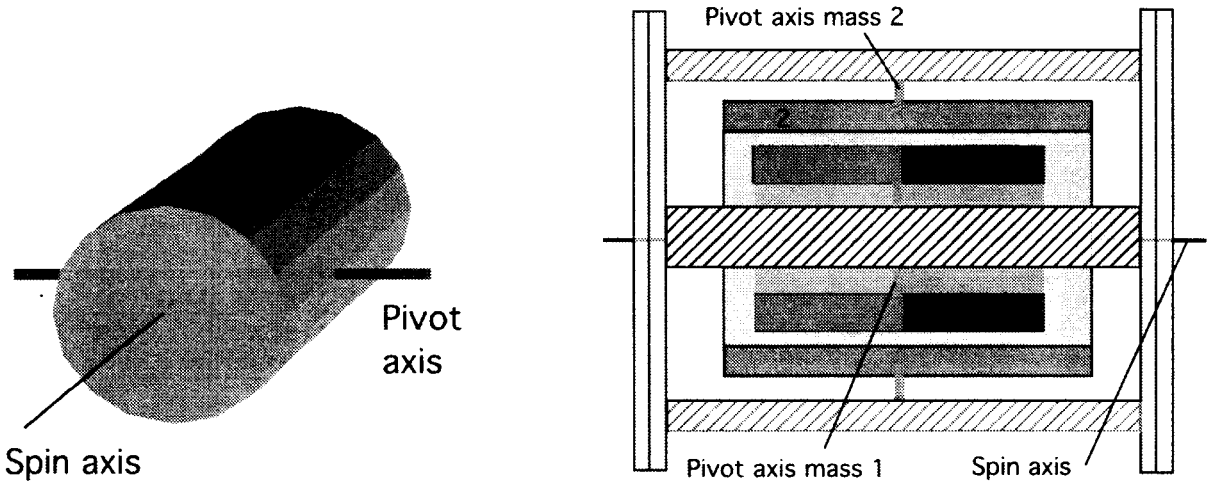

Figure 7 Schematic of rotational detector configurations with pivot axes of proof masses perpendicular to the detector's spin axis: (a) 3-D view of one proof mass; and (b) geometrical arrangement of proof masses inside the detector.

In this rotational configuration, one proof mass (labeled 1) is the "EPV-sensitive" mass that, thanks to its design consisting of two halves of different materials, is able to sense an EP violation force. Note also that an EPV force will produce a relatively strong torque (see later on) when compared to other perturbation torques thanks to its sizeable arm length with respect to the pivot axis. The second proof mass (labeled 2) is the "dynamical-reference" mass made of one of the materials of the first mass. As the name implies, the role of this proof mass is to move very closely (ideally in unison) to the other proof mass. This proof mass enables the removal of most of the instrument package dynamics from the detector's output by differencing the individual motions of the two proof masses.

Motion of proof masses with respect to detector's housing

Let us consider a set of three rigid bodies A, B, C constrained to one another in such a way that the relative motion of A with respect to C is a pure rotation around a pivot axis $<d_A>$ and the relative motion of B with respect to C is a pure rotation around a pivot axis $<d_B>$ with $<d_A>$ and $<d_B>$ parallel to one another.

This time the pivot axes are ideally coincident with the CMs of the proof masses except for the construction errors. Let A and B be linked with C through a torsional spring dashpot system around the axes $<d_A>$ and $<d_B>$ characterized by elastic and damping coefficients (k_A, ξ_A) and (k_B, ξ_B) respectively.

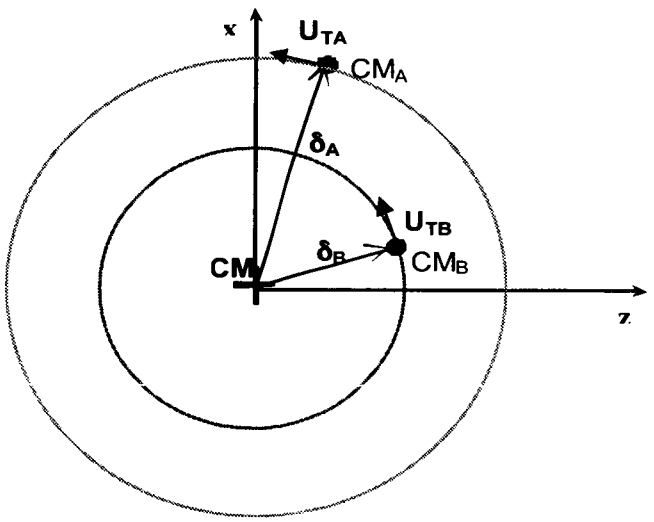

Figure 8 Relative position of individual centers of mass for pivot axis perpendicular to z-axis.

Let <x,y,z> be a reference system centered at the global center of mass CM of the system composed by the three rigid bodies, which we assume coincident with the center of mass of body C, i.e., after having assumed that $m_C >> m_A$ and m_B. Let y be parallel to $<d_A>$ and $<d_B>$ (the y axis is exiting the page in Figure 8), z parallel to the central symmetry axis of body C, and x right-handed with y and z. A schematic of the relative positions of the centers of mass, inclusive of the construction errors δ_A and δ_B, is shown in Figure 8.

The tangential unit vectors $\mathbf{u}_{TA}$ and $\mathbf{u}_{TB}$ can be written as:

$$\mathbf{u}_{TA} = \frac{1}{\boldsymbol{\delta}_{Axz}}\left(\boldsymbol{\delta}_{Ax}, 0, -\boldsymbol{\delta}_{Az}\right)^T$$

$$\mathbf{u}_{TB} = \frac{1}{\boldsymbol{\delta}_{Bxz}}\left(\boldsymbol{\delta}_{Bx}, 0, -\boldsymbol{\delta}_{Bz}\right)^T$$

with

$$\boldsymbol{\delta}_{Axz} = \sqrt{\boldsymbol{\delta}_{Ax}^{\,2} + \boldsymbol{\delta}_{Az}^{\,2}}; \qquad \delta_{Bxz} = \sqrt{\delta_{Bx}^{\,2} + \delta_{Bz}^{\,2}}$$

Let $\boldsymbol{\omega}_C = (\omega_x,\omega_y,\omega_z)^T$ be the angular velocity vector of body C and, consequently, of the reference frame <x,y,z>. The angular velocities of body A and B, projected on <x,y,z> are:

$$\boldsymbol{\omega}_A = \left(\omega_x,\omega_y + \frac{\dot{\eta}_A}{\delta_{Axz}},\omega_z\right)^T \tag{28.1}$$

$$\boldsymbol{\omega}_B = \left(\omega_x,\omega_y + \frac{\dot{\eta}_B}{\delta_{Bxz}},\omega_z\right)^T \tag{28.2}$$

where η_A and η_B are the tangential displacements of the center of masses of A and B. with respect to the initial geometry conditions drawn in Fig. 8. The equations of motion of the system written with respect to an inertial system centered at the Earth's center are:

$$m_A(\ddot{\mathbf{R}}_{CM} + \ddot{\boldsymbol{\rho}}_A) = \mathbf{F}_A^g + \mathbf{F}_A^k + \mathbf{F}_A^{\xi} + \mathbf{F}_A^b + m_A \cdot \mathbf{a}_A^{EPV} \tag{29.1}$$

$$m_B(\ddot{\mathbf{R}}_{CM} + \ddot{\boldsymbol{\rho}}_B) = \mathbf{F}_B^g + \mathbf{F}_B^k + \mathbf{F}_B^{\xi} + \mathbf{F}_B^b \tag{29.2}$$

where $\boldsymbol{\rho}$ is the radius vector of each individual center of mass relative to CM and projected on the inertial system, $\mathbf{R}_{CM}$ is the radius vector of CM from the earth center projected on the inertial system, $\mathbf{F}^g$ is the earth gravity field force, $\mathbf{F}^k$ the equivalent force of the internal spring and $\mathbf{F}^{\xi}$ the equivalent force of the internal damper acting on each mass. $\mathbf{F}^b$ is the force transmitted to each mass from the pivotal constraint as a consequence of the rigid body attitude motion of A and B. We also added the acceleration $\mathbf{a}^{EPV}$ acting on the mass A to simulate a violation of the equivalent principle. The equations of motion of the system center of mass are:

$$\ddot{\mathbf{R}}_{CM} = -\frac{\mu_E \mathbf{R}_{CM}}{\mathbf{R}_{CM}^3} + \frac{\mathbf{F}_C^p}{m_T} \tag{30}$$

where $\mathbf{F}_C^p$ is a perturbing force acting on the external case during free fall and m_T the total mass of the system. The gravitational forces, appearing in Eqs. (29), can be expressed like Eqs. (4) of the previous subsection.

After plugging Eqs. (30) into Eqs. (29) we obtain:

$$\ddot{\rho}_A = \left[\Gamma^E\right]\rho_A + \frac{\mathbf{F}_A^k + \mathbf{F}_A^{\xi} + \mathbf{F}_A^b}{m_A} - \frac{\mathbf{F}_C^p}{m_T} + \mathbf{a}_A^{EPV} \tag{31.1}$$

$$\ddot{\boldsymbol{\rho}}_B = \boldsymbol{\Gamma}^E\boldsymbol{\rho}_B + \frac{\mathbf{F}_B^k + \mathbf{F}_B^{\xi} + \mathbf{F}_B^b}{m_B} - \frac{\mathbf{F}_C^p}{m_T} \tag{31.2}$$

The previous equations can be written with respect to body axes <x,y,z> as follows:

$$\ddot{\mathbf{r}}_A + [\dot{\omega}]\mathbf{r}_A + [\omega][\omega]\mathbf{r}_A + 2[\omega]\dot{\mathbf{r}}_A = \left[\Gamma^E_{xyz}\right]\mathbf{r}_A + \frac{\mathbf{F}^k_A + \mathbf{F}^\xi_A + \mathbf{F}^b_A}{m_A} - \frac{\mathbf{F}^p_A}{m_A} + \mathbf{a}^{EPV}_A \tag{32.1}$$

$$\ddot{\mathbf{r}}_B + [\dot{\omega}]\mathbf{r}_B + [\omega][\omega]\mathbf{r}_B + 2[\omega]\dot{\mathbf{r}}_B = \left[\Gamma^E_{xyz}\right]\mathbf{r}_B + \frac{\mathbf{F}^k_B + \mathbf{F}^\xi_B + \mathbf{F}^b_B}{m_B} - \frac{\mathbf{F}^p_B}{m_B} \tag{32.2}$$

where $\mathbf{r}_A$,$\mathbf{r}_B$ are the radius vectors of each individual center of mass relative to CM and projected on the body frame; R_{IB}, R_{BI} are the rotation matrixes from the inertial to the body frame and viceversa, $[\omega] = \left[R_{IB}\right]\left[\dot{R}_{BI}\right]$ is angular velocity matrix of the body frame, and $\left[\Gamma^E_{xyz}\right]$ is the Earth's gravity gradient matrix projected in body frame (see previous subsection for details). The forces $\mathbf{F}^k$ and $\mathbf{F}^\xi$ transmitted by the rotational spring dash-pot system can be obtained by following the same procedure outlined in the previous subsection.

A rotation of the proof mass A, $\boldsymbol{\theta}_\mathbf{A} = \boldsymbol{\eta}_\mathbf{A}/\boldsymbol{\delta}_{Axz}$ with respect to C forces the spring dash-pot system exerts the torque:

$$\boldsymbol{\tau}_{\mathrm{SD}} = \left(-k^A_{\boldsymbol{\theta}}\boldsymbol{\theta}_A - \xi^A_{\boldsymbol{\theta}}\dot{\boldsymbol{\theta}}_A\right)\mathbf{u}_y \tag{33}$$

The corresponding force transmitted at the center of mass of A is then:

$$\mathbf{F}^k_A + \mathbf{F}^\xi_A = \left(-\frac{k^A_{\boldsymbol{\theta}}\boldsymbol{\theta}_A}{\boldsymbol{\delta}_{Axz}} - \frac{\xi^A_{\boldsymbol{\theta}}\dot{\boldsymbol{\theta}}_A}{\boldsymbol{\delta}_{Axz}}\right)\mathbf{u}_{TA} \tag{34}$$

and similarly for B with $\boldsymbol{\theta}_B = \boldsymbol{\eta}_B/\boldsymbol{\delta}_{Bxz}$:

$$\mathbf{F}^k_B + \mathbf{F}^\xi_B = \left(-\frac{k^A_{\boldsymbol{\theta}}\boldsymbol{\theta}_B}{\boldsymbol{\delta}_{Bxz}} - \frac{\xi^A_{\boldsymbol{\theta}}\dot{\boldsymbol{\theta}}_B}{\boldsymbol{\delta}_{Bxz}}\right)\mathbf{u}_{TB}$$

In order to determine the constraint force $\mathbf{F}^b$ transmitted at the center of mass we write down the equation of the variation of angular momentum for body A about its center of mass projected onto body axes:

$$\frac{d\mathbf{L}_A}{dt} = [\boldsymbol{\omega}_A][I_A]\boldsymbol{\omega}_A + [I_A]\dot{\boldsymbol{\omega}}_A = \mathbf{r}_A \times \mathbf{F}^b_A + \boldsymbol{\tau}^g_A \tag{35}$$

where $[I_A]$ is the inertia matrix of A in body axes and $\boldsymbol{\tau}^g_A$ is the gravitational torque acting on A. Consequently, after developing Eq. (35) and taking into account Eq. (28.1) we obtain:

$$\mathbf{F}^b_A = -\left(\frac{I_A\ddot{\boldsymbol{\theta}}_A}{\boldsymbol{\delta}_{Axz}} + \frac{I_A}{\boldsymbol{\delta}_{Axz}}\dot{\boldsymbol{\omega}}_y\right)\mathbf{u}_{TA}$$

and similarly for B:

$$\mathbf{F}_B^b = -\left(\frac{I_B\ddot{\boldsymbol{\theta}}_B}{\boldsymbol{\delta}_{Bxz}} + \frac{I_B}{\boldsymbol{\delta}_{Bxz}}\dot{\boldsymbol{\omega}}_y\right)\mathbf{u}_{TB}$$

Hence Eqs. (32) can be rewritten as follows:

$$\ddot{\mathbf{r}}_A + [\dot{\omega}]\mathbf{r}_A + [\omega][\omega]\mathbf{r}_A + 2[\omega]\dot{\mathbf{r}}_A = \left[\boldsymbol{\Gamma}_{xyz}^E\right]\mathbf{r}_A - \left(\frac{k_\theta^A\theta_A}{m_A\delta_{Axz}} + \frac{\xi_\theta^A\dot{\theta}_A}{m_A\delta_{Axz}}\right)\mathbf{u}_{TA}$$
$$-\left(\frac{I_A\ddot{\theta}_A}{m_A\delta_{Axz}} + \frac{I_A}{m_A\delta_{Axz}}\dot{\omega}_y\right)\mathbf{u}_{TA} - \frac{\mathbf{F}_A^p}{m_A} + \mathbf{a}_A^{EPV} \tag{36.1}$$

$$\ddot{\mathbf{r}}_B + [\dot{\omega}]\mathbf{r}_B + [\omega][\omega]\mathbf{r}_B + 2[\omega]\dot{\mathbf{r}}_B = \left[\boldsymbol{\Gamma}_{xyz}^E\right]\mathbf{r}_B - \left(\frac{k_\theta^B\theta_B}{m_B\delta_{Bxz}} + \frac{\xi_\theta^B\dot{\theta}_B}{m_B\delta_{Bxz}}\right)\mathbf{u}_{TB}$$
$$-\left(\frac{I_B\ddot{\theta}_B}{m_B\delta_{Bxz}} + \frac{I_B}{m_B\delta_{Bxz}}\dot{\omega}_y\right)\mathbf{u}_{TB} - \frac{\mathbf{F}_B^p}{m_B} \tag{36.2}$$

$$\mathbf{r}_C = \mathbf{0} \tag{36.3}$$

At this point we can express Eqs. (36) in terms of the stretches x_A, x_B of the springs linking A and B with C, as follows:

$$\mathbf{r}_A = \boldsymbol{\delta}_A + \eta_A\mathbf{u}_{TA} = \left(\boldsymbol{\delta}_{Ax} + \boldsymbol{\theta}_A\boldsymbol{\delta}_{Az}, 0, \boldsymbol{\delta}_{Az} - \boldsymbol{\theta}_A\boldsymbol{\delta}_{Ax}\right)^T \tag{37.1}$$

$$\mathbf{r}_B = \boldsymbol{\delta}_B + \eta_B\mathbf{u}_{TB} = \left(\boldsymbol{\delta}_{Bx} + \boldsymbol{\theta}_B\boldsymbol{\delta}_{Bz}, 0, \boldsymbol{\delta}_{Bz} - \boldsymbol{\theta}_B\boldsymbol{\delta}_{Bx}\right)^T \tag{37.2}$$

Finally, projecting Eq. (36.1) of proof mass A along the tangential direction $\mathbf{u}_{TA}$ and dividing by the arm length δ_{Axz} in order to express the equation in terms of the relative rotation θ_A:

$$\ddot{\theta}_A + C_2\dot{\theta}_A + C_3\theta_A + \dot{\omega}_y$$
$$+C_4\left(\dot{\omega}_x + \omega_y\omega_z - g_{yz}\right) + C_6\left(\dot{\omega}_z + \omega_x\omega_y + g_{xy}\right) \tag{38}$$
$$+C_7\left(\omega_x^2 - \omega_z^2 - g_{xx} + g_{zz}\right) + C_9\left(\omega_x\omega_z - g_{xz}\right) = C_{10}\tau_{Ay}^{GG} + C_{10}\tau_{Ay}^{EPV}$$

where

$$C_2 = \boldsymbol{\xi}_A/\tilde{I}_{Ay}$$

$$C_3 = \frac{m_A}{\tilde{I}_{Ay}}\left(\frac{K_{\boldsymbol{\theta}Ay}}{m_A} - \boldsymbol{\delta}_{Az}^2\boldsymbol{\omega}_z^2 - 2\boldsymbol{\omega}_x\boldsymbol{\omega}_z\boldsymbol{\delta}_{Ax}\boldsymbol{\delta}_{Az}\right)$$

$$C_4 = -\frac{m_A}{\tilde{I}_{Ay}}\delta_{Ax}\delta_{Ay}$$

$$C_6 = -\frac{m_A}{\tilde{I}_{Ay}}\delta_{Ay}\delta_{Az} \qquad (39)$$

$$C_7 = \frac{m_A}{\tilde{I}_{Ay}}\delta_{Ax}\delta_{Az}$$

$$C_9 = \frac{m_A}{\tilde{I}_{Ay}}\left(\delta_{Az}^2 - \delta_{Ax}^2\right)$$

$$C_{10} = \frac{m_A}{\tilde{I}_{Ay}}$$

with $\tilde{I}_{Ay} = I_{Ay} + m_A\delta_{Axz}^2$ and $\delta_{Axz} = \sqrt{\delta_{Ax}{}^2 + \delta_{Az}{}^2}$.

The equation relative to the rotation θ_B of mass B are written by simply replacing the subscript A with B and setting the equivalence violation torque to zero. Note that the assumption of $m_C >> m_A, m_B$ eliminates the cross-coupling from the two equations of motion.

Effect of gravity gradient torques

The attitude equations of motion are not shown for the purely rotational case because their derivation follows the same strategy outlined previously for the roto-translational detector. However, there are important points to be made about the effects of the gravity gradient torque acting on the instrument package versus the Equivalence Principle violation (EPV) torque. The components in body axes of the gravity gradient torque, for the 2-1-3 Euler's rotation sequence, are:

$$\tau_x^{GG} = -3\frac{GM}{R^3}\left(I_z - I_y\right)\cos\psi\cos\theta\sin\theta$$

$$\tau_y^{GG} = -3\frac{GM}{R^3}\left(I_x - I_z\right)\sin\psi\cos\theta\sin\theta \qquad (40)$$

$$\tau_z^{GG} = 3\frac{GM}{R^3}\left(I_y - I_x\right)\sin\psi\cos\psi\cos^2\theta$$

where $I_x = I_{Ax} + I_{Bx} + I_{Cx}$, $I_y = I_{Ay} + I_{By} + I_{Cy}$ and $I_z = I_{Az} + I_{Bz} + I_{Cz}$ are the overall moments of inertia of the instrument package.

The component of interest of the EPV torque is the one that produces a differential motion between the proof masses, i.e., the component about the pivot axis that we call generically as the

v-axis with ν = x, y, or z. The EPV torque is far too small to produce any effects about the other axes. After calling $\boldsymbol{\rho}$ the arm length of the EPV violation acceleration vector with respect to the pivot axis, the *v-axis* component of the EPV torque can be computed as:

$$\tau_v^{EPV} = \left(\rho \times \mathbf{a}_b^{EPV}\right)_v \tag{41}$$

where the EPV acceleration in body axes $\mathbf{a}_b^{EPV}$ is obtained by transforming the inertial-axes acceleration $\mathbf{a}^{EPV}$ as follows:

$$\mathbf{a}_b^{EPV} = [R_{IB}]\mathbf{a}^{EPV}$$

The expression of the sensitive EPV torque component (i.e., about the pivot axis) changes only slightly depending on the selection of the pivot axis-ν alignment with any of the body axes, as follows:

$$\begin{aligned}
\tau_x^{EPV} &= -\rho_z \cos\psi \cos\theta a^{EPV} \\
\tau_y^{EPV} &= -\rho_z \sin\psi \cos\theta a^{EPV} \\
\tau_z^{EPV} &= \rho_y \sin\psi \cos\theta a^{EPV}
\end{aligned} \tag{42}$$

In Eqs. (42), the spin angle (about the z-axis) $\psi = \omega t$ (where ω is the spin rate), θ is the elevation angle, and φ the azimuth angle. The key observation here is that the EP violation torque is always modulated at the frequency ω, irrespective of the orientation of the pivot axis along any one of the body axes.

On the contrary, the body-axes components of the gravity gradient torque (of Eqs. 40) have different frequency content. Specifically, the components about the x and y axes are modulated at ω while the component along the z-axis (i.e., the spin axis) is modulated at 2ω. This consideration has very important consequences for acceleration detectors that utilize rotational configurations. The issue here is the gravity gradient torque acting on the instrument package (see Eqs. 40) because the instrument package needs to have for dynamic reasons a longitudinal moment of inertia different from the transverse moment of inertia and, consequently, this gravity gradient torque is significant. Gravity gradient torques acting on the proof masses are much smaller than on the instrument package because the inertia ellipsoids of the proof masses are as spherical as possible (within the construction tolerances).

Detector configuration with pivot axes parallel to spin axis

In order to separate the effect of the gravity gradient torque acting on the instrument package from an EP violation signal, it is convenient to align the pivot axes of the proof masses with the symmetry axis z of the instrument package, as shown in Fig. 9.

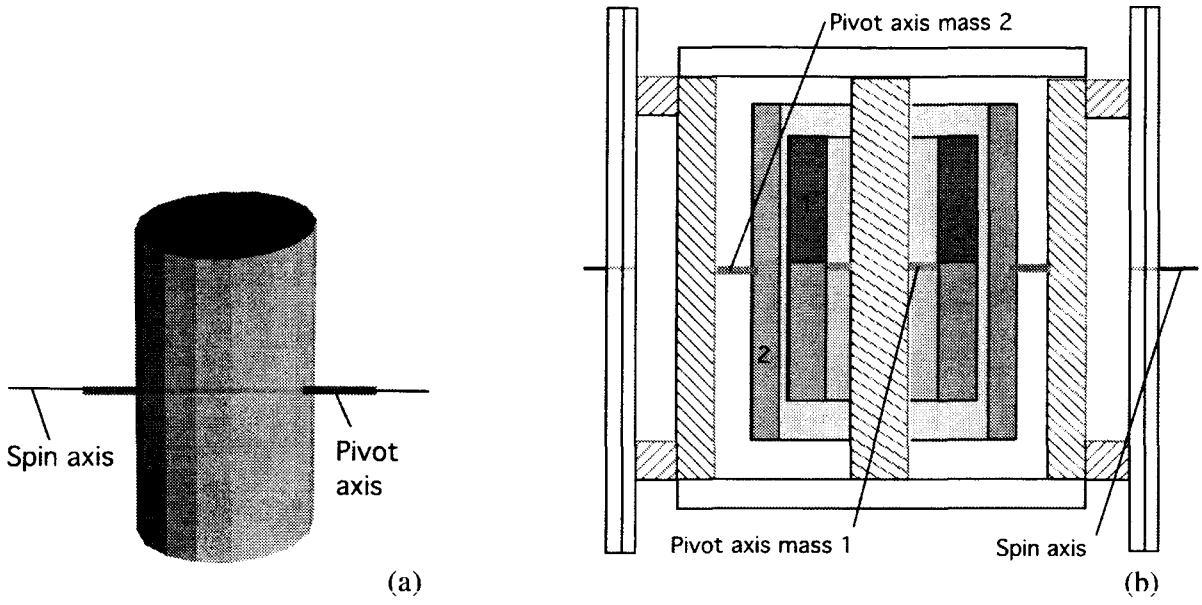

Figure 9 Schematic of purely-rotational detector configuration with pivot axes of proof masses parallel to the detector's spin axis: (a) 3-D sketch of proof mass; and (b) geometrical arrangement of proof masses inside the detector.

The equations of motion of the proof masses for this configuration can be derived from Eqs. (38) and (39) through simple axes transformations to obtain:

$$\begin{aligned}&\ddot{\theta}_A + E_2\dot{\theta}_A + E_3\theta_{\mathbf{A}} + \dot{\omega}_z \\ &+E_4\left(\dot{\omega}_x + \omega_y\omega_z - g_{yz}\right) + E_6\left(\dot{\omega}_y + \omega_x\omega_z + g_{xz}\right) \\ &+E_7\left(\omega_x^2 - \omega_y^2 - g_{xx} + g_{yy}\right) + E_9\left(\omega_x\omega_y - g_{xy}\right) = E_{10}\tau_{Az}^{EPV} + E_{10}\tau_{Az}^{GG}\end{aligned} \tag{43}$$

with

$$E_2 = \boldsymbol{\xi}_A/\tilde{I}_{Az}$$

$$E_3 = \frac{m_A}{\tilde{I}_{Az}}\left(\frac{K_{\boldsymbol{\theta}Az}}{m_A} - \boldsymbol{\delta}_{Ay}^2\boldsymbol{\omega}_y^2 - 2\boldsymbol{\omega}_x\boldsymbol{\omega}_y\boldsymbol{\delta}_{Ax}\boldsymbol{\delta}_{Ay}\right)$$

$$E_4 = -\frac{m_A}{\tilde{I}_{Az}}\delta_{Ax}\delta_{Az}$$

$$E_6 = -\frac{m_A}{\tilde{I}_{Az}}\boldsymbol{\delta}_{Ay}\boldsymbol{\delta}_{Az} \tag{44}$$

$$E_7 = \frac{m_A}{\tilde{I}_{Az}} \delta_{Ax} \delta_{Ay}$$

$$E_9 = \frac{m_A}{\tilde{I}_{Az}} \left(\delta_{Ay}^2 - \delta_{Ax}^2 \right)$$

$$E_{10} = \frac{m_A}{\tilde{I}_{Az}}$$

with $\tilde{I}_{Az} = I_{Az} + m_A \delta_{Axy}^2$ and $\delta_{Axy} = \sqrt{\delta_{Ax}{}^2 + \delta_{Ay}{}^2}$.

Note that for the purely rotational configuration the EPV torque per unit mass is as follows:

$$\tau_{Az}^{EPV} = \rho_x \, a^{EPV} \cos(\omega t) \cos(\theta) \tag{45}$$

where ρ_x, the arm length, is of order a few centimeters because half of one proof mass is made of a material different from the other half. The size of the arm length has very positive consequences regarding the effects of the Earth's gravity gradient and ultimately the tolerance to attitude errors of the spin axis.

An inspection of Eqs. (43) and (44) shows that the gravity gradient "force-related" torques per unit mass (i.e., excluding the "moment-related" gravity gradient torque τ_{Az}^{GG}) are all equal to:

$$\left| \tau_{Az}^{g_{hk}} \right| = \delta_{Ai} \delta_{Aj} g_{hk} \qquad \text{with} \quad i,j,h,k = x,y,z. \tag{46}$$

The "force-related" gravity gradient terms of greatest concern are the off-diagonal ones (with $h \neq k$) that are modulated at the spin frequency ω. The most important among those are the g_{yz} and g_{xz} terms that have the form:

$$g_{zx} = g_{xz} = 3 \frac{GM_E}{R^3} \sin(\omega t) \cos(\theta) \sin(\theta)$$

$$g_{zy} = g_{yz} = 3 \frac{GM_E}{R^3} \cos(\omega t) \cos(\theta) \sin(\theta)$$

These terms, which are directly proportional (for small angles) to the elevation angle θ (while the g_{xy} term is not), drive the requirement on the tolerable attitude error of the spin axis with respect to the horizontal plane. We then compare the maximum value of the EPV torque of Eq. (45) to that of the gravity gradient torque of Eq. (46) for typical values of the differential acceleration detector as follows: $a^{EPV} = 5 \times 10^{-14}$ m/s^2, $\rho_x \approx 3$ cm, R = 6418 km. Finally, we obtain that for very conservative values of differential errors (i.e., between the two proof masses) δ_x, δ_y and $\delta_z < 50$ microns and an attitude error of the spin axis < 7 deg, the (ω-modulated) gravity gradient torques are smaller than the EPV torque at the threshold sensitivity of the detector. In other words, *this design of the differential acceleration detector has cured the problem of the*

tight requirement on the orientation of the spin axis during free fall and also the centering errors between the proof masses CMs. As a result, the requirement on the horizontality of the spin axis at release can be relaxed, thus simplifying the design of the leveling mechanism and the spin/release mechanism.

The orientation of the pivot axis along the symmetry axis z also cures the problems generated by the "moment-related" gravity gradient torques τ^g_{Az} *and* τ^g_{Bz} *acting on the proof masses because the z-axis components are now modulated at* 2ω [see the third of Eqs. (40)] and, consequently, their frequency is well separated from the EPV signal. This is also good news because a very strict equality between the moments of inertia of the two proof masses is no longer required. However, the ellipsoid of inertia of each proof mass needs to be spherical with $\delta L/L < 10^{-4}$ (in which L is a linear dimension of the proof mass) in order to make negligible the higher-order mass moments which are coupled to nearby masses as explained in Ref. i. This issue is common to all configurations of the detector.

In other words, the purely rotational configuration with pivot axes aligned along the spin axis of the detector has mitigated, thanks to frequency separation, the issues associated with gravity gradient torques acting on both the proof masses and the instrument package. Moreover, the combination of the torsional degrees of freedom and the design of the "EPV-sensitive" proof mass made of two different materials has maximized the effect of an EP violation signal, that now overpowers the effects of the gravity gradient forces.

Numerical cases

We ran several simulations of the two configurations of the purely rotational detector: (a) with the pivot axis orthogonal to the spin axis; and (b) the pivot axis parallel to the spin axis. Note that in all those simulations the proof masses are initialized with very large oscillation amplitudes (up to their full range), which we expect to occur after detector's release. Those oscillations are abated during the first few seconds by the feedback loops (see Ref. i), the dynamics effects of which are incorporated into the simulations. At the 5-s mark, the feedback loops are turned off and the detector enter its high-Q (i.e., negligible damping) mode.

The detector is also released with transverse (orthogonal to the spin axis) rotational velocity errors of 0.1 deg/s that is the maximum error expected from the spin/release mechanism. An inclination error of the spin axis at release is also considered, ranging from 0.1 deg for the earlier simulations to 1 deg for other simulations.

Pivot axis perpendicular to spin axis

First, we adopt a precession frequency for the instrument package of 0.3 Hz which is in the previously-defined desirable frequency window. Besides the typical errors at release, we also assume an error between the elastic oscillation frequencies of the proof masses $\delta\omega/\omega = 10^{-5}$, which is consistent with a common-mode rejection factor (CMRF) better than 10^{-4}. The CMRF

depends on the equality of the elastic frequencies of the proof masses. These two frequencies can be independently calibrated by adjusting the feedback loops of the proof masses.

Figure 10 shows the results of a simulation without any EP violation signal. Note that there are no significant components appearing at the signal frequency of 0.5 Hz (i.e., at the spin frequency) and that there is also no significant harmonic component at twice the precession frequency. Figure 11 shows simulation results of a similar case in which we have added an EP violation signal of $1x10^{-14}$ g. The original signal can be recovered with enough precision by means of frequency analysis.

We need to remind that for proof masses with centering errors, the precession dynamics of the package generates differential acceleration harmonics at the spin frequency and twice the spin frequency (see Ref. i). A notable advantage of the purely rotational configuration is that the amplitudes of both harmonics are attenuated and the harmonic at twice the spin frequency becomes negligible with respect to other noise sources. Consequently, we are freer than in the other configurations in choosing the value of precession frequency because the harmonics higher than the precession frequency will not significantly affect the signal frequency. The final result is that it is convenient to lower the package's precession frequency in order to reduce the amplitude of the precession-dynamics-associated noise. Since we would like to resolve the precession dynamics out of the output data through frequency analysis, it makes sense to choose a precession frequency such that at least a couple of full precession cycles occur during free fall. In conclusion, a precession frequency of 0.1 Hz appears an optimal value for a free fall duration of about 25 s.

Figure 12 illustrates the point that, if the moments of inertia of the two proof masses are perfectly identical, then the noise level at the signal frequency is low. An EPV violation signal (here assumed equal to $1x10^{-14}$ g) would be clearly detectable above noise as shown in Fig. 12. However, if we now assume a fractional error of $2x10^{-3}$ (i.e., an absolute error of 10^{-5} kg-m^2) between the moments of inertia of the proof masses, the gravity gradient torque associated with that error, which appears at the same frequency of the signal, overpowers the signal as shown in Fig. 13.

In other words, the purely rotational configuration with the pivot axis perpendicular to the spin axis has mitigated the impact of the precession dynamics on the accelerometer output but has not improved the issue of "moment-related" gravity gradient torques acting on the proof masses themselves and the effect of an inequality in moments of inertia on the differential acceleration.

TORSION DETECTOR; Elastic freq. = 3 Hz; Ix = 0.3; Iy = 0.3003, Iz = 0.12 (0.3 Hz prograde)
OmegaX = 0.1 deg/s, Elevation angle = 0.1 deg; Spin = 0.5 Hz; Ix ≠ Iy; OM_err = 10^-5
del-xA = del-yA = del-zA = 10μm; del-xB = del-yB = del-zB = 12μm; Damp = 37%
Signal = 0 g; Noise = 0 g; Initial xA = xB = ±50 μm; Equations (12/05/04)

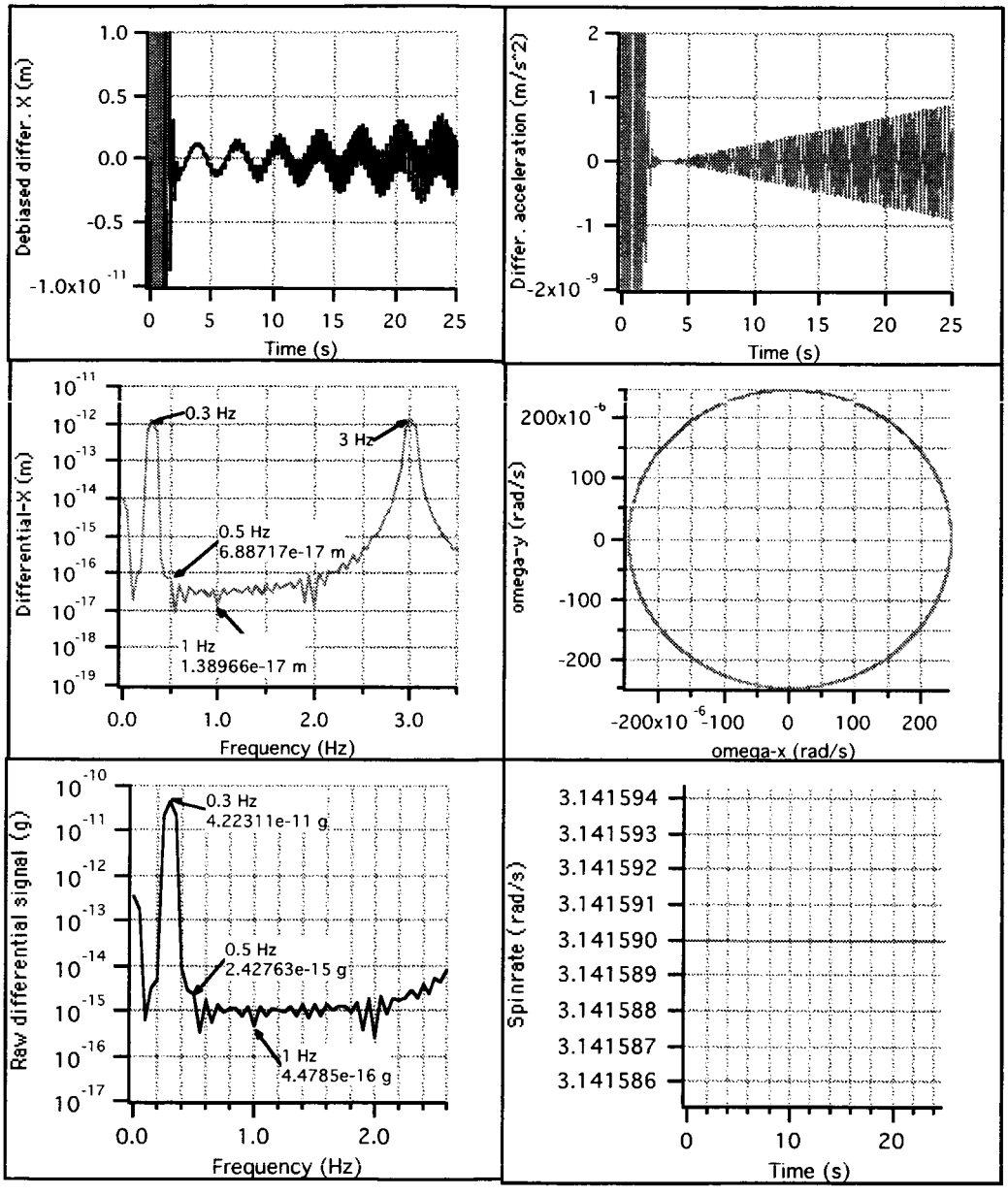

Figure 10 Simulation results for the rotational configuration *with pivot axes orthogonal to the spin axis*, instrument package precession frequency = 0.3 Hz, a difference between oscillation frequencies of the proof masses $\delta\omega/\omega = 10^{-5}$, and no EP violation signal.

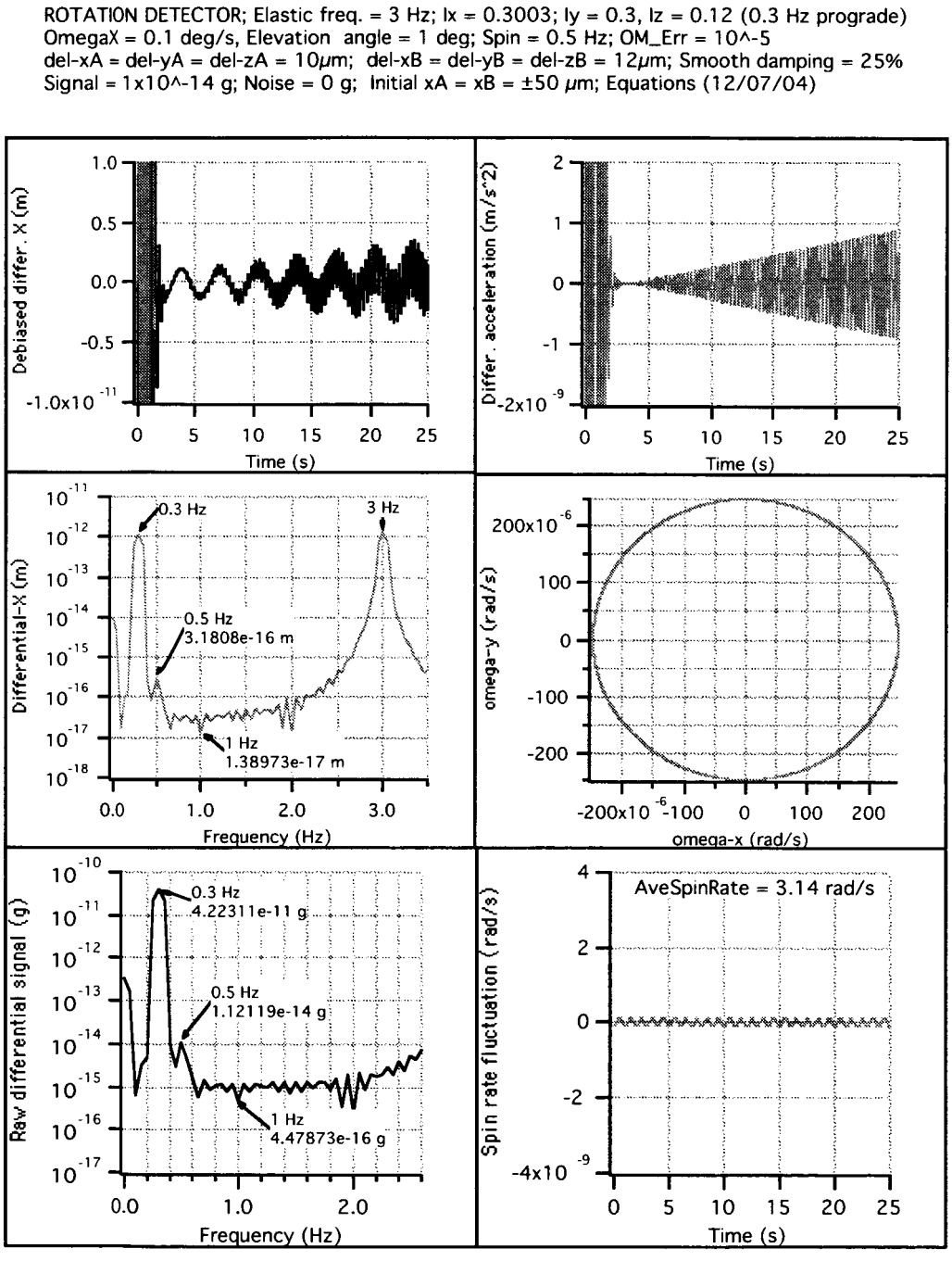

Figure 11 Simulation results for the rotational configuration *with pivot axes orthogonal to the spin axis*, instrument package precession frequency = 0.3 Hz, a difference between oscillation frequencies of the proof masses $\delta\omega/\omega = 10^{-5}$, and an EP violation signal = 1×10^{-14} g.

TORSION DETECTOR; Elastic freq. = 3 Hz; Ix = 0.3; Iy = 0.3003, Iz = 0.24 (0.1 Hz prograde)
OmegaX = 0.1 deg/s, Elevation angle = 0.1 deg; Spin = 0.5 Hz; Ix ≠ Iy; IAy = IBy
del-xA = del-yA = del-zA = 10μm; del-xB = del-yB = del-zB = 12μm; 5-s, Damp = 37%
Signal = 0 g; Noise = 0 g; Initial xA = xB = ±60 μm; Equations (12/05/04)

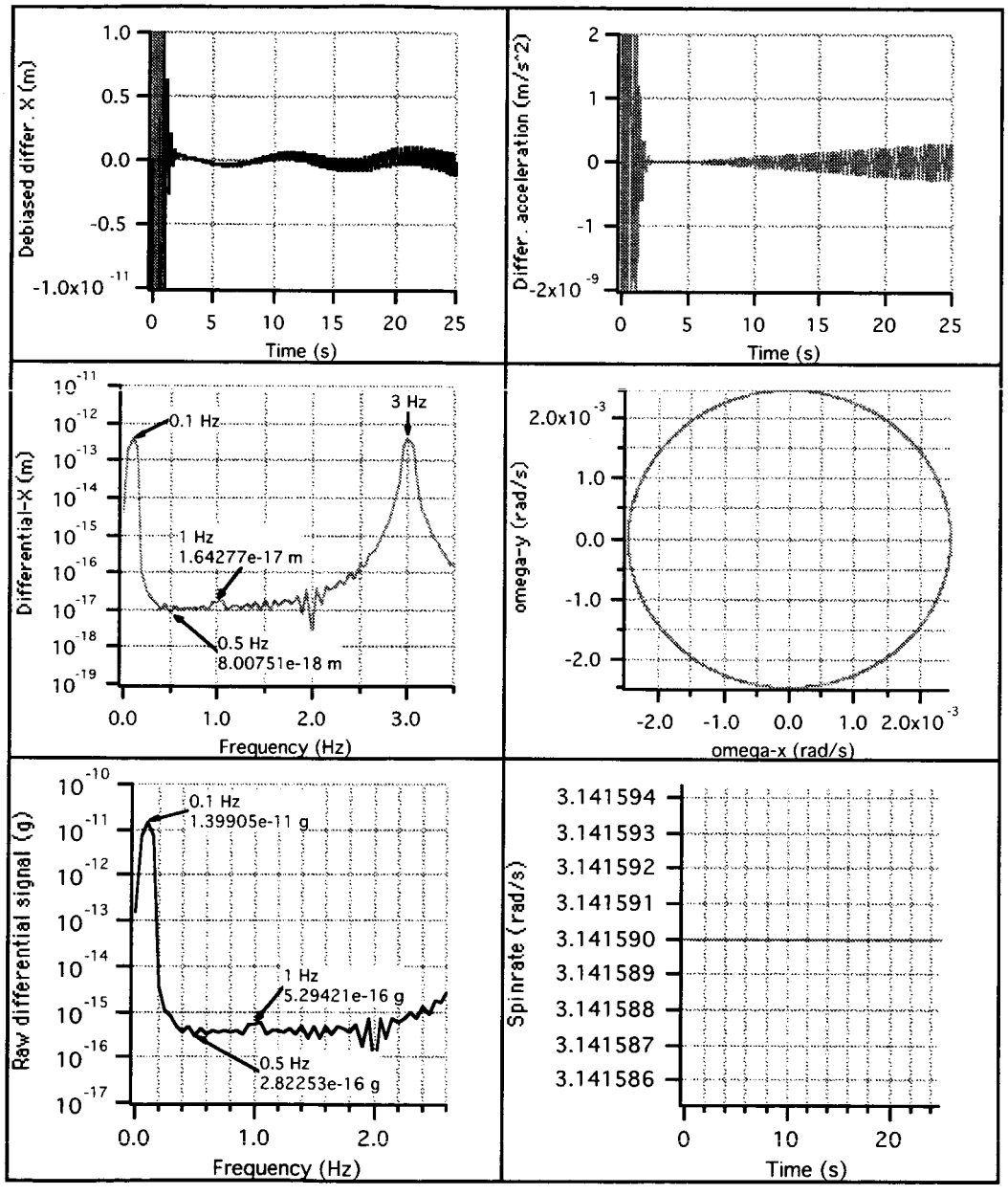

Figure 12 Simulation results for the rotational configuration *with pivot axes orthogonal to the spin axis*, instrument package's precession frequency = 0.1 Hz, perfectly spherical ellipsoids of inertia of the proof masses, and no EP violation signal.

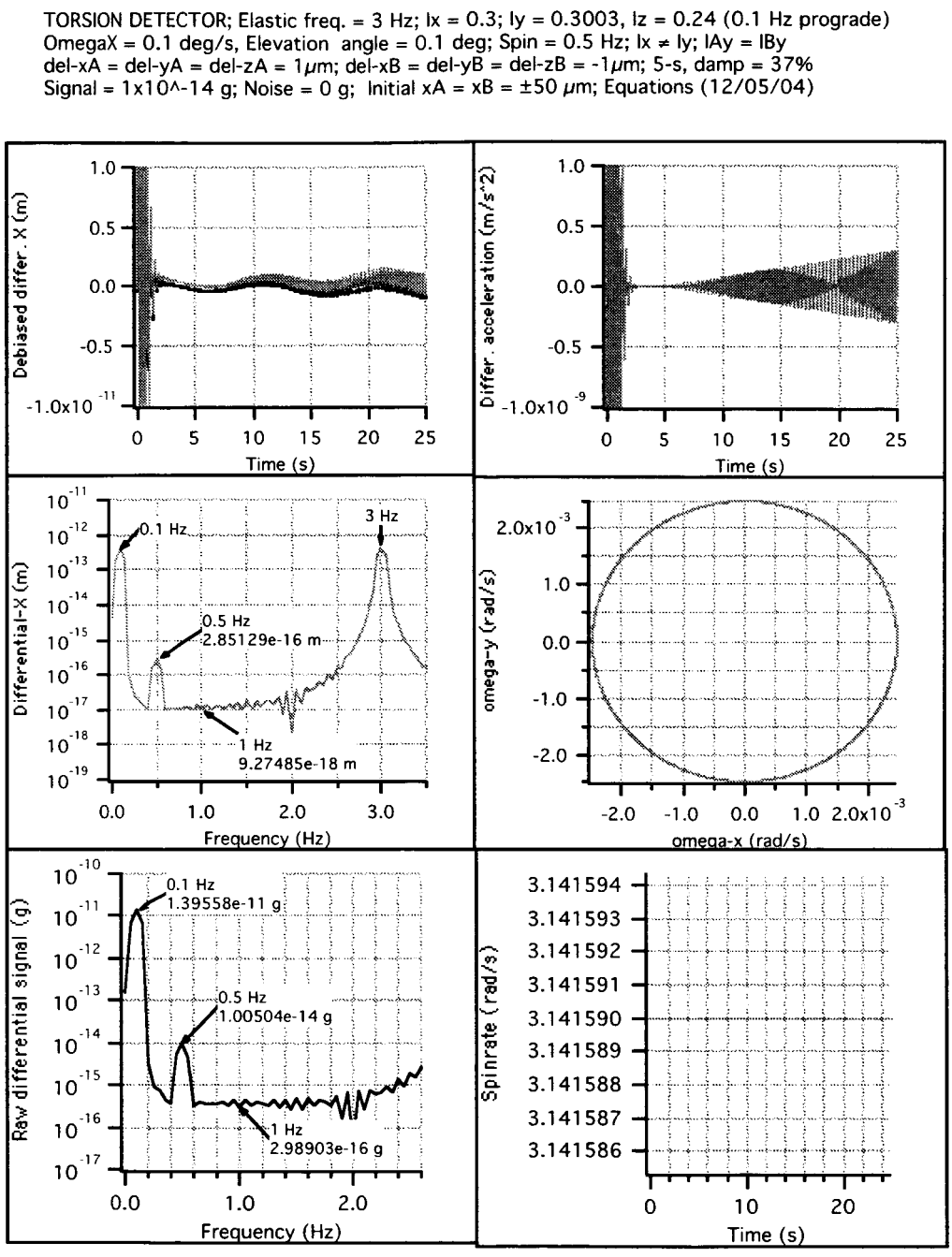

Figure 13 Simulation results for the rotational configuration *with pivot axes orthogonal to the spin axis*, instrument package precession frequency = 0.1 Hz, perfectly spherical ellipsoids of inertia of the proof masses, and an EP violation signal = 1×10^{-14} g, which is accurately recovered by the frequency analysis.

TORSION DETECTOR; Elastic freq. = 3 Hz; Ix = 0.3; Iy = 0.3003, Iz = 0.24 (0.1 Hz prograde)
OmegaX = 0.1 deg/s, Elevation angle = 0.1 deg; Spin = 0.5 Hz; Ix ≠ Iy; OM_FErr = 5x10^-6
del-xA = del-yA = del-zA = 10μm; del-xB = del-yB = del-zB = 12μm; IBy&IBz_FErr= 2x10^-3
Signal = 1x10^-14 g; Noise = 0 g; Initial xA = xB = ±50 μm; Equations (12/05/04)

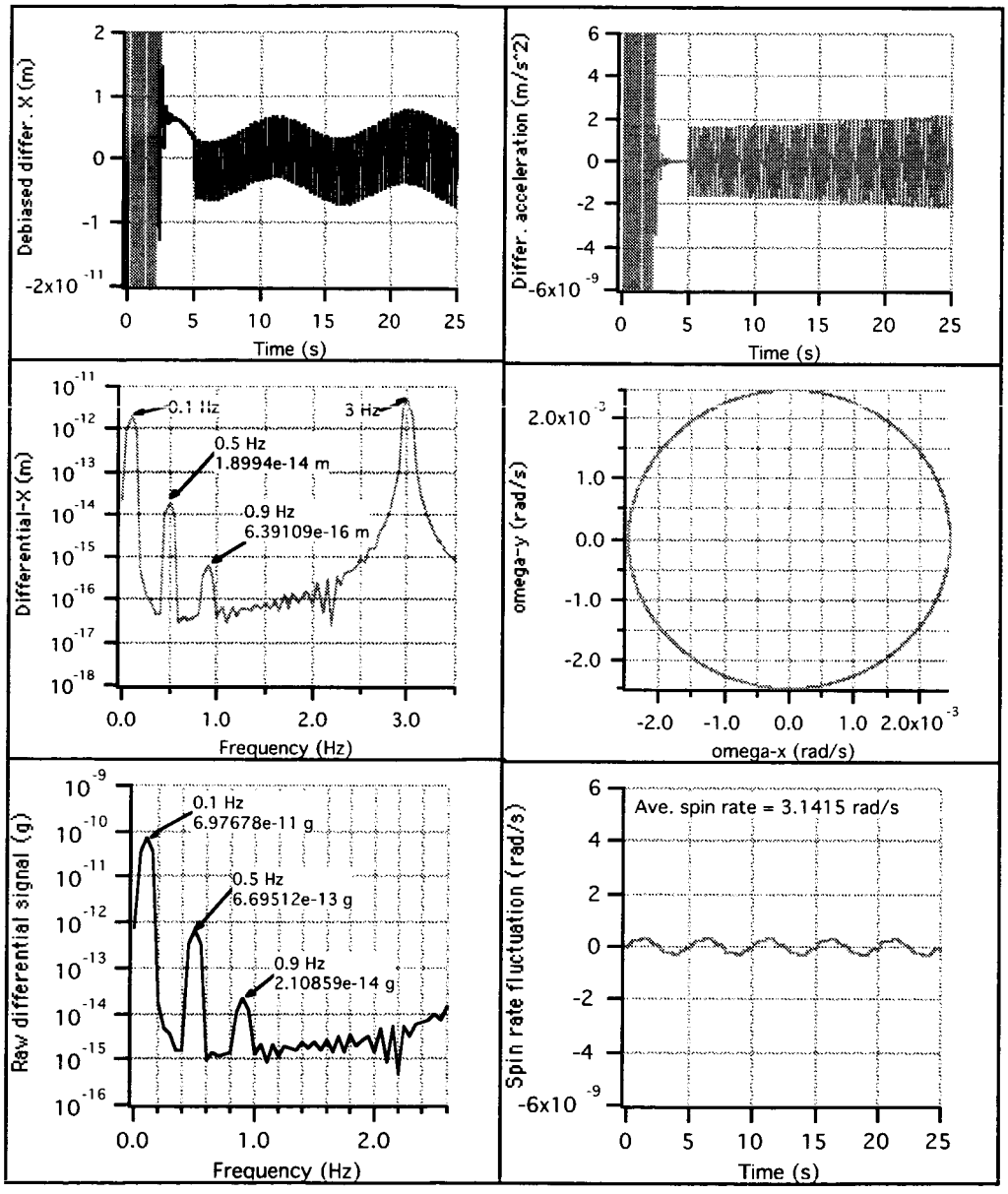

Figure 14 Simulation results for the rotational configuration *with pivot axes orthogonal to the spin axis*, instrument package's precession frequency = 0.1 Hz, EP violation signal = $1x10^{-14}$ g and a fractional error between the moment of inertia of the proof masses of $2x10^{-3}$. Note that the error associated with the moments of inertia has overpowered the EP violation signal.

Pivot axis parallel to spin axis

As mentioned previously, the configuration with the pivot axes of the proof masses parallel to the spin axis of the detector cures the issue of the gravity gradient torques. In this geometrical arrangement, the effects of those torques appear in the accelerometer output at twice the signal frequency and, consequently, do not overlap with the signal.

In the first simulation (shown in Fig. 15), we have assumed the usual velocity error at release of 0.1 deg/s (about an axis perpendicular to the spin axis) and we have increased the error on the elevation angle of the spin axis to 1 deg. The precession frequency of the package is 0.1 Hz. The fractional error between the proof masses elastic frequencies is $\delta\omega/\omega = 5\times10^{-6}$ (which provides a common-mode rejection factor CMRF $\approx 10^{-5}$), the fractional error between the proof masses moments of inertia $\delta I/I = 10^{-5}$, and no EP violation signal. The figure clearly shows that the level of dynamics-related noise at the signal frequency of 0.5 Hz is very low.

Figure 16 shows a case with same error parameters as in the previous simulation but with the addition of an EP violation signal = 1×10^{-14} g. In the simulation of Fig. 17, we have increased the fractional error between moments of inertia of the proof masses to a very lax 10^{-3} in order to show that, thanks to frequency separation, the gravity gradient torques (of the second-order) are not an issue with this detector's configuration. Actually, the tolerable difference in inertia characteristics between the proof masses will be limited to a stricter value by the higher-order moments coupled to nearby masses. The higher-order mass moments require shape accuracies between the two masses better than $\delta L/L \approx 10^{-4}$ which in turns will imply second-order moments of inertia with differential errors $\delta I/I < 10^{-4}$.

In the simulation run of Fig. 18, we have increased the CM centering errors further and relaxed the difference in natural frequencies between proof masses as follows: δ_A = 25 microns, δ_B = 30 microns $\delta\omega/\omega = 10^{-5}$, $\delta I/I = 10^{-4}$. Moreover, we have reduced the EP violation signal to 2×10^{-15} g. As shown in Fig. 18, the small signal has been successfully resolved from the dynamics-related noise and gravity gradients. In other words, the detector sensitivity is no longer limited by the dynamics-related noise and gravity gradients but rather by the intrinsic noise of the differential accelerometer. The latter noise can be modeled as white Gaussian noise, which was assumed null in these simulations (see later on for the extraction of signal from noise)

TORSION DETECTOR; PIVOT-z; Elastic freq. = 3 Hz; Ix = 0.3; Iy = 0.3003, Iz = 0.24 (0.1Hz prograde)
OmegaX = 0.1 deg/s, Elevation angle = 1 deg; Spin = 0.5 Hz; OM_FErr = 5x10^-6
del-xA = del-yA = del-zA = 10μm; del-xB = del-yB = del-zB = 12μm; IBx_FErr = 10^-5
Signal = 0 g; White Noise = 0 g; Initial xA = xB = ±50 μm; Equations (01/03/05)

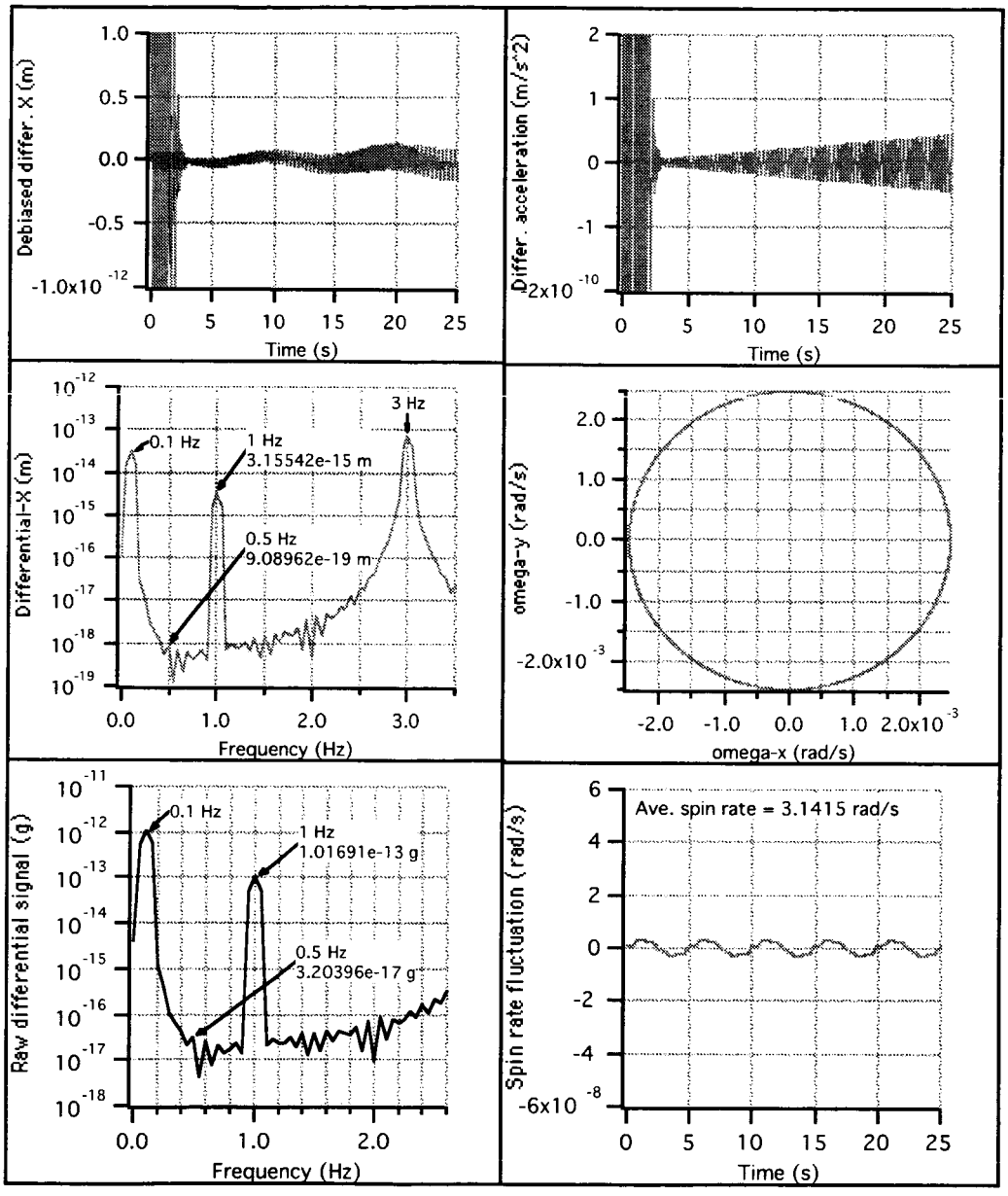

Figure 15 Simulation results for the rotational configuration *with pivot axes parallel to spin axis*, instrument package's precession frequency = 0.1 Hz, proof masses inertia error $\delta I/I = 10^{-5}$, oscillation frequency error $\delta\omega/\omega = 5\text{x}10^{-6}$, and no EP violation signal.

TORSION DETECTOR; PIVOT-z; Elastic freq. = 3 Hz; Ix = 0.3; Iy = 0.3003, Iz = 0.24 (0.1 Hz prograde)
OmegaX = 0.1 deg/s, Elevation angle = 1 deg; Spin = 0.5 Hz; OM_FErr = 5x10^-6
del-xA = del-yA = del-zA = 10μm; del-xB = del-yB = del-zB = 12μm; IBx_FErr = 10^-5
Signal = 1x10^-14 g; White Noise = 0 g; Initial xA = xB = ±50 μm; Equations (01/03/05)

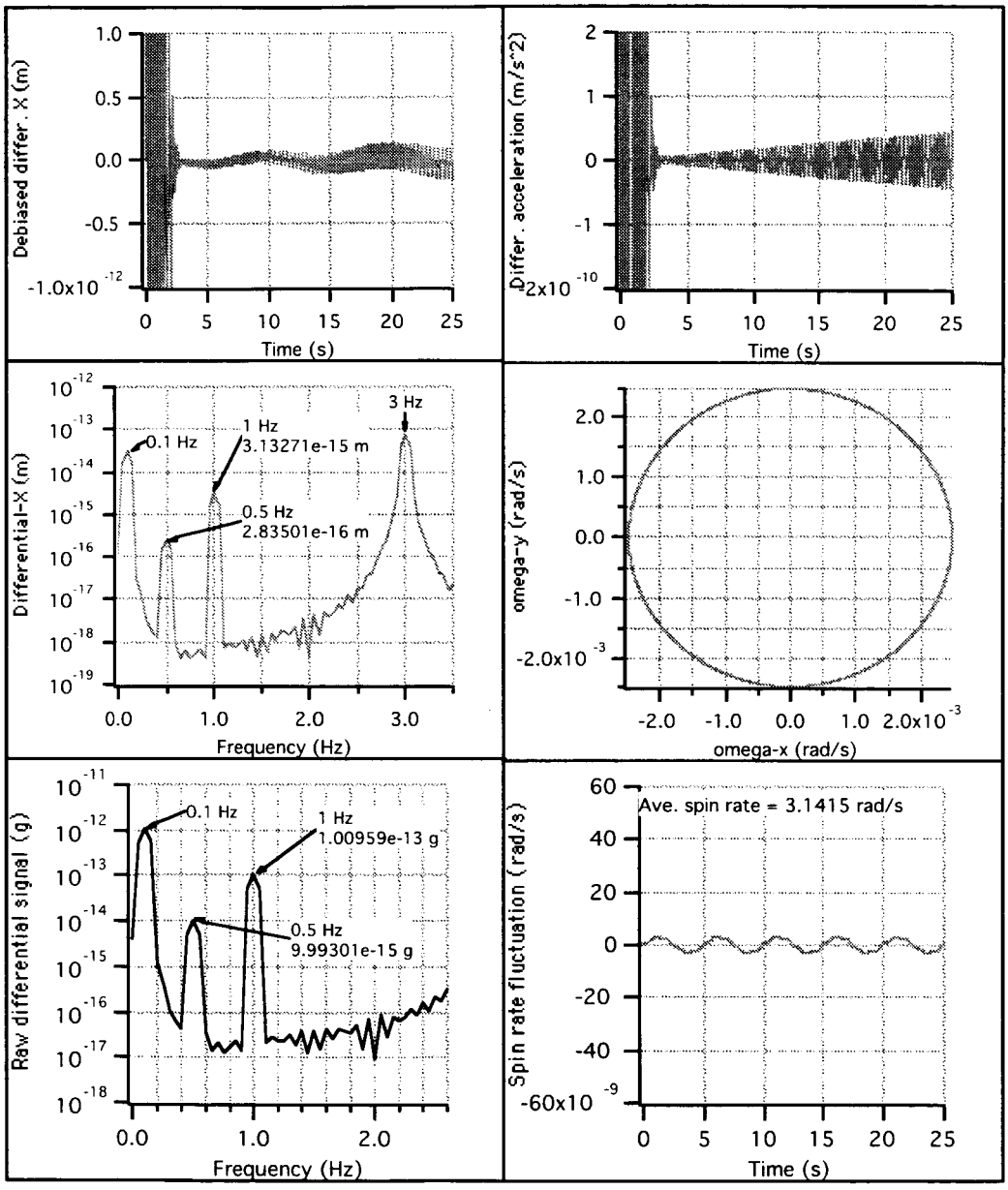

Figure 16 Simulation results for the rotational configuration *with pivot axes parallel to spin axis*, same errors as in Fig. 15, and an EP violation signal = $1x10^{-14}$ g.

TORSION DETECTOR; PIVOT-z; Elastic freq. = 3 Hz; Ix = 0.3; Iy = 0.3003, Iz = 0.24 (0.1 Hz prograde)
OmegaX = 0.1 deg/s, Elevation angle = 1 deg; Spin = 0.5 Hz; OM_FErr = 5x10^-6
del-xA = del-yA = del-zA = 10μm; del-xB = del-yB = del-zB = 12μm; IBx_FErr = 10^-5
Signal = 1x10^-14 g; White Noise = 0 g; Initial xA = xB = ±50 μm; Equations (01/03/05)

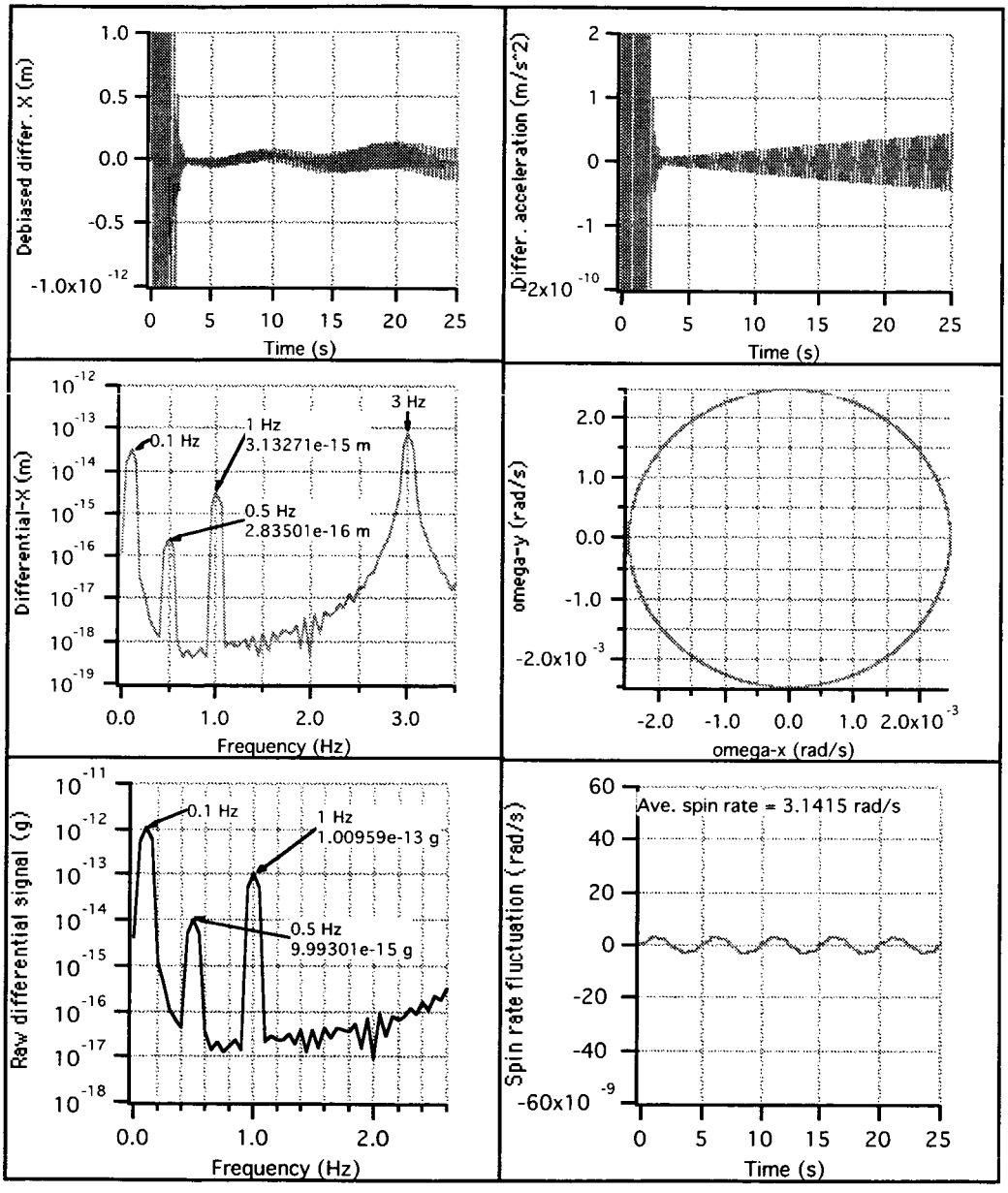

Figure 17 Simulation results for the rotational configuration *with pivot axes parallel to spin axis*, instrument package's precession frequency = 0.1 Hz, proof masses inertia error $\delta I/I = 10^{-5}$, oscillation frequency error $\delta\omega/\omega = 5\text{x}10^{-5}$, EP violation signal = $1\text{x}10^{-14}$ g.

TORSION DETECTOR; PIVOT-z; Elastic freq. = 3 Hz; Ix = 0.3; Iy = 0.3003, Iz = 0.24 (0.1 Hz prograde)
OmegaX = 0.1 deg/s, Elevation angle = 1 deg; Spin = 0.5 Hz; OM_FErr = 5x10^-6
del-xA = del-yA = del-zA = 10μm; del-xB = del-yB = del-zB = 12μm; IBx_FErr = 10^-3
Signal = 1x10^-14 g; Noise = 0 g; Initial xA = xB = ±50 μm; Equations (01/03/05)

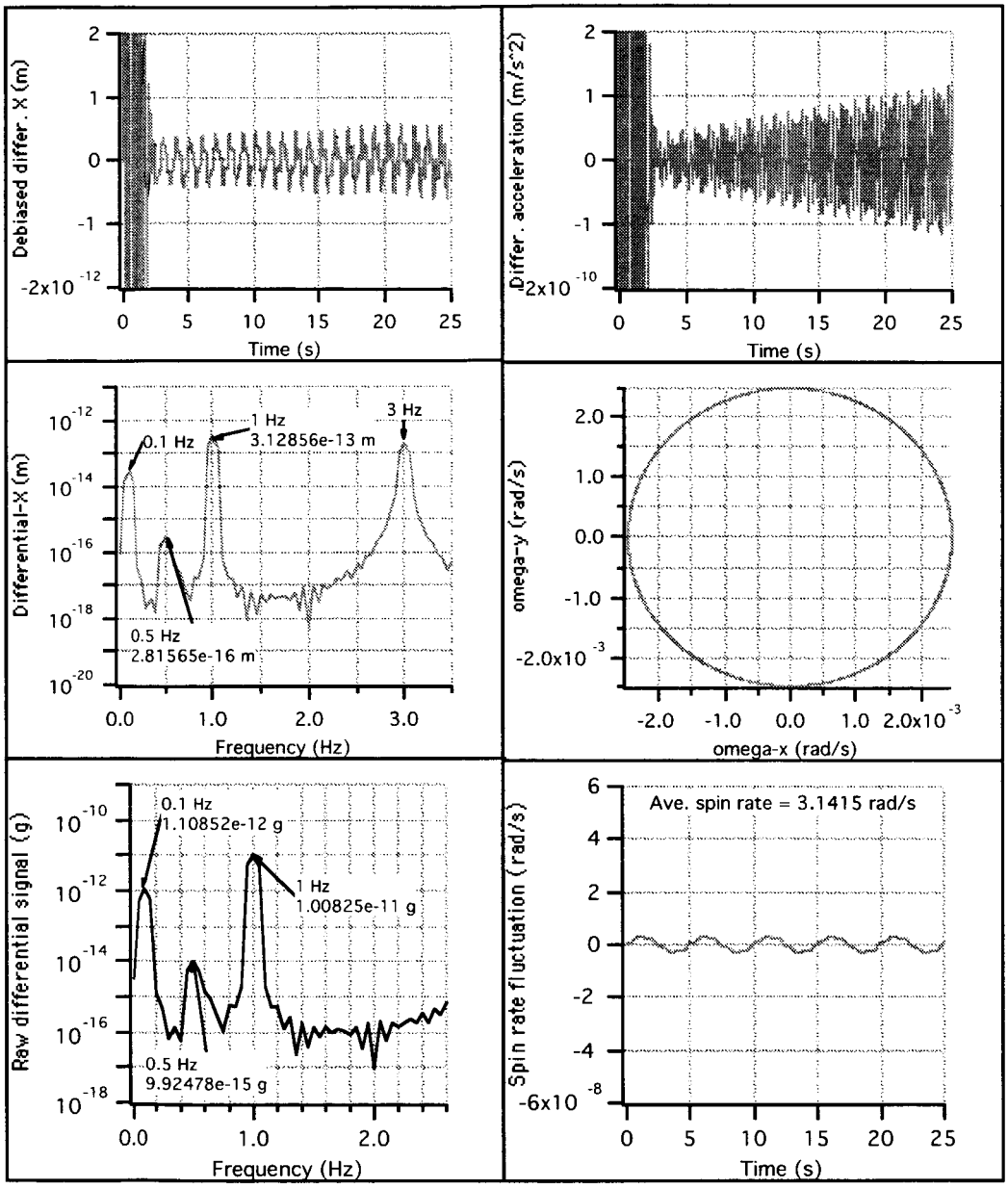

Figure 18 Simulation results for the rotational configuration *with pivot axes parallel to spin axis*, instrument package's precession frequency = 0.1 Hz, proof masses inertia error $\delta I/I = 10^{-3}$, oscillation frequency error $\delta\omega/\omega = 5\text{x}10^{-6}$, EP violation signal = $1\text{x}10^{-14}$ g.

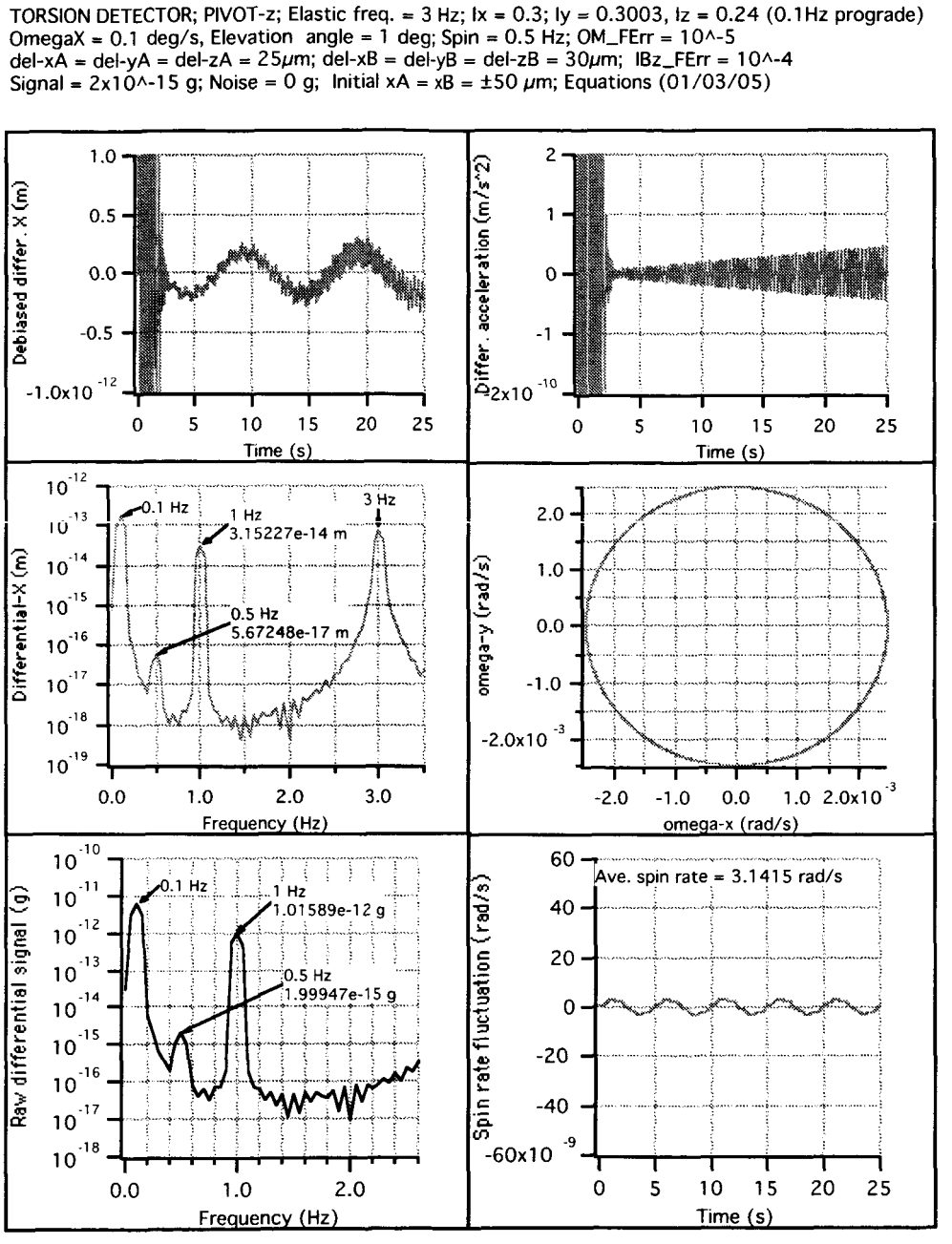

Figure 19 Simulation results for rotational configuration *with pivot axes parallel to spin axis*, instrument package's precession frequency = 0.1 Hz, proof masses inertia error $\delta I/I = 10^{-4}$, oscillation frequency error $\delta\omega/\omega = 10^{-5}$, large centering errors of CMs, spin axis elevation error = 1°, and EP violation signal = $2\text{x}10^{-15}$ g. No white noise was added to the accelerometer output. Note that the small signal is successfully resolved out of the dynamics-related noise.

Detector conceptual design

Proof mass geometry

The analysis conducted thus far has resulted in a conceptual design of the flight-experiment detector that is able to reject almost any reasonable perturbation and, at the same time, magnify the effect of an EP violation signal with respect to perturbations. A large number of numerical simulations carried out for the various configurations have proved that the purely-rotational configuration with pivot axes parallel to the detector's spin axis can effectively separate the dynamics-related effects and gravity gradients from the signal.

An important element of the rotational detector is the design of the proof masses, consisting of: (1) an *EPV-sensitive* mass made of two different materials; and (2) a *dynamics-reference* mass that enables the attenuation of the rigid-body dynamics and its effect on the detector's differential output. In this section we would like to dwell further on the inertia characteristics of the proof masses and options for their mechanical design.

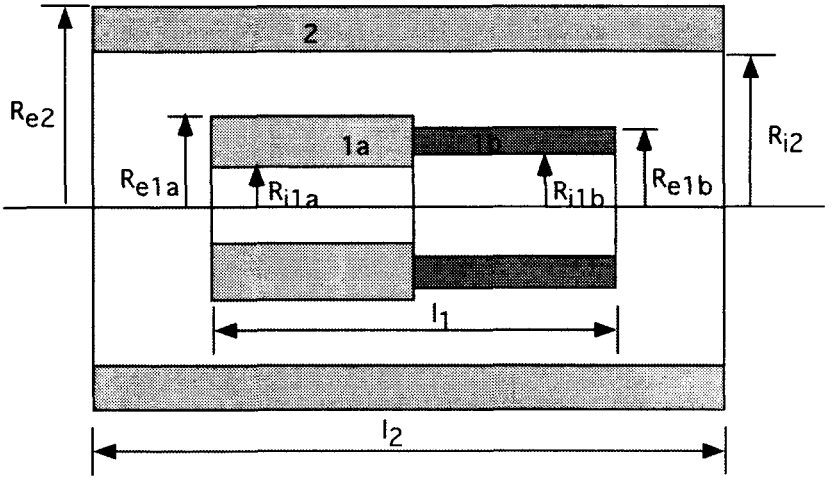

Figure 20 Geometry of proof masses.

Equal masses of the proof masses are not required because, thanks to the EP, the mass does not count in free fall. The equality of the oscillation frequencies of the proof masses is important in a differential detector because we want the two masses move in synchronicity and with equal amplitude under the effect of a common-mode excitation. The frequencies depend on the ratio K/I where K is the rotational elastic stiffness and I the moment of inertia of each mass about the pivot axes. Although in general we could design for equal ratios, here we focus on the case in which the stiffnesses are the same and, consequently, we need to design for $I_A = I_B$. Remember also that each proof mass needs to have a spherical ellipsoid of inertia which drives the design into using cylinders with a specific ratio between radius and length as shown later on.

In the schematic drawing of Fig. 19 we use the subscript 1 for the internal and 2 for the external proof mass; l_1 and l_2 are the cylinders' lengths, R_{e1} and R_{e2} are the external radii and R_{i1} and R_{i2} the internal radii of the proof masses. Moreover, we adopt a body-attached reference frame with z along the longitudinal axis of the proof mass and x and y along the transverse axes. Note that the naming of the axes is conventional and, consequently, the analysis shown here is valid for either a configuration with the pivot axis perpendicular to the spin axis or the pivot axis parallel to the spin axis.

We need to design for proof masses with: (a) spherical inertia ellipsoids (i.e., same moments of inertia about the three axes); (b) same moments of inertia between one another; (c) and coincident centers of mass in the geometrical centers, where the pivots are attached. Let us focus first on the internal proof mass which consists of a cylinder with two halves (named *a* and *b)* made of different materials. We first define the moments of inertia about the three axes as follows:

$$\begin{aligned} I_{1z}^{CM} &= I_{1az}^{*} + I_{1bz}^{*} \\ I_{1x}^{CM} &= I_{1ax}^{*} + I_{1bx}^{*} + \left(m_{1a} + m_{1b}\right)\left(\frac{l_1}{4}\right)^2 \\ I_{1y}^{CM} &= I_{1x}^{CM} \end{aligned} \tag{47}$$

where the asterisk indicates that that moment of inertia is computed with respect to the center of mass of the half portion of the proof mass while the superscript CM stands for the overall center of mass.

The condition of spherical inertia ellipsoid that is, $I_{1x}^{CM} = I_{1z}^{CM} = I_{1y}^{CM}$, can be expressed as:

$$I_{1az}^{*} + I_{1bz}^{*} = I_{1ax}^{*} + I_{1bx}^{*} + \left(m_{1a} + m_{1b}\right)\left(\frac{l_1}{4}\right)^2 \tag{48}$$

in which the cylindrical symmetry makes the second equality redundant. The condition of CM in the middle of the proof mass implies obviously that

$$m_{1a} = m_{1b} = \frac{1}{2} m_1 \tag{49}$$

After expressing the moments of inertia in terms of geometrical parameters, we obtain

$$I_{1az}^{*} = \frac{1}{4} m_1 \left(R_{e1a}^2 + R_{i1a}^2\right) \tag{50.1}$$

$$I_{1bz}^{*} = \frac{1}{4} m_1 \left(R_{e1b}^2 + R_{i1b}^2\right) \tag{50.2}$$

$$I^*_{1ax} = \frac{1}{24} m_1 \left[3R^2_{e1a} + 3R^2_{i1a} + (l_1/2)^2 \right] \tag{50.3}$$

$$I^*_{1bx} = \frac{1}{24} m_1 \left[3R^2_{e1b} + 3R^2_{i1b} + (l_1/2)^2 \right] \tag{50.4}$$

Since we have 5 geometrical variables and one equation, we need to impose more conditions in order to restrict the numbers of possible solutions. If we require that the two halves of the internal proof mass have equal moments of inertia about their own CMs then $I^*_{1az} = I^*_{1bz}$ will yield

$$\left(R^2_{e1a} + R^2_{i1a} \right)/2 = \left(R^2_{e1b} + R^2_{i1b} \right)/2 \tag{51}$$

Equation (51) restricts the possible solutions to only those pairs of radii with equal geometrical means for the two halves of the proof mass.

If we now impose that $I^*_{1ax} = I^*_{1bx}$ then Eqs. (47) and (48) yield:

$$I^{CM}_{1z} = \frac{1}{2} m_1 \left(R^2_{e1} + R^2_{i1} \right) \tag{52.1}$$

$$I^{CM}_{1x} = \frac{1}{12} m_1 \left[3R^2_{e1} + 3R^2_{i1} + l^2_1 \right] \tag{52.2}$$

which, when equated to one another, yields the usual relationship for cylinders with spherical inertia ellipsoids

$$l_1 = \sqrt{3} \sqrt{R^2_{e1a} + R^2_{i1a}} \tag{53}$$

After calling ρ_a and ρ_b the densities of the materials that make up the two halves (in which we have assumed $\rho_a < \rho_b$), we have

$$m_{1a} = \rho_a \pi \left(R^2_{e1a} - R^2_{i1a} \right) \frac{l_1}{2} \tag{54.1}$$

$$m_{1b} = \rho_b \pi \left(R^2_{e1b} - R^2_{i1b} \right) \frac{l_1}{2} \tag{54.2}$$

where $m_1 = m_{1a} + m_{1b}$. Finally, Eqs. (49), (51) and (54) lead to:

$$R^2_{e1a} = \frac{1}{2} \left[R^2_{e1b} (1 + \rho_a/\rho_b) + R^2_{i1b} (1 - \rho_a/\rho_b) \right] \tag{55.1}$$

$$R_{i1a}^2 = \frac{1}{2}\left[R_{e1b}^2\left(1-\rho_a/\rho_b\right)+R_{i1b}^2\left(1+\rho_a/\rho_b\right)\right] \tag{55.2}$$

which relate the radii of one side to the other side of the proof mass.

The relevant equations for the external proof mass (subscript = 2) can be simply summarized as follows:

$$m_2 = \rho_a \pi\left(R_{e2}^2 - R_{i2}^2\right) l_2 \tag{56.1}$$

$$I_{2x}^{CM} = I_{2y}^{CM} = I_{2z}^{CM} = \frac{1}{2} m_2\left(R_{e2}^2 + R_{i2}^2\right) \tag{56.2}$$

$$l_2 = \sqrt{3}\sqrt{R_{e2}^2 + R_{i2}^2} \tag{56.3}$$

where in Eq. (56.1) we have assumed that the density of proof mass 2 is equal to the density of one of the halves of proof mass 1. The previous equations can be used to dimension the two proof masses so that they satisfy the conditions imposed on their inertial characteristics.

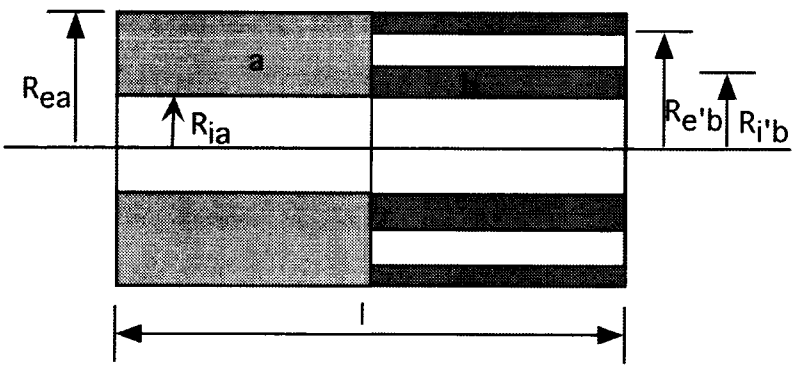

Figure 21 Geometry of internal proof mass with flat inner and outer surfaces.

In a further refinement of the internal proof mass design, we also impose that the inner and outer radii are the same for the two halves. These additional geometrical constraints will simplify the design of the signal pick up plates of the accelerometer because, in this case, the internal proof mass will have flat inner and outer surfaces. However, in order to satisfy these two additional constraints without violating the previous ones, we have to split the right half of the proof mass into two concentric cylinders: the inner one will be mounted flush with the inner radius of the left half and, likewise, the outer one will be mounted flush with the outer radius. In other words, the inner and outer radii of the left half have been replaced by the inner radius of the outer cylinder of the outer radius of the inner cylinder (see Fig. 21). By following the new parameterization, the conditions $I_{1ax}^* = I_{1bx}^*$ and $I_{1az}^* = I_{1bz}^*$, combined with Eqs. (54), yield:

$$R_e^2 = \frac{1}{2}\left[\frac{R_e^4 - R_i^4}{R_e^2 - R_i^2} + (1 - \rho_a/\rho_b)(R_e^2 - R_i^2)\right] \tag{57.1}$$

$$R_i^2 = \frac{1}{2}\left[\frac{R_e^4 - R_i^4}{R_e^2 - R_i^2} - (1 - \rho_a/\rho_b)(R_e^2 - R_i^2)\right] \tag{57.2}$$

in which we have dropped the subscript 1 for the sake of simplicity. Equations (57) replaces Eqs. (55) for the flush-cylinder configuration.

In a modification of the previous design, the internal proof mass would involve the inner cylinder of the right half to consist of two layers: the innermost one (on the side of the pivot attachments) made of the same material of the left half and followed by a thicker cylinder of the higher-density material (see Fig. 22). The outer cylinder will also be made of the higher-density material. The goal obviously is to maximize the amount of mass made of the higher-density material while at the same time provide for ease of manufacturing and construction precision. Having the innermost surface of the internal proof mass made of the same material could help in constructing the pivots of the proof masses which are also made of the same material[ix]. Other geometrical options are also possible. We have not explored them further because at this point of the project we are more interested in developing the conceptual models and analyzing their merits rather than focusing on the detailed engineering of the flight detector. The latter effort will require a thorough design and development work of the flight detector to be led by our partners at the IFSI laboratory.

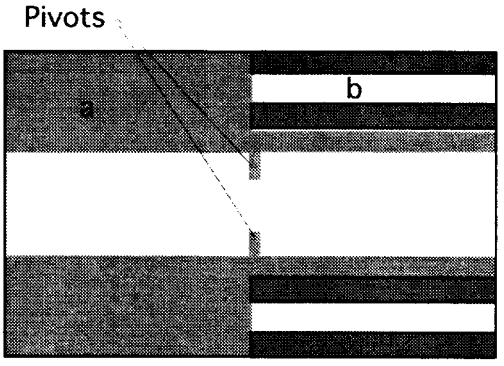

Figure 22 Schematic of internal proof mass with inside surface of cylinder made of one material.

Sample dimensioning of proof masses

We have utilized the previous equations to derive a sample design of the two proof masses tat could be used in a purely rotational configuration of the detector. This is only a sample design of the proof masses that does not intend to freeze the dimensioning of the actual flight detector for the EP experiments. In the example of Figure 23, we have adopted Aluminum as the low-density material and a Copper alloy as the high-density material. Aluminum and Copper are materials that have been widely used for EP testing in the past and they are adopted here for

exemplification only. Other materials pairs, like Beryllium and Platinum-Iridium for example, would lead to a design of the proof masses with different dimensions.

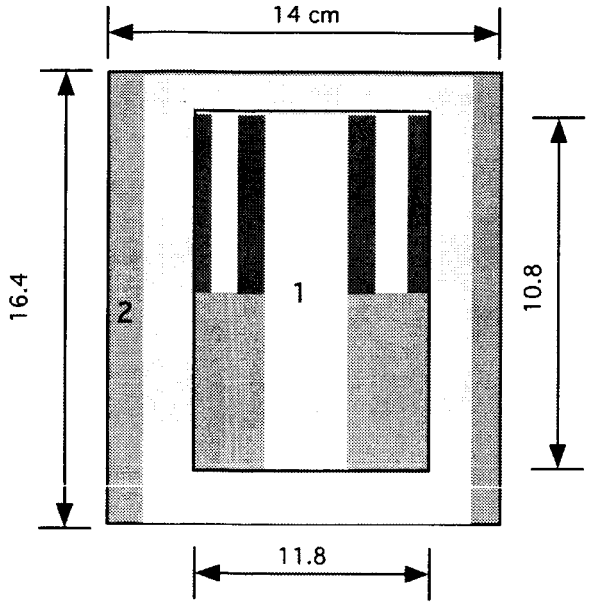

Figure 23 Sample dimensioning of proof masses made of Aluminum and Copper-alloy.

Many choices of materials are possible because the equations derived above have solutions for any ratio of the material densities ρ_a/ρ_b. In the design shown in Fig. 23, the inertia characteristics of the proof masses are as follows:

$m_1 = 2.82$ kg; $I_{x1} = I_{y1} = I_{z1} = 5.47 \times 10^{-3}$ kg-m^2 (1 = internal proof mass)
$m_2 = 1.12$ kg; $I_{x2} = I_{y2} = I_{z2} = 5.47 \times 10^{-3}$ kg-m^2 (2 = external proof mass)

These values have been used in the dynamics simulations shown in the previous section for the rotational configuration of the detector. As stated previously, this dimensioning is one possibility among many options.

Concluding remarks

The analysis of the dynamics in free fall of various detector configurations in the presence of release errors and proof masses imperfections has led to the design of a suitable detector configuration. This configuration provides a very low level of dynamics-related noise at the signal frequency that meets the desired threshold sensitivity goal for the detector. The configuration consists of proof masses that have purely rotational degrees of freedom. The internal proof mass is the "EP-violation-sensitive" mass that, thanks to its design made of two halves of different materials, is able to sense an EP violation force. The second mass, made of one of the materials of the other mass, is the "dynamical-reference" mass. The role of this proof mass is to attenuate (and ideally remove), through output differencing, the dynamics-related

noise from the detector's output. Moreover, with this design an EP violation force will produce a relatively strong torque when compared to other perturbation torques.

We have demonstrated through extensive simulations that this detector design is capable of detecting a very small differential signal and resolving that signal out of the dynamics-related noise and gravity gradients in the presence of conservative values of the construction errors of the proof masses. *This conclusion implies that, with this new design, the dynamics-related noise is no longer the limiting factor of the detector's threshold sensitivity. The limiting factor becomes the intrinsic noise of the detector (e.g., the Brownian noise of the proof masses).*

We have also derived the geometrical relationships between the internal and external proof masses that provide the desired inertia ellipsoids for each mass and the equality between the moments of inertia of the two proof masses. Moreover, we have worked out design options for the internal proof mass (the one made of two different materials) and the geometries that satisfy the inertia and mass requirements for that proof mass.

Detection and Estimation of the EP Violation Signal

Characteristics of the data

The sampled data consists of a colored noise, a white Gaussian noise (WGN) and a possible EP violation signal. The colored noise is produced by the precession dynamics (at a known frequency) and by elastic modes of vibration. The Signal to Noise Ratio due to the colored noise is very small and could be as much as –80dB. The white noise represents a thermal noise and may be at the same order of magnitude as the violation signal. The violation signal is at a known frequency (0.5 Hz) and phase. In this report we will call the EP violation signal *the signal.* Accordingly, there are two major difficulties in extracting the signal. The first problem is the low SNR and the possible masking of the signal by colored noise components (e.g., the harmonics associated with the precession dynamics). The second problem is the extraction of the signal from the white noise. Since the harmonic related to the signal frequency may be affected by the white noise, we need to estimate the confidence of detection as well. For that purpose we will assume that there is no component of colored noise at the signal frequency.

The data record length is $T = 20$ seconds and the sampling rate is typically $f_s = 100$ Hz. Therefore the data consists of 2000 samples. Accordingly, the spectral resolution is $\Delta f = 1/T = 0.05$ Hz. The bin width on the other hand is $\Delta f_{bin} = f_s / N_{DFT}$ where N_{DFT} is the number of points in the DFT. The maximum number of point effectively used for an FFT (out of a sample of 2000) is 1024 that gives a bin width of about 0.097 Hz. Therefore we prefer a DFT algorithms of 2000 points, with a bin width of 0.05 Hz, rather than an FFT algorithms. In addition to sufficient resolution we require a bin at 0.5 Hz (the assumed signal frequency, f_0). The condition for that is the existence of an integer K such that $K = N f_0 / f_s$. Therefore $N = 200K$ for the current data. The conclusion from this discussion is that an acceptable N_{DFT} for bin widths less than 0.1 Hz are 1000, 1200, 1400, 1600, 1800 and 2000 for a bin width of 0.05 Hz.

As a test-bed we used four sets of sampled data associated with different cases and/or detector configurations. The data include a colored noise and an assumed signal of 2.8×10^{-16} m (equivalent to a differential acceleration of 1×10^{-14} g). The sampled data and their DFTs are shown in Figs. 24 and 25. It is obvious that the DFT alone is not sufficient to resolve the signal.

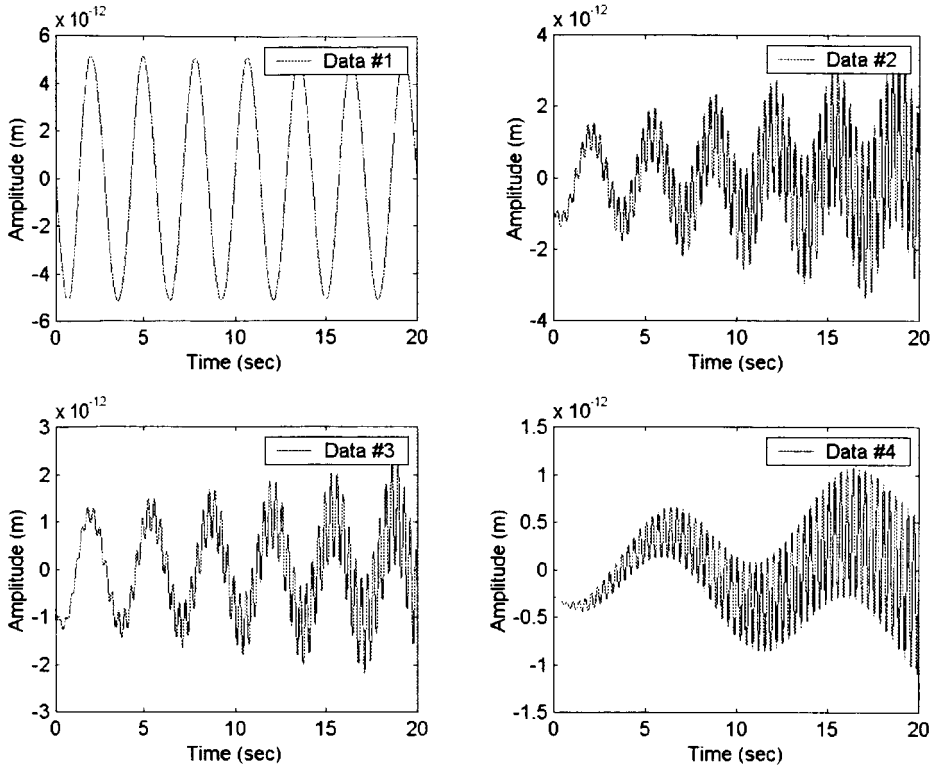

Figure 24 Sampled data (signal + colored noise).

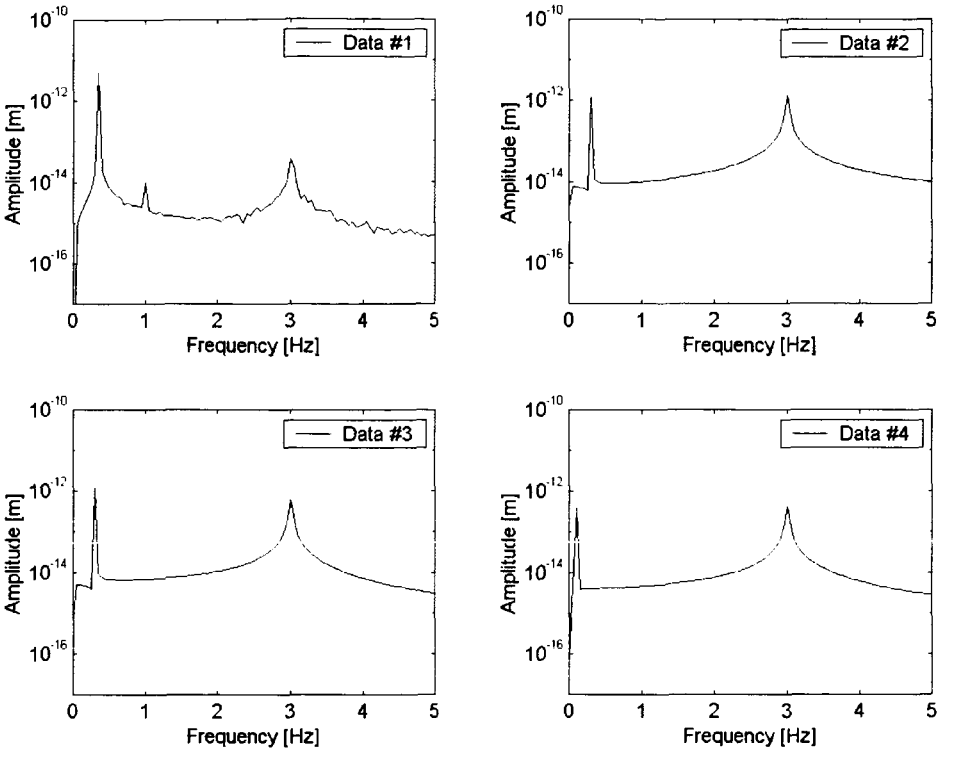

Figure 25 DFT of sampled data without pre-processing.

Our goal was to search and test feasible methods for detecting and estimating the signal. In this report we deal separately with the colored noise and with the white noise. We first present few methods to pre-process the data in order to improve the signal detection. We then test few filtering techniques to estimate the signal with the pre-processed colored noise. Lastly, we assume a pure white noise and we estimate and detect the signal by using an optimal statistical filter.

Data pre-processing

Windowing

In order to enhance the observability (frequency detection) of the DFT data we need to pre-process the data through a window. We tested three window algorithms:

Hamming: $W(n) = 0.54 - 0.46\cos(2\pi n/N)$

Hanning: $W(n) = 0.5[1 - \cos(2\pi n/N)]$

Blackman: $W(n) = 0.42 - 0.5\cos(2\pi n/N) + 0.08\cos(4\pi n/N)$

Hamming window performed poorly while Blackman window was the best. Figure 26 shows the DFT of the previous sampled data after windowing by Blackman window. Each test in this report was pre-filtered by Blackman window. Note that the signal is observable only in data set #4, where the precession frequency is the smallest. Note also that the windowing attenuates the physical resolution by a factor of two. Therefore, although the bin length is still 0.05 Hz, the physical resolution is now 0.1 Hz.

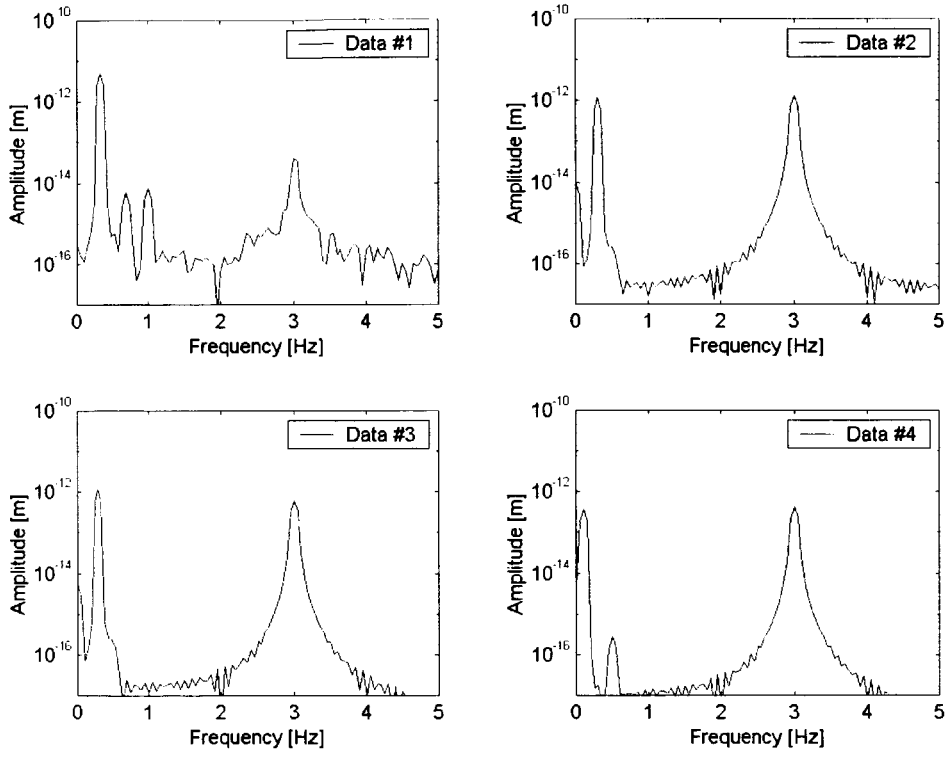

Figure 26 DFT of sampled data after windowing.

Segmentation

A hypothetical way to improve the signal detection is to segment the signal with time record commensurate with the signal period and to aggregate the segmentations. This technique should work well when the white noise is ideal and there is a sufficient number of segmentation such that at each time step the white noise will average out. A segmented record should be of an even number (since the signal period is 2 sec), but because of our 20-sec total time record, only segment records of 2, 5 and 10 seconds are acceptable. Therefore the number of segmentations can be only 2, 5 or 10.

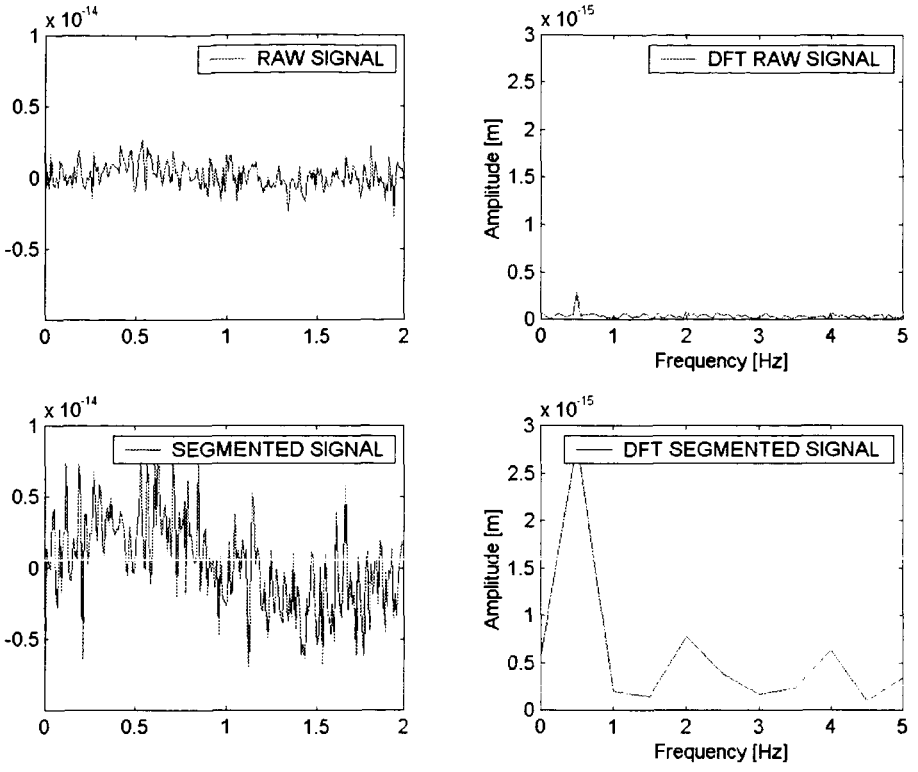

Figure 27 Aggregated 10 segmentations for the signal in a white noise.

Figure 27 shows the segmentation results in the time and in the frequency domains for 10 segmentations. Since the noise is not pure white and the time record is too short, in addition to the signal that adds up, some components of the "white" noise also adds up. Only Monte Carlo simulations gave the desired benefit: signal adds up while the uncorrected noise cancelled. Another problem is that the resolution deteriorates with increasing number of segments. Since we have only few bins separating the signal from the colored noise, reducing the resolution adds the noise (colored or white) to the bin related to the signal. Given our current time record and sampling rate, it is not recommended to have more than two segments (and probably not to use it for a single experiment). In addition, some colored noise may also add up. But only certain frequencies, greater than 0.5 Hz and commensurate with the segmentation would add up. Thus, integer frequencies from 1 Hz to the Nyquist frequency may add up.

Amplitude cuts in the frequency domain

Another possible method is to apply a DFT to the windowed data and then cut or eliminate the dominant colored noise in the frequency domain. The advantage of this method is that it preserves the signal while reducing the colored noise as needed. Figure 28 shows the data with threshold cuts where a white noise was added. The domain of the cuts depends on the particular

data. Utilizing a threshold with a magnitude as high as the expected signal can improve the numerical convergence of dynamical filters and improve the precision of least square algorithms. However, we need to be careful when a white noise is present. The threshold cuts conserves the white noise as long as the threshold is above the white noise. But a complete cut eliminates certain frequency domain from the while noise, thus destroys the purity of whiteness.

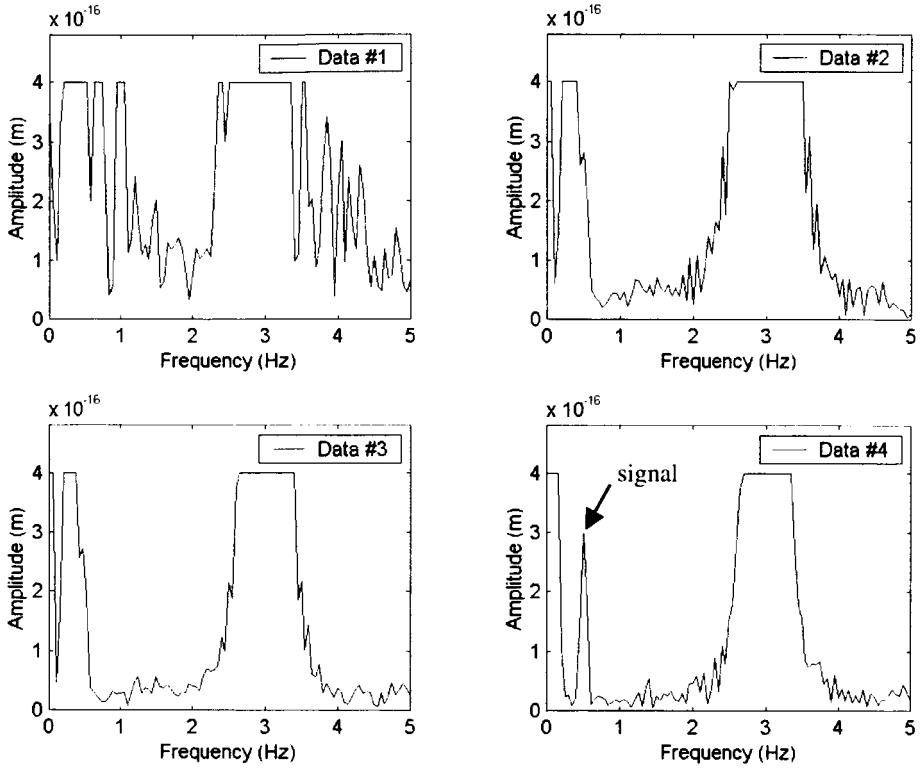

Figure 28 Windowed data with threshold cuts in the frequency domain.

Filtering of colored noise

Dynamic digital filtering

The motivation for using digital filters is twofold: To eliminate certain noise frequencies, and to resolve the signal. We examined a notch filter and a resonator. Both filters are IIR type that filter the signal via a dynamical process. The main disadvantage of dynamic filters is the transient time for convergence. Therefore, these filters are more adequate for long data spans. Nevertheless, we examined the possible advantages of these filters for our data.

The Notch filter has zeros at the required notch frequency (ω denotes the digital frequency). The transfer function of the second-order notch filter is:

$$H(z) = b\frac{1-2\cos\omega_0 z^{-1}+z^{-2}}{1-2b\cos\omega_0 z^{-1}+(2b-1)z^{-2}}$$

$b = \dfrac{1}{1+\tan(\Delta\omega/2)}$ where $\Delta\omega$ is the digital frequency width around ω_0.

The resonator has poles at the required signal frequency. The transfer function of the second-order resonator is:

$$H(z) = (1-b)\frac{1-z^{-2}}{1-2b\cos\omega_0 z^{-1}+(2b-1)z^{-2}}$$

$b = \dfrac{1}{1+\beta}$ where $\beta = \dfrac{G_B}{\sqrt{1-G_B}}\tan(\dfrac{\Delta\omega}{2})$ and G_B is the attenuation at $\omega = \omega_0 \pm \Delta\omega/2$.

In order to make $\Delta\omega$ as narrow as possible the radius of the poles (resonator) or zeros (Notch filter) must approach the unit circle. However, the filter time constant increases as the radius approaches one. Thus, there is a tradeoff between accuracy and convergence speed. The number of samples (time constant) to converge to ε from the steady state given radius R is $\eta = \ln(\varepsilon)/\ln(R)$. The relation between the radius and the frequency band is approximately: $\Delta\omega \approx 2(1-R)$. The digital frequency for our signal is $\omega_0 = 0.01\pi$ (rad/sample) and the digital frequency range, for a frequency band of 0.1 Hz (0.05 Hz from each side), is $\Delta\omega_0 = 0.002\pi$ (rad/sample). Therefore, the number of samples to converge with $\varepsilon = 0.1$ is 730 and the number of samples to converge with $\varepsilon = 0.01$ is 1460. Testing a notch filter with our data showed three disadvantages. First, some noise shifts toward the signal frequency, especially when there is not enough separation between signal and colored noise (data 1 thru 3). Second, the transient time is about half of the record time, as explained above. In order to extract the signal we need to run the resonator for the rest of the data (the tail) or to apply another signal extraction method. The tail is marginally sufficient for another dynamical filter and also contains

only about half of the original physical resolution. Third, a notch filter is perfect for removing an isolated harmonic noise (for instance, removal of the AC interference from ACG signal) but is less efficient for removing a non-stationary noise (data 2 thru 4).

We tested the resonator as follows. We first pre-filtered the data using amplitude cut filter with amplitude threshold of 10^{-15} m (about three times larger than the expected signal). With $\omega_0 = 0.01\pi$ we estimated the amplitude at ω_0 using a frequency band of 0.1 Hz.

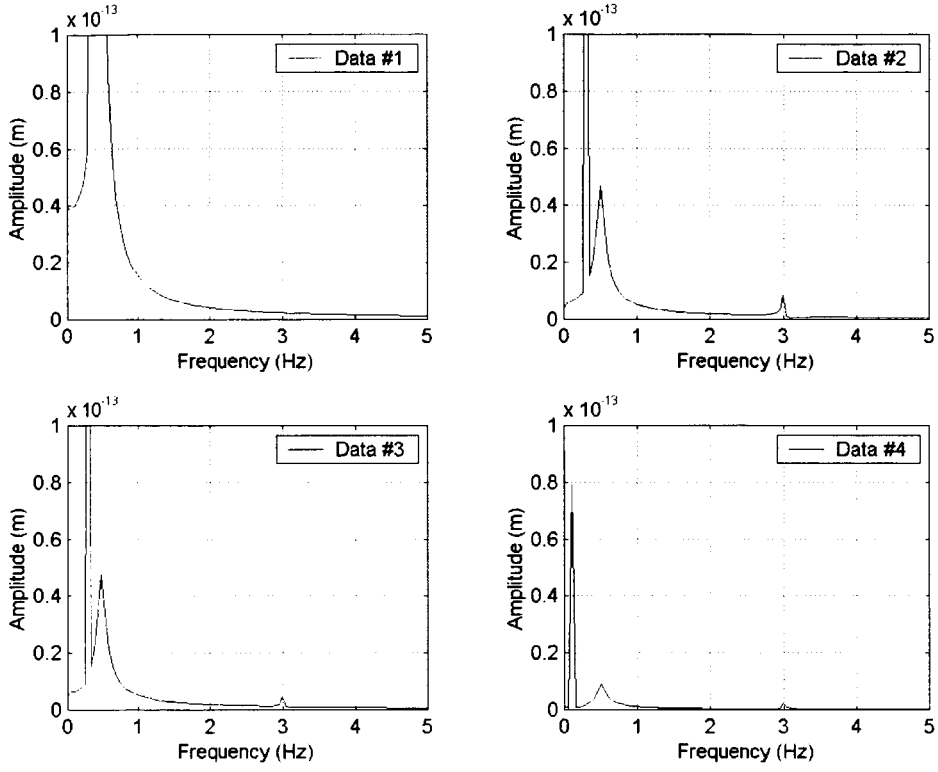

Figure 29 The output of a resonator applied to the raw data.

Figure 29, that shows the filtered data without pre-processing the cuts, demonstrates the necessity of the amplitude cut. The amplitude at 0.5 Hz is an alias of the colored noise at lower frequency. We obviously can not reveal the signal with the original colored noise. Note that a possible peak at 0.5 Hz is due to the choice of the peaking frequency and not to the real signal.

Figures 30 and 31 show the results from the application of the resonator to the pre-filtered noise. The noise in Fig. 30 is colored while the noise in Fig. 31 is a combination of colored and white ($\sigma = 1 \times 10^{-15}$).

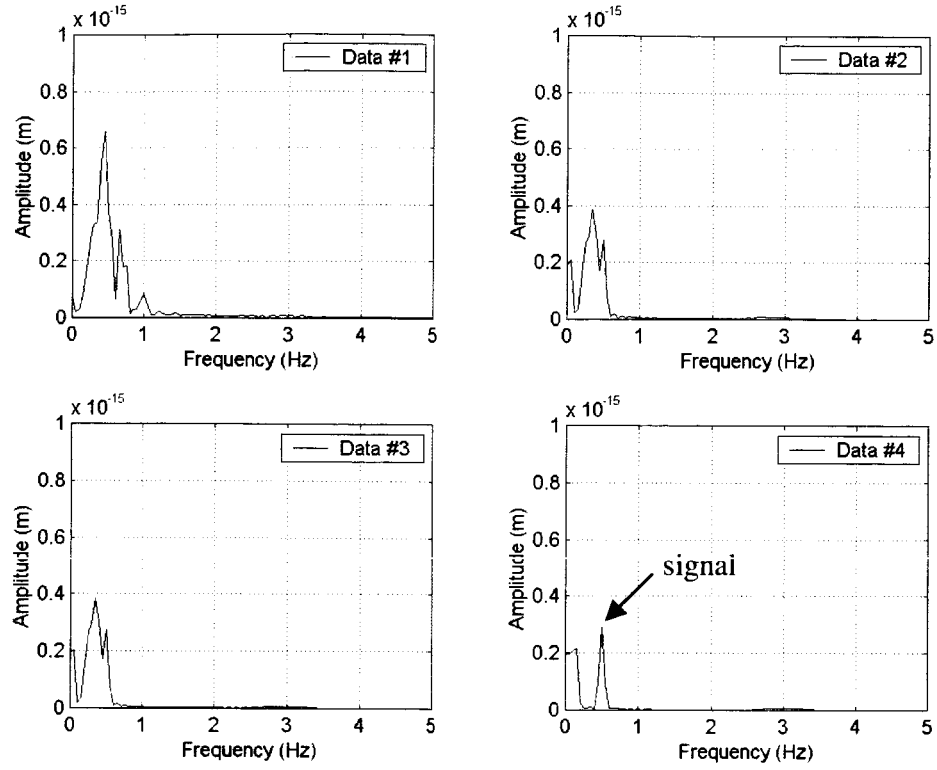

Figure 30 The output of a resonator applied to a filtered data (no white noise).

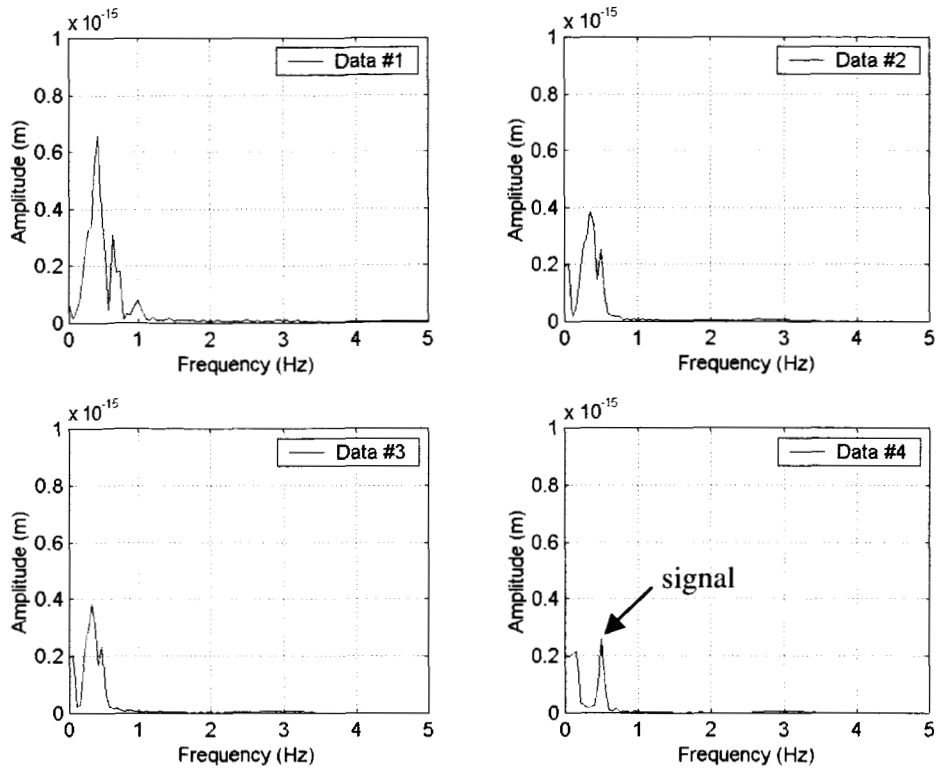

Figure 31 Output of a resonator applied to a filtered noisy data.

Figures 32 and 33 show validation tests in which the signal is absent. The noise in Fig. 32 is colored while the noise in Fig. 33 is white. It is obvious that the resonator picks some low frequency colored noise when the separation of signal/noise is poor. In addition, it picks some white noise. Since generally speaking there is no pure white noise, the component of the white noise that the resonator picks is always unpredictable.

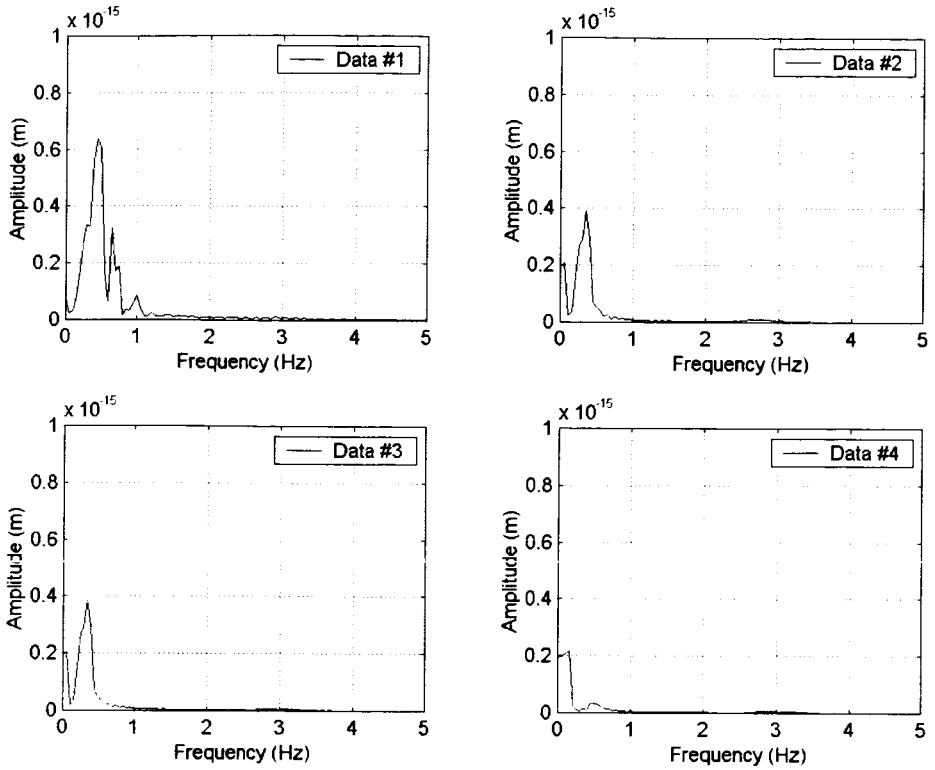

Figure 32 The output of a resonator for a colored noise (no signal).

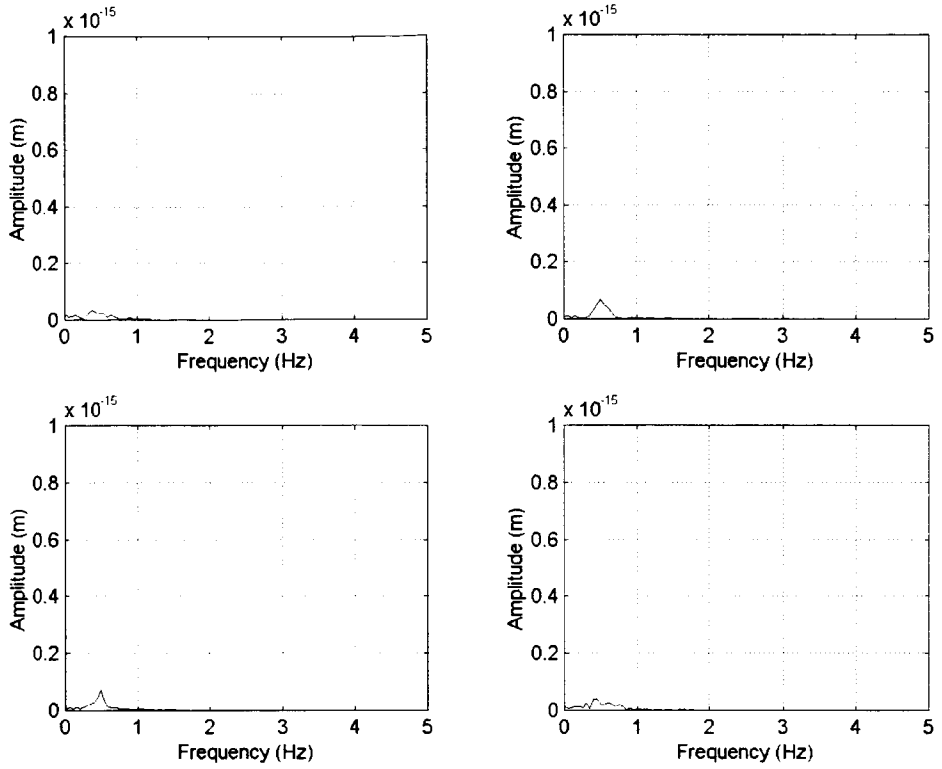

Figure 33 The output of a resonator for a white noise (no signal).

Least square filtering

Since the signal frequency as well as some components of the colored noise frequencies are known, we try to fit these harmonics. The model should include as many known frequencies as possible. For optimal fit, the unmodeled noise should be white. In any case, there are some unmodeled frequencies, so the estimator is sub-optimal in the best case. One may attempt to estimate the colored noise amplitude and then subtract the estimation from the data. This process would not work well unless all the modeled colored noise consists of pure harmonics and all frequencies are modeled. We modeled the estimator as: $X = H\Theta + n_c + n_w$, where X is an N-array sampled data, Θ is an $2n + 3$array of unknown amplitudes, and n_c, n_w are the unmodeled colored noise and a white Gaussian noise respectively. There are n modeled frequencies and an additional free frequency. The free frequency is close to the signal frequency. The reason will be explained later. The corresponding $N \times (2n + 3)$ model matrix is:

$$H = \begin{bmatrix} 1 & \cos\omega_1 t_1 & \sin\omega_1 t_1 & \cdots & \sin\omega_n t_1 & \cos(\omega_n + \delta\omega)t_1 & \sin(\omega_n + \delta\omega)t_1 \\ 1 & \cos\omega_1 t_2 & \sin\omega_1 t_2 & \cdots & \sin\omega_n t_2 & \cos(\omega_n + \delta\omega)t_2 & \sin(\omega_n + \delta\omega)t_2 \\ \vdots & \vdots & & & & \vdots & \\ 1 & \cos\omega_1 t_N & \sin\omega_1 t_N & \cdots & \sin\omega_n t_N & \cos(\omega_n + \delta\omega)t_N & \sin(\omega_n + \delta\omega)t_N \end{bmatrix}$$

where $\omega_j = 2\pi f_j$.

Because of is the relative closeness of some frequencies, we applied a Singular Value Decomposition to compute the pseudo-inverse. That is, $H = USV^T$ where U is $N \times N$ orthogonal matrix, V is $(2n+3) \times (2n+3)$ orthogonal matrix, and S is $N \times (2n+3)$ diagonal matrix that consists of the singular values. The estimate amplitude array is:

$\hat{\theta} = V(S^T S)^{-1} S^T U^T$ with a Covariance matrix of : $\hat{\theta} = \sigma^2 (H^T H)^{-1}$.

We tested the Least Square algorithm as follows. After pre-filtering (as done in the previous section) we applied LS with four frequencies (in addition to a bias): two dominants colored noise frequencies, the signal frequency and one frequency near the signal.

We tested the LS with the four data sets and a White Gaussian noise (WGN) with a variance $\sigma = 10^{-16}$ (see Fig. 24). We estimated the amplitude (squares) at the signal frequency and the amplitudes at a couple of frequencies on each side of the signal (note that the model matrix becomes ill defined if a frequency is too close to the signal). The circles show the amplitude of the noise without the signal (null signal). The size of the squares is the error estimate. The criteria for the existence of a signal should be a visible amplitude peak. Only the signal at data #4 has a clear peak. Data #3 has some peak while the amplitude estimation of data #1 and data #2 does not reveal the signal. If we had a reference noise (circles) we could reveals the signal from each data.

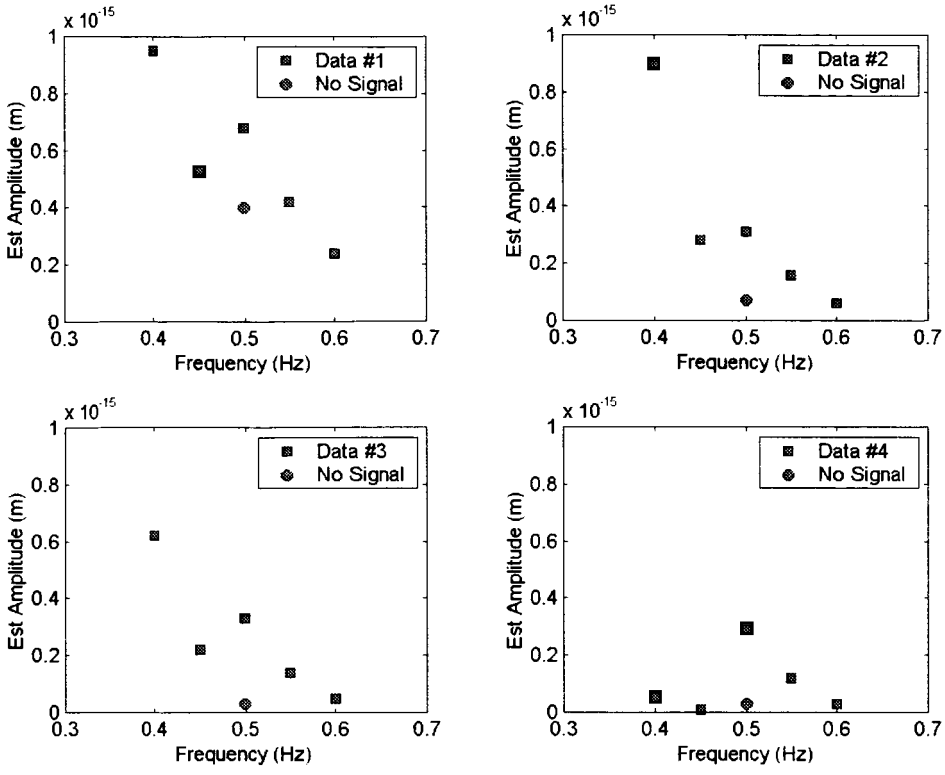

Figure 34 Amplitude estimation in the vicinity of the signal (with white noise) using LS.

White noise filtering

Model

We assume that we have eliminated the colored noise so the processed data consists of a pure white noise and a hypothetical signal. We further assume that the white noise is a WGN with a variance σ^2.

There are two hypotheses that describe the possible scenarios:

Noise only: $H_0: \; x[n] = w[n]$

Noise and a signal: $H_1: \; x[n] = s[n] + w[n]$

Our purpose is to detect and estimate the signal. It is not sufficient to estimate the signal amplitude because we may pick up a noise with the same frequency as the signal. For example, a resonator would show a peak at the desired frequency (for a dense white noise), even for a null signal. Therefore, in addition to an amplitude estimator we need to evaluate the confidence of

our estimation. Given a probability of false alarm (as small as possible) we would like to maximize the probability of detection.

The main assumption is that the signal frequency and phase are known and the noise is a white-Gaussian, therefore:

$$p(x;H_0) = \frac{1}{(2\pi\sigma^2)^{N/2}}\exp[-\frac{1}{2\sigma^2}\sum_{N=0}^{N-1}(x[n])^2]$$

$$p(x;H_1) = \frac{1}{(2\pi\sigma^2)^{N/2}}\exp[-\frac{1}{2\sigma^2}\sum_{N=0}^{N-1}(x[n]-s[n])^2]$$

where $x = [x[0]\, x[1] \cdots x[N-1]]^T$. We tested a unit signal with different SNR. The sampled data (dots) is presented in Fig. 35 together with the true signal (solid line).

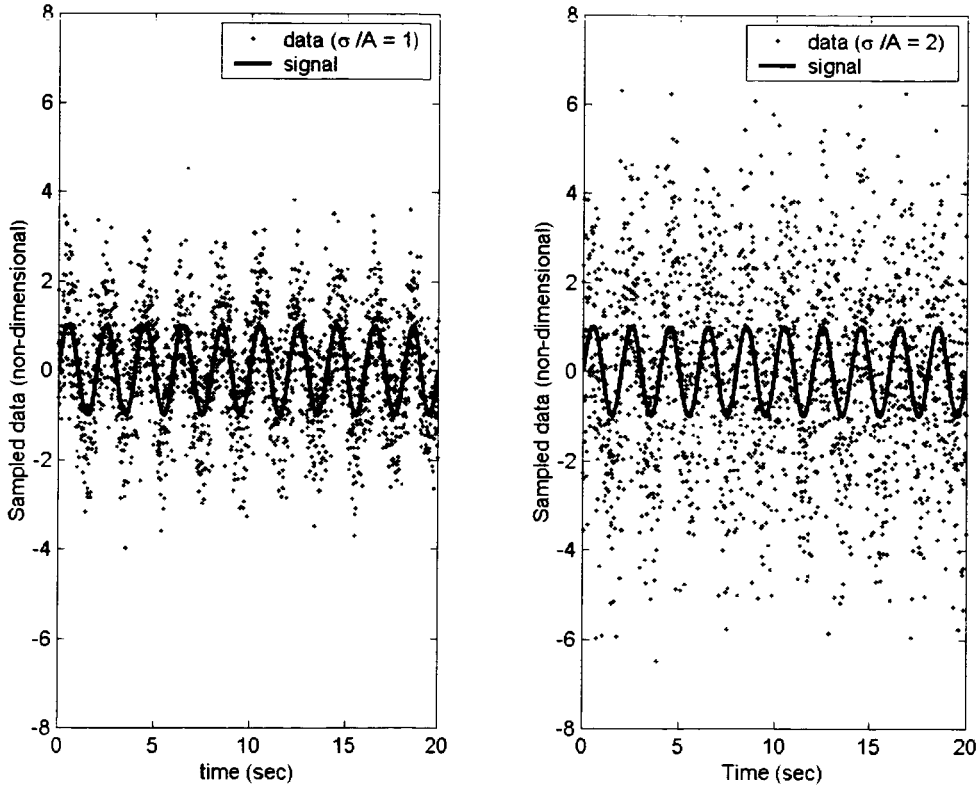

Figure 35 Signal with a white noise.

Signal detection

Each sample data $x[n]$ is considered as a random variable with two possible probability distributions: a Gaussian with zero-mean for the null hypothesis, H_0, and a Gaussian centered at the expected amplitude for H_1. We then assign a threshold γ and classify a detection or null-detection according to the value of the data with respect to the threshold. The threshold is related to the probability of false alarm and to the probability of detection as follows:

$$P_{FA} = P(H_1;H_0) = P\{x > \gamma;H_0\} = \int_{\gamma}^{\infty} p(x;H_0)\,dx$$

$$P_D = P(H_1;H_1) = P\{x > \gamma;H_1\} = \int_{\gamma}^{\infty} p(x;H_1)\,dx$$

The threshold is a function of the probability of false alarm. Given P_{FA} our aim is to find the amplitude that maximizes P_D. Note that in general the unknown parameters are amplitude, phase and frequency. We used the Generalized Likelihood Ratio Test (GLRT) and decided for H_1 according the following likelihood criterion:

$$\frac{p(x;\hat{A},H_1)}{p(x;H_0)} > \gamma$$

where $\hat{A}$ is the Maximum Likelihood Estimation (MLE) of A given in the next section.

When the amplitude is the only unknown we can express H_1 as: $A\,s[n] + w[n]$, where S is a given reference signal. This case is much simpler than the general case (unknown amplitude, phase and frequency).

The model can be written as: $x = \mathbf{H}A + w$, where $\mathbf{H} = [s[0]\ s[1] \cdots s[N-1]]^T$, therefore the hypothesis is now:

H_0: $\hat{A} = 0$

H_1: $\hat{A} > 0$

It can be shown that we can select H_1 (for unknown amplitude) if

$$\frac{\sum_{n=0}^{N-1} x[n]s[n]}{\sum_{n=0}^{N-1} (s[n])^2} > \gamma' = \sigma^2 \ln\gamma + \frac{1}{2}\sum_{n=0}^{N-1} (s[n])^2$$

where γ' is related to P_{FA} by $P_{FA} = 2Q(\sqrt{\gamma'})$.

The best P_D in the sense of maximum likelihood is:

$$P_{FA} = Q\left(Q^{-1}\left(\frac{P_{FA}}{2}\right) - \sqrt{\frac{\mathbf{E}}{\sigma^2}}\right) + Q\left(Q^{-1}\left(\frac{P_{FA}}{2}\right) + \sqrt{\frac{\mathbf{E}}{\sigma^2}}\right)$$

where the signal energy is defined as: $\mathbf{E} = A^2 \sum_{n=0}^{N-1} (s[n])^2$.

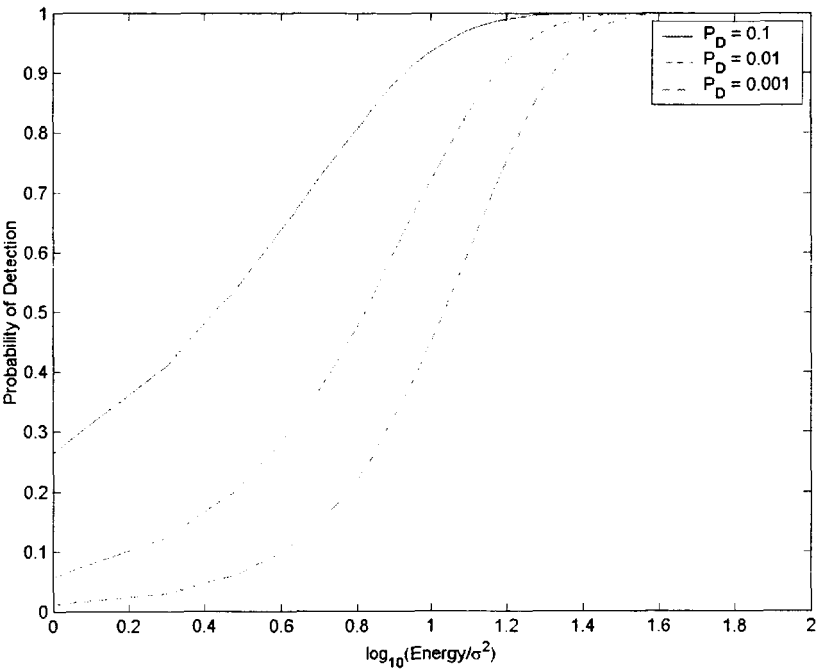

Figure 36 Probability of detection Vs energy-to-noise ratio.

The relation between the signal-to-noise energy ratio ($\log_{10}\frac{NA^2}{2\sigma^2}$) and the probability of detection, given several probabilities of false alarm is shown in Fig. 36. Our signal is obviously detectable with excellent probability for noise variance of few orders of magnitude greater than the signal amplitude. However, probability of detection does not tell about the accuracy of the signal amplitude estimate (see later).

Signal estimation

The amplitude is the only unknown so the amplitude estimate becomes quite simple using the model: $x = \mathbf{H}A + w$. The MLE of the amplitude is:

$$\hat{A} = (\mathbf{H}^T\mathbf{H})^{-1}\mathbf{H}^T x = \frac{\sum_{n=0}^{N-1} x[n]s[n]}{\sum_{n=0}^{N-1} (s[n])^2}$$

We examined the quality of the above estimation for a signal with a variety of white noise. The estimation quality depends only on the SNR, so we assign the signal as a unit sinusoid with frequency of 0.5 Hz and checked it with different noise variances. Since the 20-s computer generated white noise is not a pure white noise, we repeated the test in a Monte Carlo fashion. The plots in Fig. 37 show the probability distribution (cumulative frequency distribution) of the amplitude estimate for 100 runs. Each plot represents a different SNR. The broken line indicates the mean estimate (the true amplitude is one). The probability distribution approach a Gaussian as the number of runs increases, as expected from the problem formulation. The amplitude estimation is quite good considering that the white noise is greater than the signal.

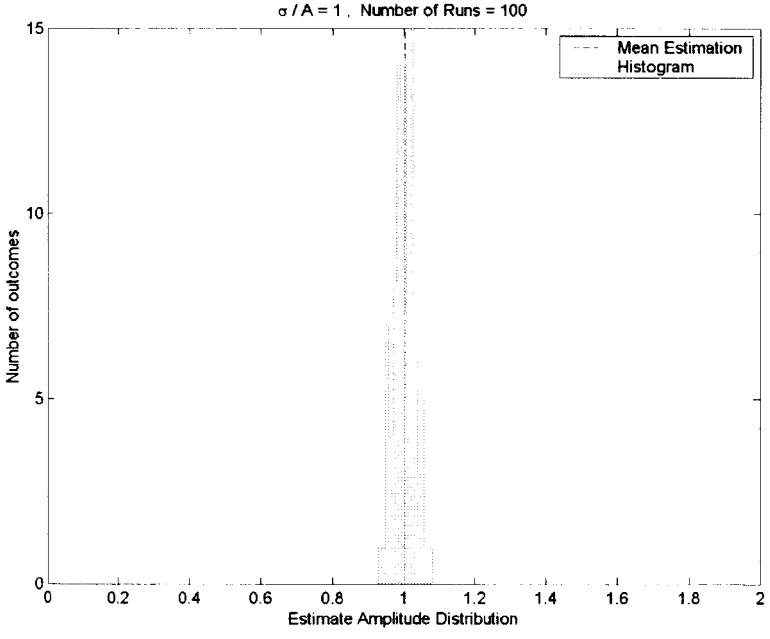

(cont'd)

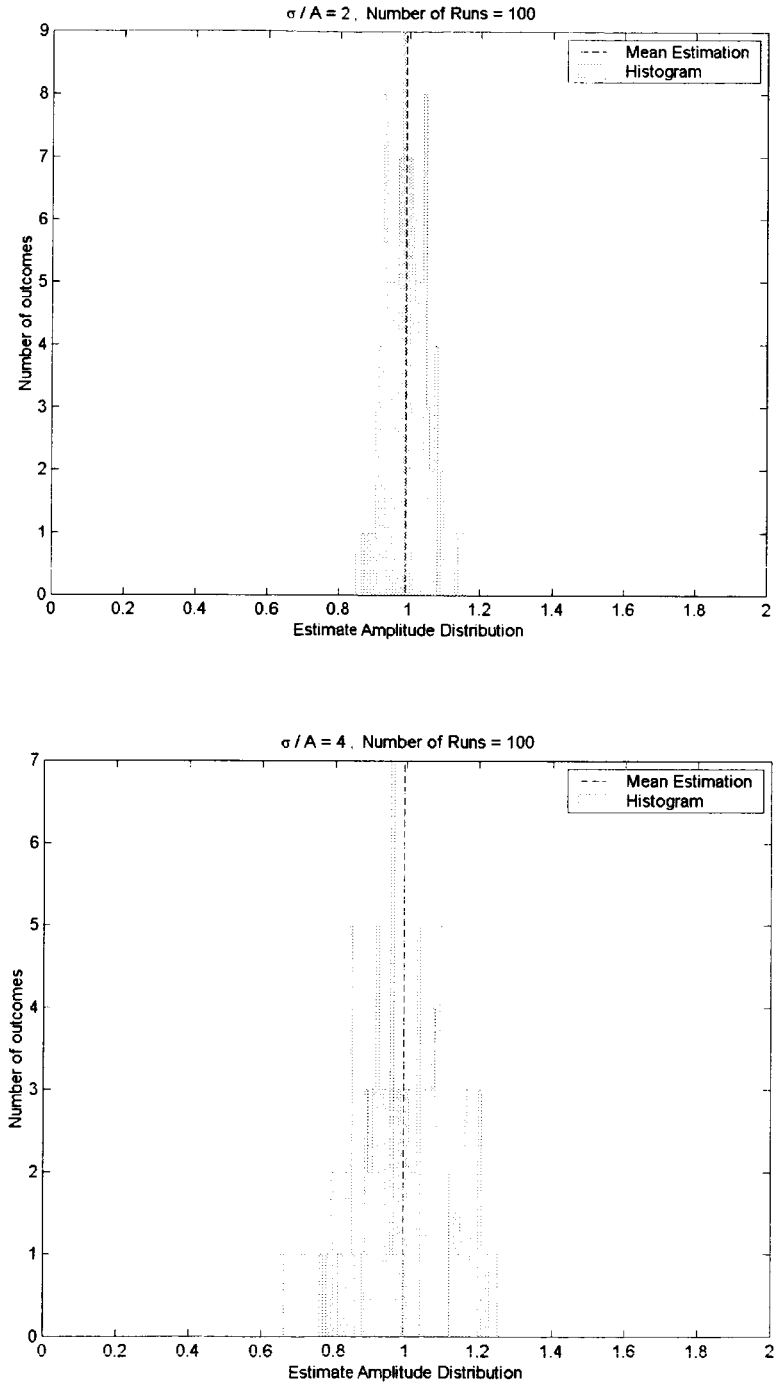

Figure 37 Amplitude cumulative frequency distributions using MLE for different signal-to-noise ratios.

Summary and Recommendations

We summarize the advantages and disadvantages of the methods examined in Table 1.

Table 1 Comparison of the various methods.

Method	Advantage	Disadvantage
Windowing	Better observability	Less resolution
Segmentation	Better SNR	Less resolution
Amplitude cuts	Removes colored noise in specific band	Colors the white noise
Notch Filter	Remove colored noise	- Requires transient time $\Rightarrow$ less resolution -The colored noise should be in isolated harmonics - Does not preserve signal
Resonator	Picks the signal directly	- Requires transient time $\Rightarrow$ less resolution - Picks the white noise - No detection confidence estimate
LS Filter	Estimates the amplitudes of the colored noise and the signal amplitude	- Requires a model of the noise - Only estimate error but no detection confidence estimate
GLRT	Estimates the amplitude of the signal and estimates the detection confidence	Requires a pure white noise

The method to use for the real experimental data depends on the nature of the data. Pre-filtering such as windowing and amplitude cuts are recommended for any type of data. Filters such as the resonator and the least square can be used when the separation between the signal and the low frequency colored noise is sufficient. Least square filter is preferable for a large white noise. However, least square requires good modeling of the noise while the resonator is model free. GLRT is the best method when the white noise is large. However, it is optimal for a pure WGN while the whiteness of our post-processed data is not perfect.

The most important future work is to test the performance of the GLRT with a filtered colored noise. We executed some preliminary tests of complete cuts that eliminated the noise bellow the signal frequency and up to 3 Hz. We tested the GLRT with the inverse Fourier transform of the processed data. Except data #1, the estimation is reasonable and *very good for the case of data #4*. Note that although the white noise is far from ideal, the amplitude estimation works quite well. Data #4 is a simulated output of the purely rotational detector configuration with pivot axis perpendicular to the spin axis. Note also that the colored noise level for the configuration with pivot axis parallel to the spin axis is even lower than in data #4.

In conclusion, the approach that gave the best results for the extraction of the small EP violation signal from a prevalent colored and white noise is as follows:

Apply Window to data -> Apply Discrete Fourier Transform -> Remove colored noise in frequency domain through amplitude cuts ->Apply Inverse Discrete Fourier Transform -> Apply Maximum Likelihood Estimation and match filtering.

The data set #4 (from the purely-rotational detector's configuration) proved to be the most amenable to signal extraction thanks to the good frequency separation between the colored noise and the signal, and the low level of dynamics-related noise at the signal frequency.

Symbols and Abbreviations

A = signal amplitude (unknown)
DFT = Discrete Fourier Transform
$E(x)$ = expected value of x
E = signal energy
FFT = Fast Fourier Transform
FIR = Finite Impulse Responce
$GLRT$ = Generalize Likelihood Ratio Test
$\mathbf{H}$ = observation matrix
H = hypothesis
IIR = Infinite Impulse Responce
LS = least square
γ = threshold
MLE = Maximum Likelihood Estimation
N = number of samples
$p(x)$ = probability density function
$p(H_i; H_j)$ = probability of H_i when H_j is true
P_D = probability of detection
P_{FA} = probability of false alarm
$Q(x)$ = probability that a random variable exceeded x in a Gaussian probability distribution
σ^2 = variance
s = signal
SNR = Signal to Noise Ratio
w = noise
x = data

Mechanical Design of Spin and Release Mechanism

System Operation Description

The most important requirement on the sensor support and release system is that it releases the sensor smoothly during the experiment. In order to do this, the support system must hold the sensor against large launch loads, rotate the sensor package up to the desired spin frequency (~0.5Hz) and release the sensor without imparting unacceptable lateral dynamics to the package. This is accomplished by a design assembled from a number of specialized systems. At the inside, the instrument package is held on either side in a 3 point kinematic connection consisting of 3 ball joints each. The balls are arranged to avoid over-constraint. To ensure that possibly large launch loads do not knock the sensor out of position, there is a launch lock for the launch phase of the flight. Once aloft, the launch lock will be removed from position. Next there are two (one on each side) voice coil/flexure linear stages that allow the sensor to be released smoothly. These are each, in turn, mounted on smooth rotary stages that accomplish the sensor spin up. Finally, this whole system is mounted on a standard ball slide, linear stage which pulls this whole system out of the way (see Fig. 38).

Well before release, the sensor package is spun up to 0.5 Hz. Release is accomplished by the two equivalent voice coils on either side of the sensor. These pull quickly the ball mounts out of position on a set of flexures. The system is designed to have no sliding elements that take part in this motion. Since the voice coil/flexure system has a very limited travel, once the sensor is rotating freely, the entire sensor support is moved out of the way by the two linear stages that support each of the voice coil actuated mounts. The sensor package is now in position to rotate without impacting the mass of the supporting structure.

Mechanical Description – Release Mechanism and Support Structure

Rotation and Release Assembly

The instrument package is held in place and rotated between two, three-ball kinematic mounts. Each kinematic mount containing the three balls is fastened to a linear voice coil actuator. To release the detector package, the actuators are energized in reverse to pull the kinematic mounts away by 4 mm each end along the rotation axis. The 4-mm travel will take 0.1 sec. The rotating, actuator field assemblies retract the kinematic mounts while the non-rotating coil assemblies are attached to the stator housing. See Rotation and Release Assembly, Fig. 39. Thin, Titanium flexures are attached to both ends of the field assembly and both ends of the internal, rotating actuator housing. A brushless DC motor rotates the instrument package through the flexures, voice coil actuators and kinematic mounts.

Long Travel Linear Actuators and Support Structures

Each Rotation and Release Assembly is held in place with side plates attached to a linear motion (LM) block (see Fig. 38) mounted to a rail and experiment support channel above the instrument package and its clearance envelope.

Additional linear travel of 10 cm, in about 1 s, immediately after the 4-mm release translation is accomplished using an electric thrust cylinder (2 req'd) coupled to the LM block and mounted to brackets attached to the experiment support channel. The experiment support channel is fastened to mounting brackets welded to the inside of the cryostat ID.

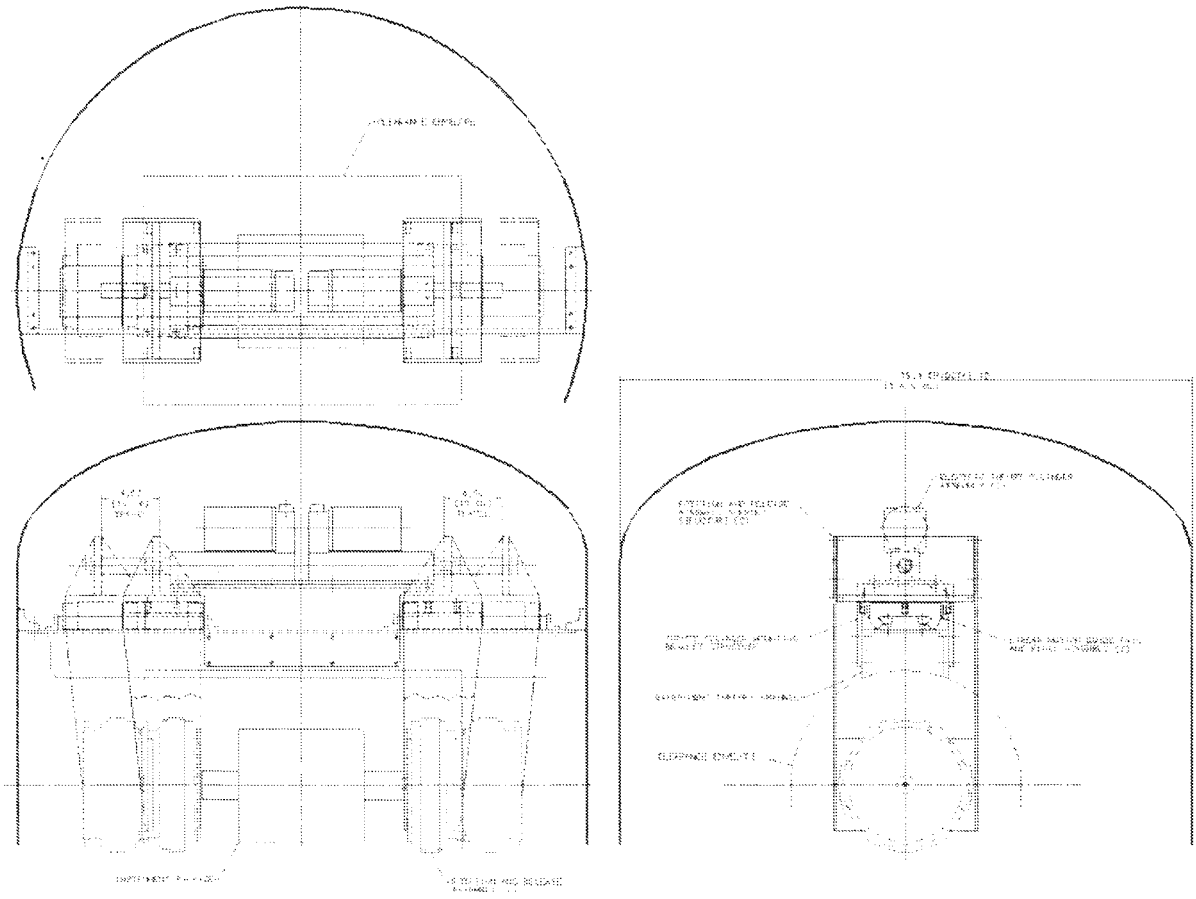

Figure 38 Spin and release mechanism and its support structure.

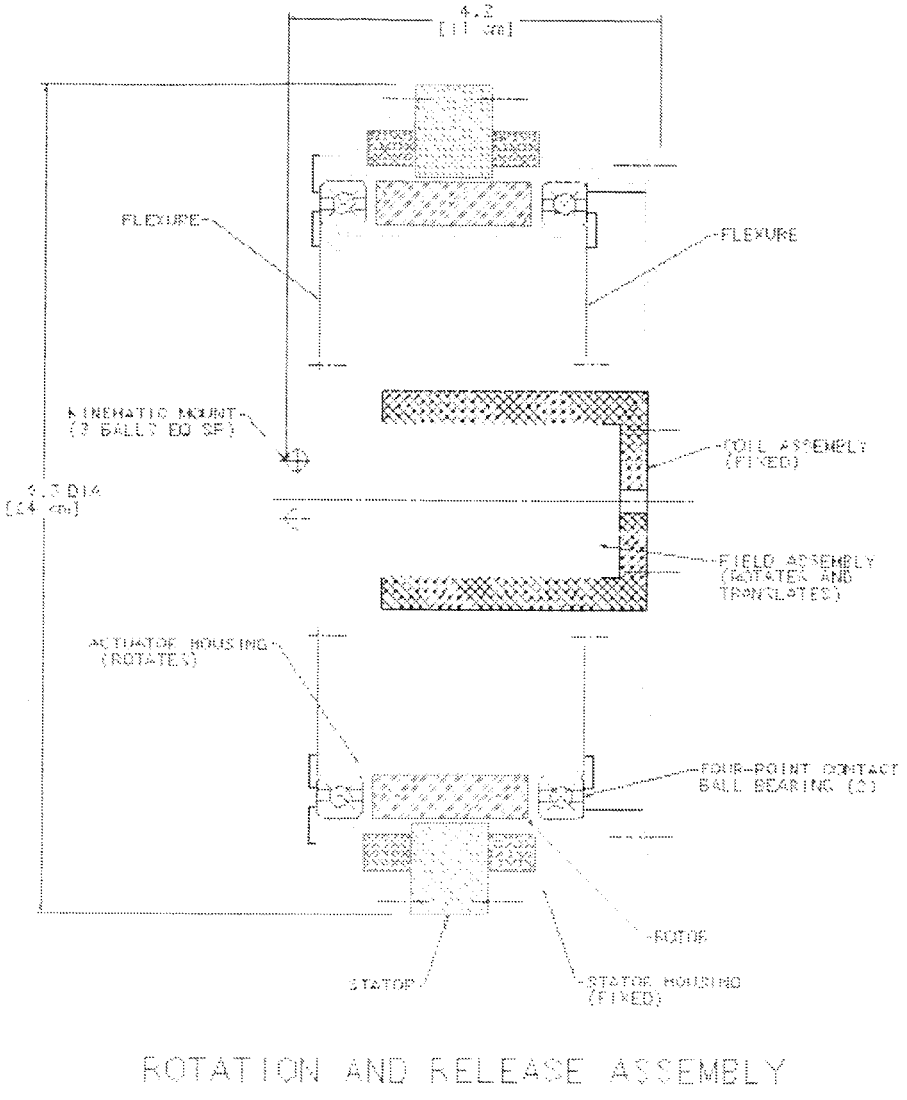

Figure 39 Spin system and voice coil actuator (first stage of release).

Parts specification

ELECTRICAL THRUST CYLINDER (2 REQ'D):

IDC MODEL NO. N2-S32 (V) -25-5B (WITH MOTOR BRAKE)
2.5 / 1 HELICAL GEARS, 5 REV INCH BALL SCREW
MAX SPEED: 4 IN/S (100 mm/s)
MAX THRUST: 600 LB (2670 N)
LINEAR STROKE: 4 IN. (100 mm)
MOTOR: 1.8 deg/step PERMANENT MAGNET HYBRID STEP MOTOR
POWER (PEAK): 150 W
POWER INTERMITTANT DUTY CYCLE: 100 W
WEIGHT (QTY 2 CYLINDERS): 19.0 LB (8.6 kg)

LINEAR MOTION GUIDE RAIL AND LM BLOCK (2 RAILS AND 2 BLOCKS REQ'D):

THK MODEL NO. HRW 50 CA
4-ROW CIRCULAR ARC CONTACT DESIGN WITH RECIRCULATING BALLS
DYNAMIC LOAD RATING: 11,295 LB (50.2 kg)
STATIC LOAD RATING: 18,338 LB (81.5 kg)
MATERIALS (BLOCKS, RAILS AND BALLS): STAINLESS STEEL
LENGTH OF RAILS: 10.3 IN.(26 cm)
WEIGHT (TOTAL, RAILS AND BLOCKS): 7 LB (3.2 kg)

LINEAR VOICE COIL ACTUATOR (2 REQ'D):

MODIFIED BEI MODEL NO. LA25 - 42
PEAK FORCE: 60 LB+ (267 N+)
STROKE REQUIRED: 0.16 IN (4.0 mm)
STROKE TIME: 0.1 s
POWER: 375 W
WEIGHT (QTY 2 ACTUATORS): 4.4 LB (2 kg)

BRUSHLESS DC MOTOR (2 REQ'D):

MODIFIED BEI MODEL NO. DIP90 - 15 - 001Z
PEAK TORQUE: 3.9 LB-FT (5.3 NM)
POWER: 28 W

EXPECTED RPM @ RELEASE: 30 RPM
WEIGHT (QTY 2 MOTORS): 11.0 LB (5.0 kg)

FLEXURES (4 REQ'D):
MATERIAL: TITANIUM, 6AL4V GRADE 5
DIMENSIONS: THICKNESS = 0.001 IN (0.025 mm)
WIDTH = 0.197 IN (5.00 mm)
LENGTH = 1.1811 IN (30.00 mm)
FORCE REQ'D : 50 LB (222 N)

ROTATION AND RELEASE ASS'Y (HOUSINGS AND BEARINGS):
MATERIALS: STAINLESS STEEL
OVERALL DIMENSIONS: 9.3 IN. (24 cm) O.D. x 4.2 IN. (11 cm)
WEIGHT (2 ASSEMBLIES): 20.0 LB (9.1 kg)

ROTATIONS AND RELEASE ASS'Y SUPPORT STRUCTURE:
MATERIAL: 6061-T6 ALUMINUM ALL0Y
WEIGHT (2 ASSEMBLIES): 9.0 LB (4.1 kg)

THRUST CYCLINDER MOUNTING BRACKET STRUCTURE:
MATERIAL : 6061 -T6 ALUMINUM ALLOY
WEIGHT : 21 LB (9.5 kg)

EXPERIMENT SUPPORT CHANNEL:
MATERIAL: 6061-T6 ALUMINUM ASSOCIATION CHANNEL
WEIGHT: 9 LB (4.1 kg).

Summary of last-year activity at IFSI laboratory[1]

Construction of new differential accelerometer prototype

A new differential accelerometer prototype was built by the team at the IFSI laboratory. The new prototype consists of proof masses with pivot axes perpendicular to the spin axis (i.e., the vertical axis in Fig. 40(a)) and offset from the CM. The proof masses, which are concentric hollow cylinders, are attached to the detector's housing by means of elastic flexures at their upper edges (see Fig. 41). Unlike the previous prototype, the capacitive pick-ups are on the inner and outer surfaces of the cylinders.

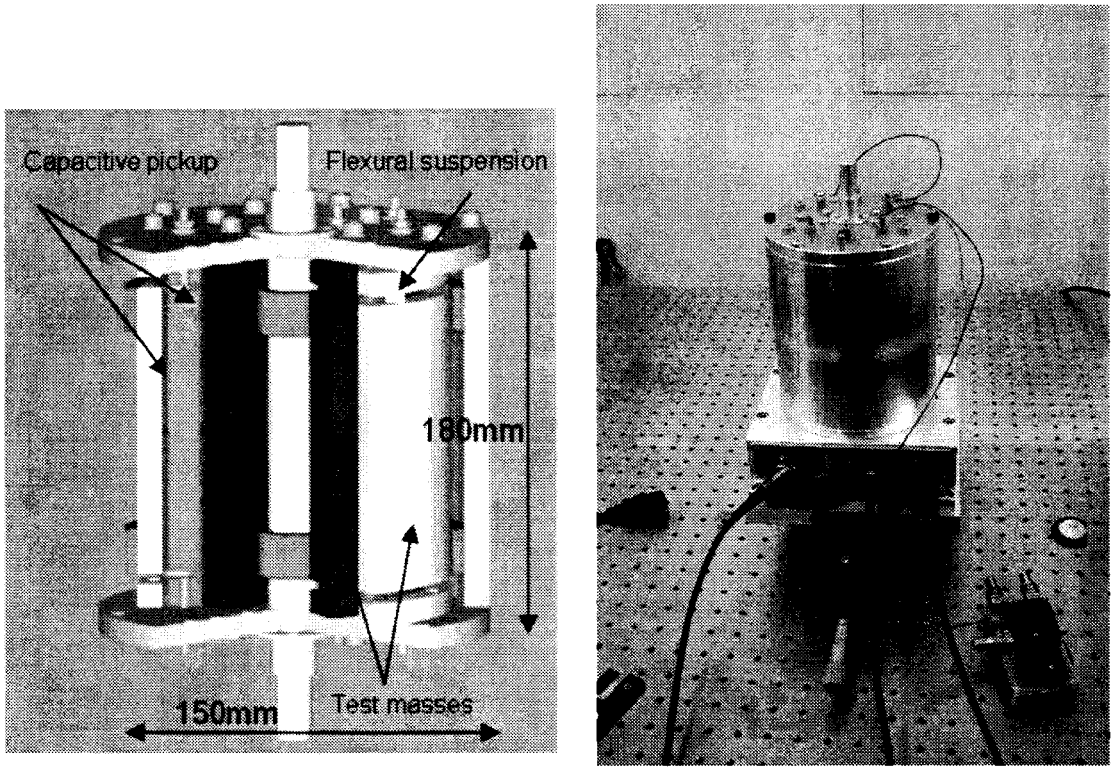

Figure 40 New differential accelerometer prototype: (a) cut-up view of proof masses and signal pickups; and (b) differential accelerometer assembled inside its vacuum chamber.

This pickup arrangement provides for a better electro-mechanical coupling of the accelerometer (i.e., a better conversion of mechanical energy into electrical energy) and an increase of the effective mass of the proof masses. Moreover, in the new prototype the CMs of the proof masses are coincident within the attainable construction accuracy.

[1] Section contributed by V. Iafolla, S. Nozzoli, D. Lucchesi, F. Santoli of the Institute of Interplanetary Space Phyiscs (IFSI) in Rome, Italy.

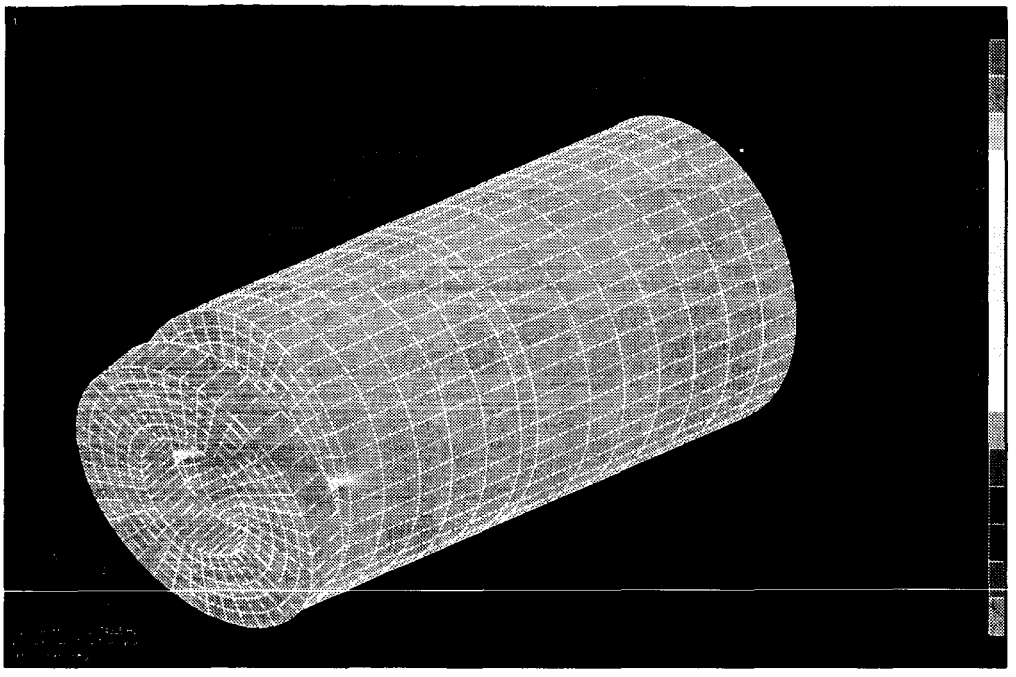

Figure 41 Finite element analysis of the proof mass vibration modes.

The proof masses in this prototype are both made of aluminum. The internal mass is 0.96 kg and the external mass is 1.1 kg. The resonant frequency in a 1-g environment depends on the top-up (regular pendulum) or top-down (inverted pendulum) orientation of the detector. The resonant frequency for the top-up configuration (that is normally used in the laboratory) is 2.28 Hz. Table 2 summarizes the key characteristics of the new differential accelerometer.

Table 2 Key characteristics of differential accelerometer prototype.

ITEM	VALUE
Internal proof mass	0.96 kg
External proof mass	1.1 kg
Resonant frequency (top-up)	2.28 Hz
Pre-amplifier noise temperature (commercial amplifier)	0.75 K

The development of the new prototype has occurred in parallel to the progress made in the analysis of the configuration for the flight-experiment detector. The new prototype adopts the roto-translational configuration which has many features in common with the purely rotational configuration. On the one hand, the roto-translation does not have the same degree of rejection of dynamics-related noise of the purely rotational configuration. On the other hand, the roto-translational configuration is amenable to more meaningful testing on ground because the motion of its test masses can be excited gravitationally by tilting the detector off the local vertical while the purely rotational configuration is practically insensitive to tilt.

Noise measurements of the new detector prototype

Introduction

This section illustrates the results of the experimental activity carried out in 2004 to evaluate the noise level of the new differential accelerometer prototype.

Measurements have been carried out with four different experimental setups:

1) The fist setup consists of the measurement electronics coupled to two reference capacitances on each channel that simulate the characteristics of the accelerometer. Lock-in amplifiers have been used for generating the polarization potential, signal demodulation and acquisition. This setup has been used to evaluate the effect of atmospheric pressure on the noise level of the electronics.

2) The previous electronics setup has been coupled to one sensor of the differential accelerometer to measure the seismic noise level. Moreover, we evaluated the input noise to the lock-in amplifiers.

3) Amplifiers have been added to the previous setup to amplify the polarization tension and increase the signal-to-noise ratio. We carried out measurements with reference capacitances on one channel while the other channel was coupled to the accelerometer sensor (excited by seismic noise).

4) In this setup, we added the input pre-amplifiers to the lock-in amplifiers to increase the signal-to-noise level and we carried out measurements of the electronics-related noise on one channel (with reference capacitances) and seismic noise measurements on the other channel.

The data acquisition was carried out with a sampling frequency of 64 Hz with data strings of about 15-minute each. A low-pass filter with a time constant of 10 ms and a cut-off attenuation of 14 dB/oct was used.

Summary of experimental results

Here we show a short summary of results while more details can be obtained from the relevant documents written by the IFSI laboratory team.

Table 3 shows a summary of the output voltage noise levels measured with setup 1 in which the measurement electronics is coupled to reference capacitances (simulating the acceleration sensors).

Table 3 Noise levels measured with setup 1.

Channel	Acquisition	Pressure (mBar)	Noise at 1 Hz V/sqrt(Hz)	Noise at 10^{-2} Hz V/sqrt(Hz)
1	EL 02	ambient	$2x10^{-6}$	$2x10^{-5}$
1	EL 03	$6.7x10^{-3}$	$1x10^{-6}$	$9x10^{-6}$
1	EL 05	$5.9x10^{-3}$	$2x10^{-6}$	$4x10^{-6}$
2	EL 02	ambient	$2x10^{-6}$	$2x10^{-5}$
2	EL 03	$6.7x10^{-3}$	$2x10^{-6}$	$2x10^{-6}$
2	EL 04	$5.9x10^{-3}$	$7x10^{-7}$	$1x10^{-6}$

In Setup 2 one channel was connected to the internal proof mass of the accelerometer while the other channel was connected to the reference capacitances. The two channels are marked by the letters I and E which are associated with the internal and external proof masses of the differential accelerometer. The measurements with the lowest noise level for this setup are shown in Figs. 42(a) and 42(b) that portray the time-domain signal and its frequency spectrum, respectively.

Setup 2 was also used to convert the voltage measurements into acceleration units (g) by tilting (by known values) the base plate of the detector prototype. The results of this calibration measurements are shown in Fig. 43.

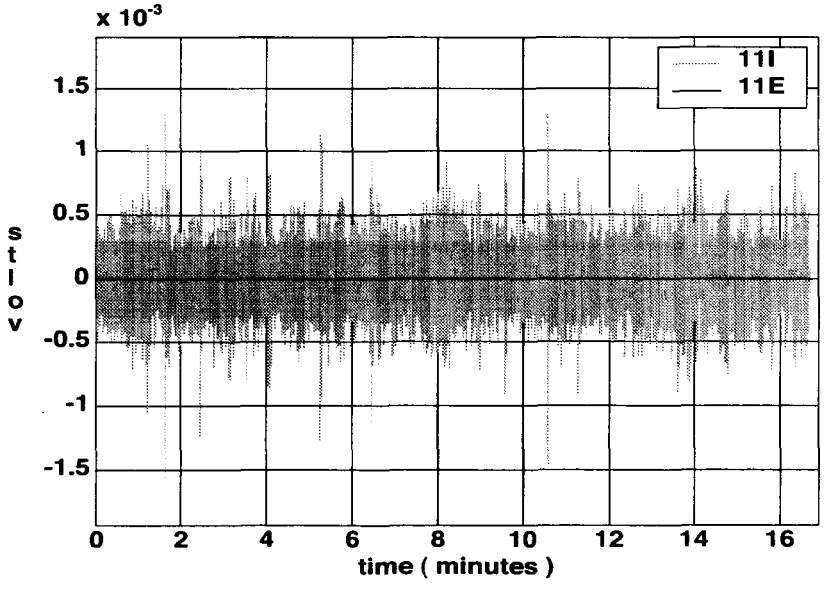

(a)

(cont'd)

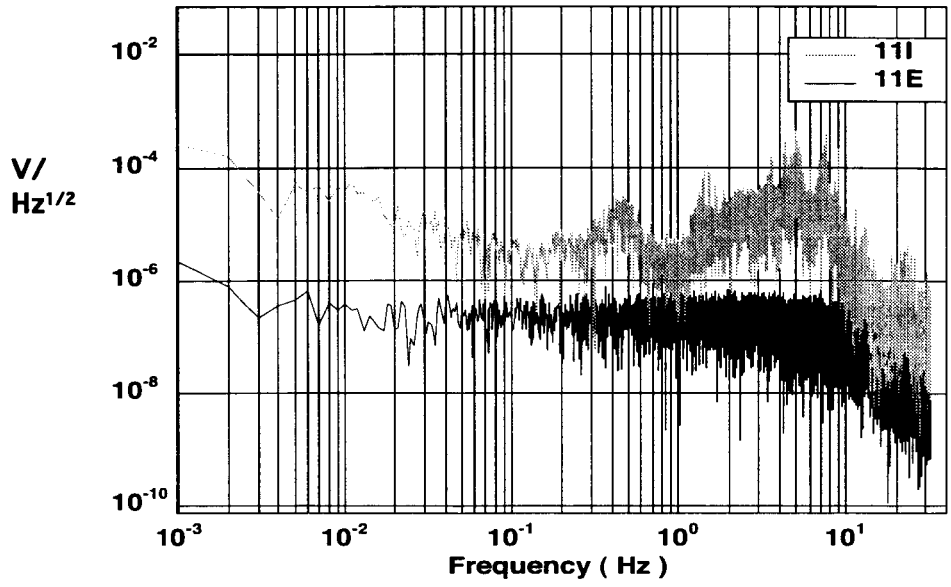

(b)

Figure 42 A sample of noise measurement taken with setup 2: (a) time-domain *(Volts)*, and (b) power spectral density ($Volts/\sqrt{Hz}$).

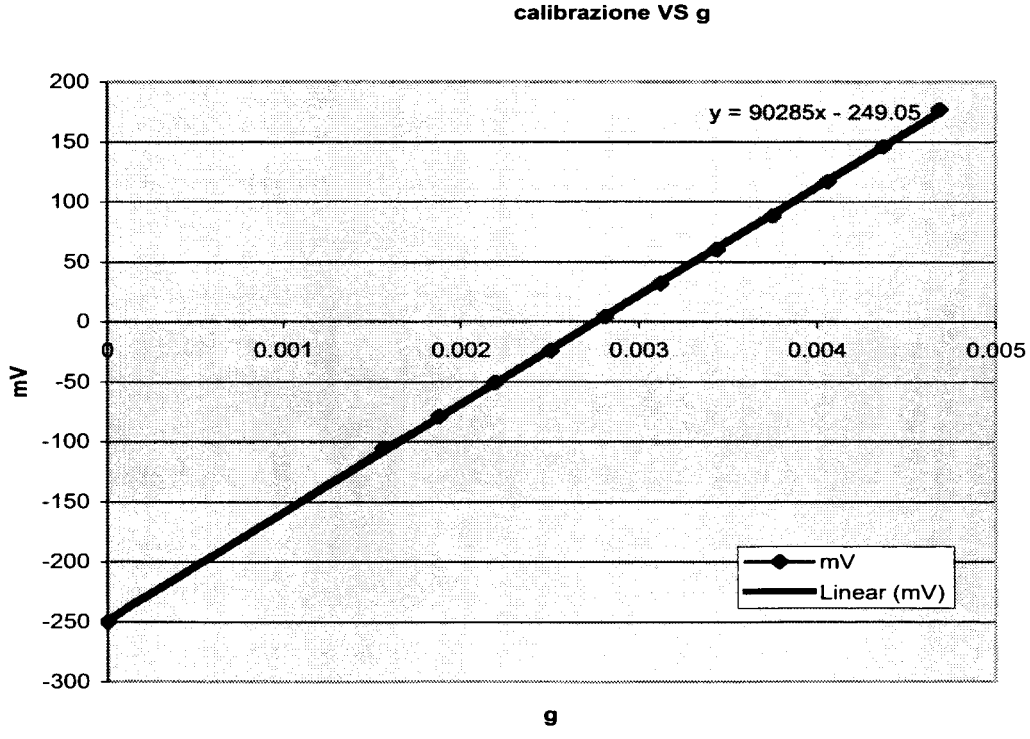

Figure 43 Calibration of detector's prototype output in acceleration units (g)

Finally, we have collected in Fig. 44 a consistent set of results obtained from measurements carried out with setup 2 (shown in black), setup 3 (green) and setup 4 (magenta) from the two channels. Note that setup 1 was not used to carry out measurements of seismic noise. The results are expressed in terms of acceleration power spectral densities ($g/\sqrt{Hz}$).

The upper group of lines is associated with channel 1 (connected to the internal proof mass) while the lower group of lines is associated with channel 2 (connected to the reference capacitances). The upper group of lines represent the seismic noise measured by the internal proof mass of the differential accelerometer. These lines are practically alike as it should be expected because the seismic noise does not change substantially with time.

The lower group of lines represent the noise level of the entire electronic measurement chain. The noise at low frequencies is attributable to external thermal effects while the noise at higher frequencies is associated with the input noise of the lock-in amplifiers.

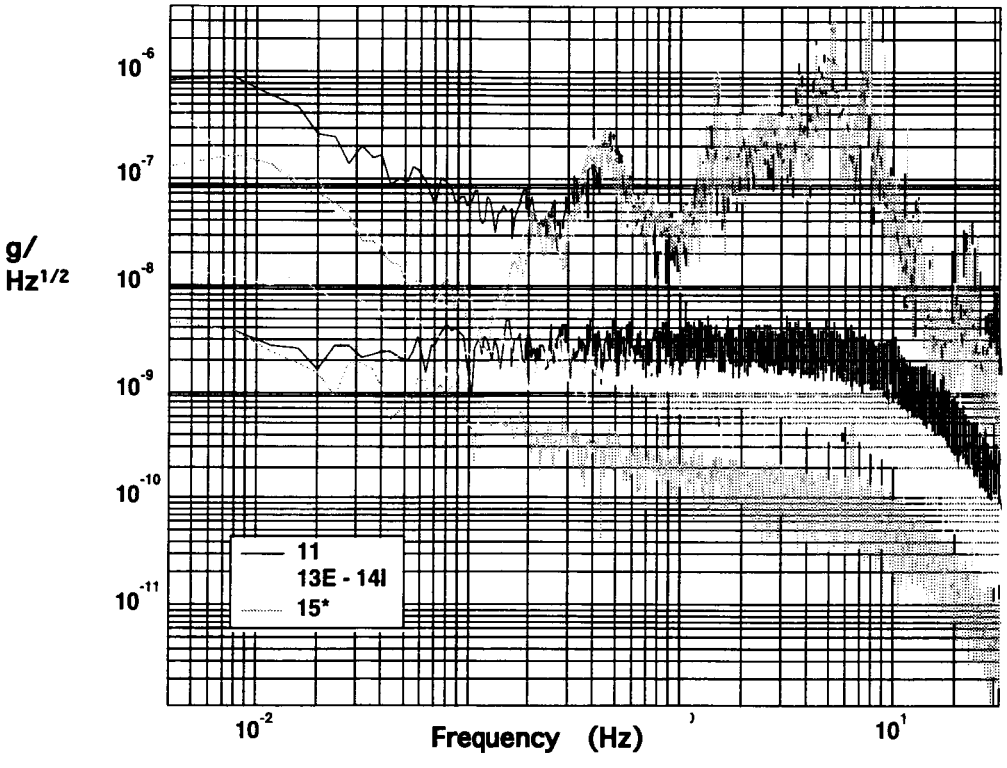

Figure 44 Acceleration spectral densities of a consistent set of measurements taken with setup 2 (black), 3 (green), and 4 (magenta). The upper curves are seismic noise measurements from the channel connected to the internal proof mass of the detector. The lower curves are noise levels of the electronic measurement chain from the channel connected to the reference capacitances.

The experimental results demonstrate that the electronics-related noise is much lower than the seismic noise even with commercial electronics operating at room temperature. Consequently, the accuracy of the measurements conducted in the laboratory will be limited by the seismic noise. Moreover, the arrangement of setup 4 exhibits the lowest level of electronics-related noise of those explored.

Preliminary measurements of common-mode rejection

Measurements with one lock-in amplifier

The measurement (GRT53) was carried out by utilizing the measurement scheme presented in Fig. 45. The seismic noise, measured by the internal mass, is sent to one lock-in amplifier and then to two channels of the data acquisition system. This measurement is needed to determine the upper limit of the common-mode rejection factor achievable with two lock-in amplifiers and two sensors.

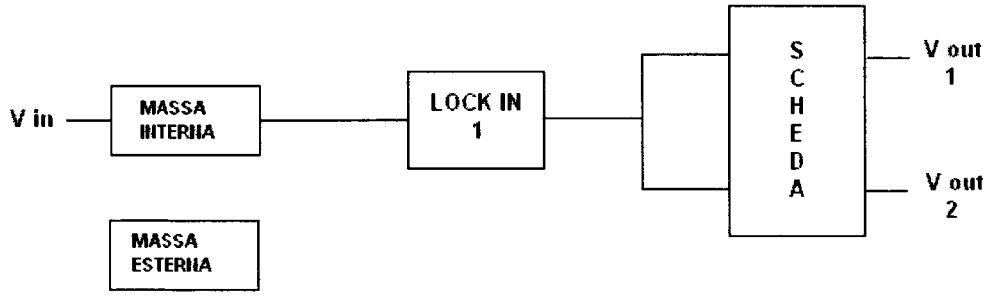

Figure 45 Scheme to measure the common-mode rejection of the acquisition system.

Figure 46 shows the spectral densities of the seismic signal and the rejection obtained at the output of the data acquisition system. After comparing the two spectra, we computed a common-mode rejection factor in the range $3x10^{-4}$ and $3x10^{-5}$ in the frequency range 0.008 Hz and the cut-off frequency of 1 Hz (see Fig. 47).

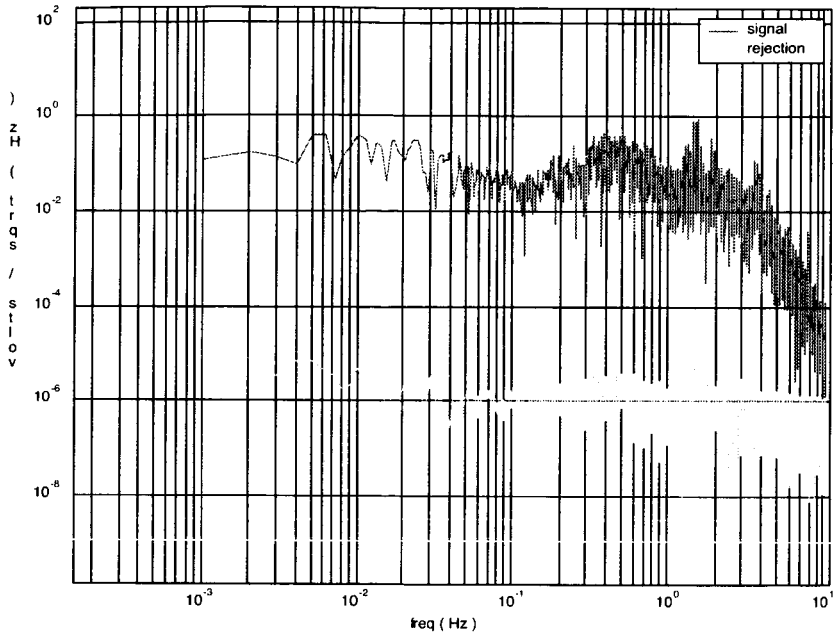

Figure 46 Spectra of seismic noise acquired by one proof mass and the rejection residual from the data acquisition system.

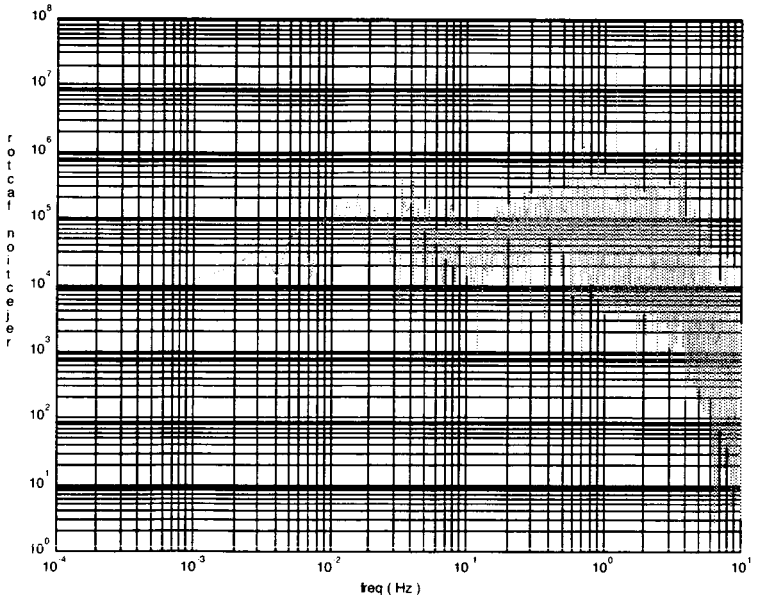

Figure 47 Common-mode rejection factor associated with data acquisition system.

Measurements with two lock-in amplifiers

With this measurement set (GTR54) we aim to evaluate the contribution to the common-mode rejection of the two lock-in amplifiers. The seismic signal measured by the one proof mass has been sent to two lock-in amplifiers and then to the data acquisition system as shown in Fig. 48.

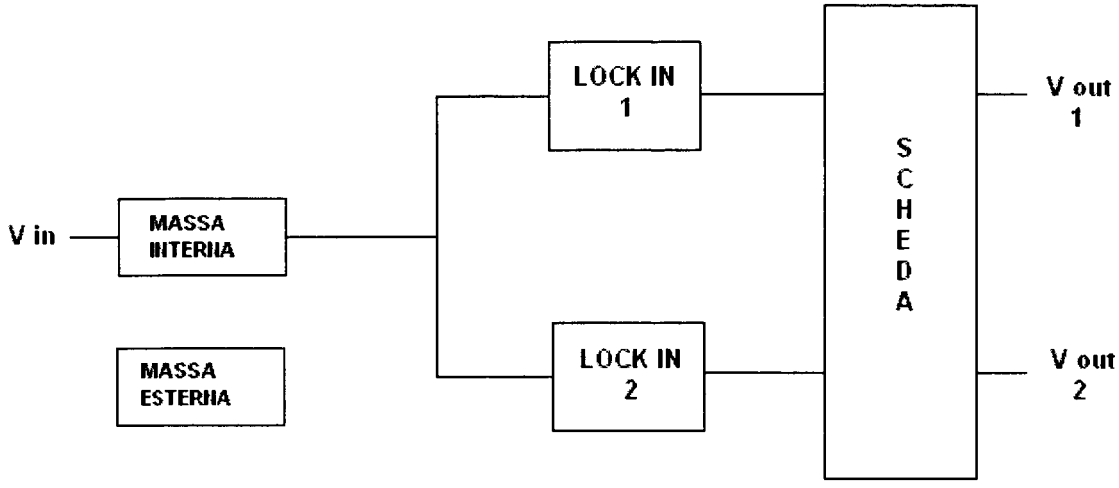

Figure 48 Arrangement to measure the common-mode rejection of the two lock-in amplifiers.

The input (seismic) signal vs. time is shown in Fig. 49. The spectra of the signal and of the rejection obtained at the output of the measurement chain are shown in Fig. 50.

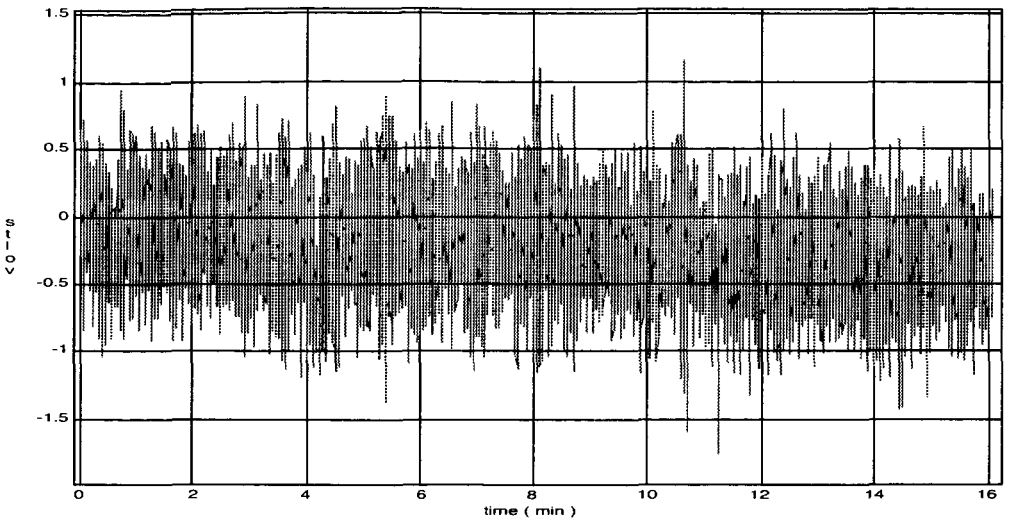

Figure 49 Input signal vs. time.

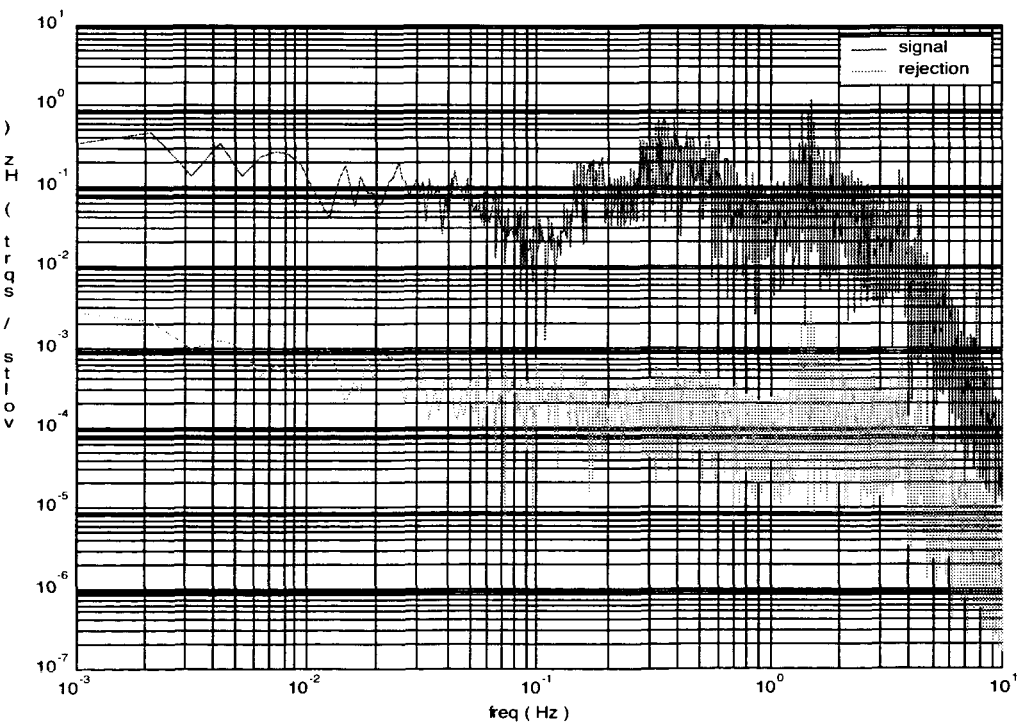

Figure 50 Spectra of input signal and output rejection signal.

After comparing the two spectra we compute a common-mode rejection factor ranging from 100 to 3000 in the frequency band 0.007 Hz and the cut-off frequency of 1 Hz (see Fig. 51).

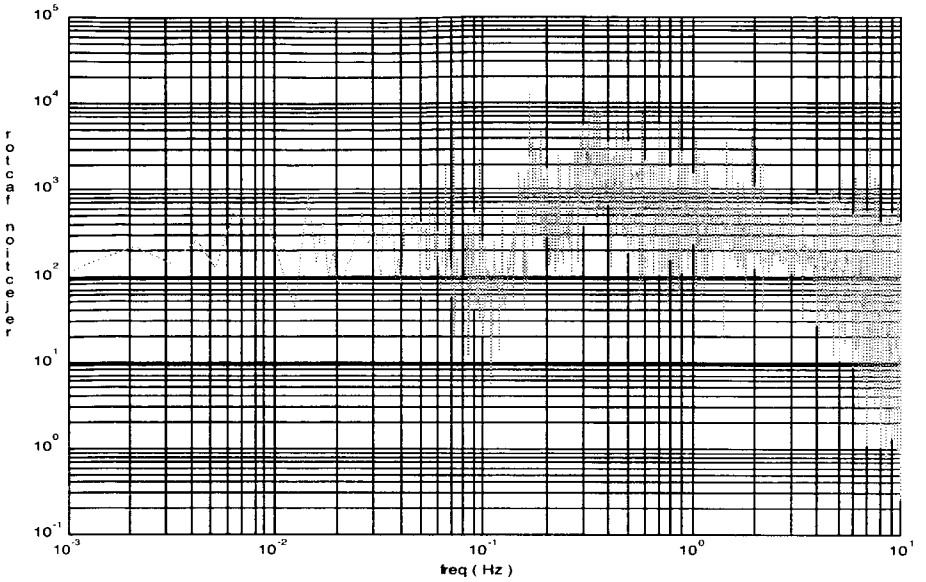

Figure 51 Contribution to common-mode rejection of the two lock-in amplifiers.

Calibration in acceleration units and rejection factor

A new calibration curve, to be associated with this measurement chain, was derived (see Fig. 52) to obtain a calibration factor for the internal proof mass of a 2.149 10^3 Volt/g.

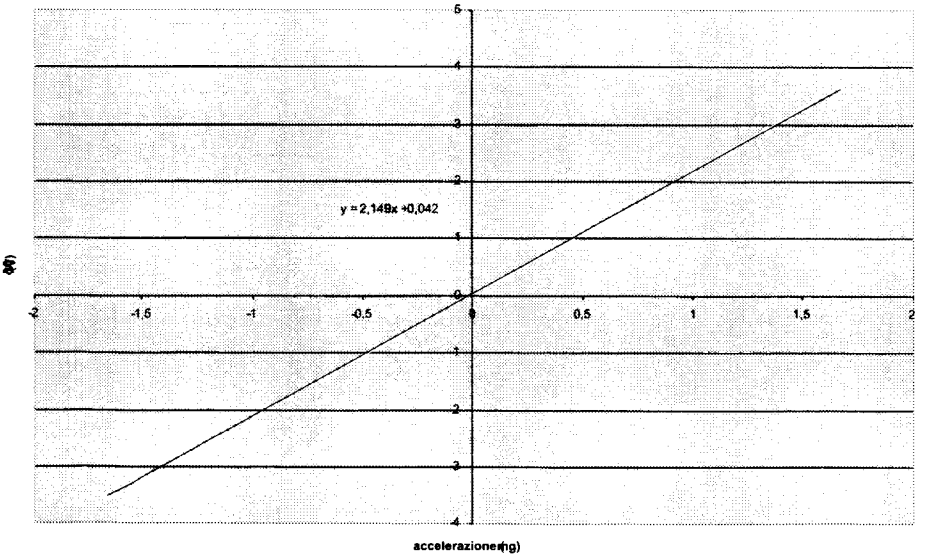

Figure 52 Calibration curve Volts – g for the internal proof mass.

By adopting the calibration factor computed previously, the spectra of the input signal and rejection output can be expressed in terms of acceleration units. The spectra, depicted in Fig. 53, show that the lowest rejection value is 10^{-10} g/sqrt(Hz) for frequencies below the cut-off frequency of 1 Hz. This value must be considered the limiting value for this particular measurement chain.

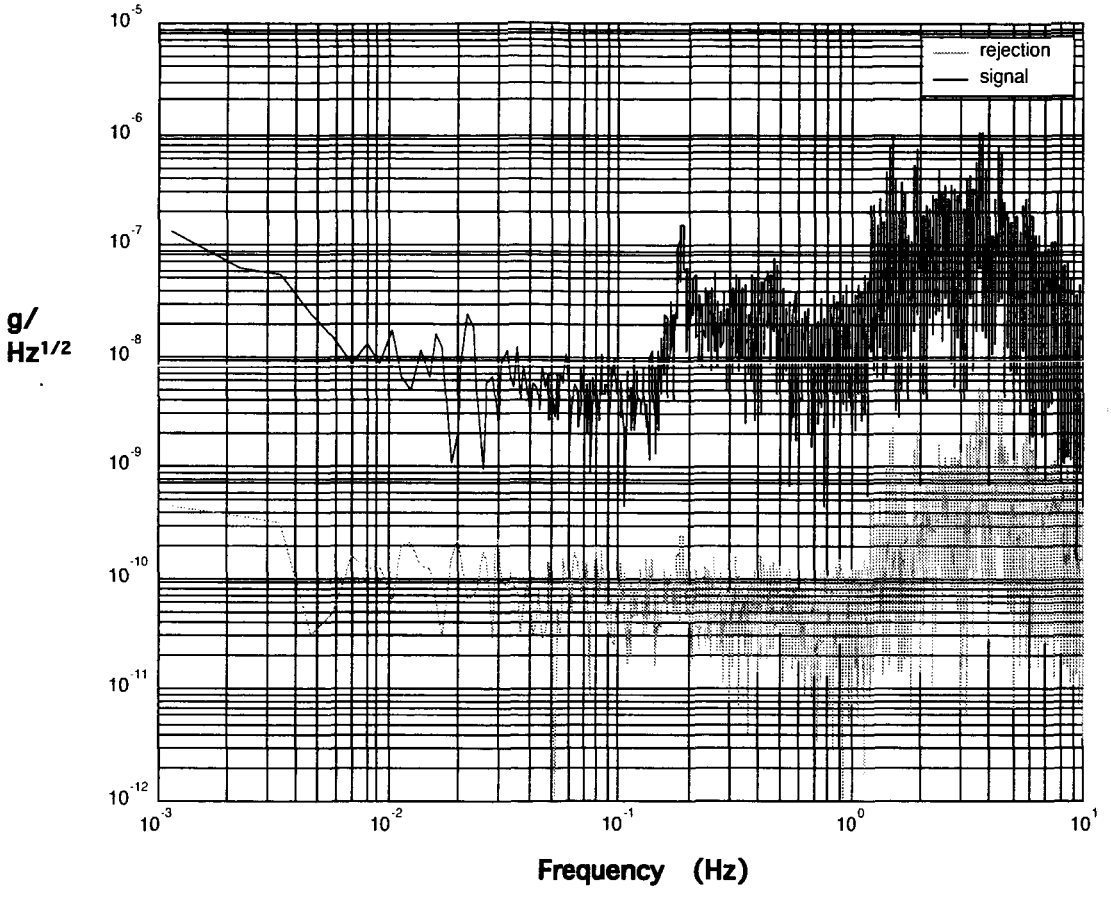

Figure 53 Spectra of input signal and rejection output in terms of acceleration units.

As previously stated, these are preliminary measurements of the common-mode rejection factor in which the limit imposed by the noise of the electronics measurement chain has not yet been approached.

Conclusions

The analysis of the dynamics in free fall of various detector configurations in the presence of release errors and proof masses imperfections has yielded the design of a suitable detector configuration. This configuration provides a very low level of dynamics-related noise at the signal frequency that meets the deired detector's threshold sensitivity goal. The configuration consists of proof masses that have purely rotational degrees of freedom. The internal proof mass is the "EP-violation-sensitive" mass that, thanks to its design made of two halves of different materials, senses an EP violation as a torque about its pivot axis. The second mass, made of one of the materials of the other mass, is the "dynamical-reference" mass. The role of this proof mass is to attenuate (and ideally remove), through output differencing, the dynamics-related noise from the detector's output. In this design, an EP violation will produce a torque that is comparatively strong with respect to gravity gradient torques.

We have demonstrated through extensive simulations that this detector design is capable of detecting a very small differential signal and resolving that signal out of the dynamics-related noise and gravity gradients in the presence of conservative values of the construction imperfections of the proof masses and errors at release. *This conclusion implies that, with this new design, the dynamics-related noise is no longer the limiting factor of the detector's threshold sensitivity. The limiting factor becomes the intrinsic noise of the detector (e.g., the Brownian noise of the proof masses).*

In addition, we have devised a data analysis technique that enables the extraction of a small signal from the colored noise (associated with the detector's dynamics and gravity gradients) and white noise (associated with the detector's intrinsic noise). Moreover, we have estimated the probability of detection of a monochromatic signal of known frequency and phase and the likely error in the amplitude estimate as a function of the signal-to-noise ratio.

Our engineering department has developed a design of the mechanism to spin and release the instrument package inside the cryostat. The mechanism will be capable of operating at cryostatic temperature. The mechanism spins up the detector and then releases it through a two stage process: (1) a very quick short retraction of the two kinematic mounts that support the instrument package; and (2) a relatively fast and longer retraction of the first stage to clear the mechanism out of the instrument package motion.

Our non-US partners have built a second differential detector prototype that incorporates many of the features planned for the flight-experiment detector. They also carried out preliminary laboratory measurements of instrument noise and common-mode rejection factor of the new detector protoype.

Planned Future Work

Tasks to be carried out during the next year research activity are as follows:

Design and construction of an engineering model of the spin and release mechanism for room temperature testing. The engineering model will have all the functionality of the (cryogenic) mechanism for the flight experiments and provisions for unloading the weight of the instrument package so that it can be used for laboratory tests that mimic the zero-g release dynamics.

Compute higher-order gravitational harmonics (coupled to the capsule mass) of the internal proof mass that is made of two halves of different materials, in order to verify that the new design does not violate the noise level requirement of the detector.

Apply the newly-developed noise extraction techniques to data strings obtained from the laboratory noise measurements of the new differential accelerometer prototype. A signal with a signal-to-noise ratio (SNR) comparable to what is expected in the flight tests will be added to the noisy data to test the signal-extraction strategy on experimental data.

Derive a preliminary cost estimate for the design and construction of the balloon-released facility and the recurring operating costs for the experiments.

Provide inputs to our non-US partners for a detailed design of the flight detector based on the results of the detector's dynamics response analysis conducted thus far.

Papers published or submitted during last year grant activity

Ashenberg, J. and E.C. Lorenzini, "Analytical formulation of a complex mutual gravitational field." Classical and Quantum Gravity, Vol. 21, No. 8, 2089-2100, 2004.

Iafolla, V., D.M. Lucchesi, S. Nozzoli, M. Ravenna, F. Santoli, I.I. Shapiro, E.C. Lorenzini, M.L. Cosmo, C. Bombardelli J. Ashenberg, P.N. Cheimets, and S. Glashow, "General Relativity Accuracy Test (GReAT): new configuration for the differential accelerometer." Presented at the COSPAR-2004 Congress, Paris, France, July 2004. Also submitted to Advances in Space Research.

Lorenzini, E.C., I.I. Shapiro, M.L. Cosmo, P.N. Cheimets, C. Bombardelli, V. Iafolla, D.M. Lucchesi, S. Nozzoli, M. Ravenna, F. Santoli, and S. Glashow, "Development of the TEPEE/GReAT experiment to test the Equivalence Principle in Free Fall from a balloon." Proceedings of Testing the equivalence principle in Space and on Ground, Pescara, Italy, 20-23 September 2004.

Iafolla, V., D.M. Lucchesi, S. Nozzoli, M. Ravenna, F. Santoli, I.I. Shapiro, E.C. Lorenzini, M.L. Cosmo, J. Ashenberg, P.N. Cheimets, and S. Glashow, "The Weak Equivalence Principle (WEP) and the General Relativity Accuracy Test (GReAT) with an Einstein Elevator." Proceedings of 16th SIGRAV Conference on General Relativity and Gravitational Physics, Vietri, Italy, 13-16 September 2004.

References

[i] Shapiro, I.I., et al. "Test of the Equivalence Principle in an Einstein Elevator." Smithsonian Astrophysical Observatory, Final Report on NASA Grant NAS8-1780, April 2004.

[ii] Baessler, S., B. Heckel, E. Adelberger, J. Gundlack, U. Schmidt, and E. Swanson, *Phys Rev Lett.,* Vol. 83, 1 Nov. 1999.

[iii] Williams, J.G., X.X. Newhall and J.O. Dickey, Relativity parameters determined from lunar laser ranging, *Phys. Rev. D*, 53, p. 6730, 1996.

[iv] Damour T, F. Piazza, and G. Veneziano, "Runaway dilaton and equivalence Principle violations." Physical Review D, Vol. 66, 081601-1, 2002.

[v] Damour T, F. Piazza, and G. Veneziano, "Violations of the Equivalence principle in a dilaton-runaway scenario." Physical Review Letters Vol. 89, 046007-1, 2002.

[vi] Lorenzini, E.C., I.I. Shapiro, F. Fuligni, V. Iafolla, M.L. Cosmo, M.D. Grossi, P.N. Cheimets and J.B. Zielinski, "Test of the Weak-Equivalence Principle in an Einstein Elevator." Il Nuovo Cimento, Vol. 109B, No. 11, 1994.

[vii] Parzianello, G., E.C. Lorenzini, I.I. Shapiro, M.L. Cosmo, V. Iafolla and S. Nozzoli, "Analysis of Effects of Initial Conditions and Physical Parameters in a Differential Accelerometer Modeled as a Multibody System." Presented at the 54th International Astronautical Federation (IAF) Congress, Oct, 2003, Bremen, Germany.

[viii] Shapiro, I.I., et al. "Test of the Equivalence Principle in an Einstein Elevator." Smithsonian Astrophysical Observatory, Annual Report #1 on NASA Grant NAS3-2881, April 2004.

[ix] Iafolla, V., A. Mandiello and S. Nozzoli, "The High Sensitivity Italian Spring Accelerometer (ISA) for Fundamental Physics in Space" *Advances in Space Research,* Vol. 25, No. 6, 1241-1244, 2000.